

学位論文

**Kuroshio path variations due to
meso-scale eddies and their predictability**

渦活動による黒潮流路変動とその予測可能性

平成16年10月博士(理学)申請

宮澤 泰正

論文内容の要旨

論文題目 Kuroshio path variations due to meso-scale eddies
and their predictability
(渦活動による黒潮流路変動とその予測可能性)

氏名 宮澤泰正

日本南岸を流れる黒潮は、大蛇行流路、非大蛇行接岸流路、非大蛇行離岸流路という3種類の安定した流路をとることが知られている。近年、人工衛星などの観測手段の発達や数値モデリングの進展により中規模渦と黒潮流路変動との関連が示唆されているが、渦解像の海洋大循環モデルを用いて中規模渦と黒潮流路変動の双方が現実的に表現された例は従来無かった。本論文では、高解像度(水平 1/12 度格子)の海洋大循環モデルを人工衛星観測等から得られた現実的な外力で駆動することにより、中規模渦活動と黒潮流路変動との相互作用をモデル内で表現できることを示した。さらに、開発した海洋大循環モデルにデータ同化とアンサンブル予測手法を適用し、1999年に生じた現実の黒潮流路変動の予測可能性について中規模渦との相互作用の観点から明らかにした。

最初に、1992年から1998年までの外力を用いて海洋大循環シミュレーションを行った。7年間の平均的な黒潮流路は非大蛇行接岸流路であったが、非大蛇行離岸流路への遷移も見られた。非大蛇行離岸流路は黒潮と高気圧性渦との相互作用によって生じることがわかった。さらに、一時大蛇行に似た流路も生じた。大蛇行的な流路は高気圧性の黒潮再循環が著しく強化された後に生じた。黒潮の再循環は、上流域から高気圧性渦が連続的に再循環域に進入し合体することによって強化される。これらの高気圧性渦がルソン島の北東海域から黒潮によって移流される過程で上流域の黒潮流量が経年的に増加する。一方、黒潮続流域域から伝播する低気圧性渦は黒潮の蛇行と合体し切離することによって蛇行の振幅を弱めその消滅に寄与することもわかった。

以上の結果は、日本南岸の黒潮流路変動が亜熱帯循環系における中規模渦活動と密接に

関係していることを示唆している。特に、中規模渦活動を媒介として黒潮再循環が強化されたときに大蛇行的な流路が発生したことは興味深く、黒潮大蛇行発生の予測可能性を考える上で重要な示唆を与える。ただし、シミュレーションで表現された大蛇行的な流路は持続時間が1年に満たず不安定であり厳密な意味で大蛇行流路であるとは言えず、大蛇行流路が安定して持続する状態の再現には至らなかった。

流路の変動には中規模渦と黒潮の非線形な相互作用が大きく影響するので、現実の流路変動を正確に予測するためにはデータ同化により正確に初期状態を推定しその後の時間発展を予測することが必要になる。そこで、同じ海洋大循環モデルを用い現実の黒潮蛇行の予測可能性について調べるために、データ同化手法を適用し予測実験を行った。海面高度データを40日間モデルに同化することによって1999年の9月7日の初期値を作成しハインドキャスト実験を行った結果、1999年11月に生じた黒潮蛇行を再現することができた。この黒潮蛇行は、九州南東沖にあった高気圧性渦と黒潮の相互作用によって生じたものであり最初の大循環シミュレーションで表現された流路変動の過程とよく似ている。モデルは初期化以後80日間有意な予測をしていることがわかった。さらに、ブリーディング法によって10個の摂動を作成し9月7日の初期値にそれぞれ付加してアンサンブル予測実験を行った。アンサンブルメンバーの予測結果は、予測開始50日以降大蛇行型と非大蛇行型に分岐した。アンサンブル予測実験の結果は、1999年の黒潮が大蛇行及び非大蛇行流路の多重平衡状態にあったことを示唆している。

予測結果における大蛇行と非大蛇行の分岐の原因を調べたところ、初期状態における高気圧性渦の強度が分岐に大きく影響することがわかった。初期状態に強い高気圧性渦があった場合には、蛇行の成長に伴い下層と上層の流れが強く励起された状態が生ずる。この現象は大循環シミュレーションにおける蛇行の増幅の過程でみられたものと同様なものである。高気圧性渦の力学は前線地衡流レジームに従い、その振る舞いの時間スケールは下層の流れによって決められる。推定される時間スケールは、黒潮による直接の移流の時間スケール(10日程度)よりは長く予測結果の分岐が生ずる時間スケールである50-80日とほぼ一致した。このことは、蛇行の予測可能性を決める時間スケールが渦そのものの挙動に影響されていることを示唆している。

本研究は、日本南岸の黒潮流路変動のモデリングとオペレーショナルな予測に必要な以下の条件を示唆する。すなわち、北太平洋の亜熱帯循環全体をモデリングすること、黒潮・黒潮続流域及び亜熱帯前線海域を1/10度以下の水平高解像度で表現すること、海底地形を適切に取り扱い少なくとも20層以上の鉛直格子により成層を正確に表現すること、衛星海上風などの現実的な外力を用いること、正確な予測のために多種類のデータを同化することにより適切な初期値を与えることである。

Abstract

This thesis investigates the Kuroshio path variation south of Japan from the viewpoint of eddy-Kuroshio interactions. A basin-scale eddy-resolving ocean general circulation model is a primary tool for this study. In addition, predictability of the Kuroshio path variation is investigated by conducting an ensemble forecast experiment of the real event.

A high-resolution ocean general circulation model is developed to simulate connections between the Kuroshio path variations and meso-scale eddy activities as realistically as possible. The mean climatology of the modeled Kuroshio takes a nearshore non-large-meander path. It is found that the model is capable of simulating two types of non-large-meander state, and the large-meander like path. The offshore non-large-meander is generated through interaction between the Kuroshio and an anticyclonic eddy. The large-meander like path occurs just after significant intensification of the anticyclonic Kuroshio recirculation; successive intrusion of anticyclonic eddies from the upstream region is responsible for this process. Those anticyclonic eddies are advected by the Kuroshio from the region northeast of the Luzon Island and increase the upstream Kuroshio volume transport on an interannual time scale. The cyclonic eddies propagating from the Kuroshio Extension region, on the other hand, weaken the Kuroshio meander after the merger. The Kuroshio path variations south of Japan thus seem be closely related to eddy activities in the subtropical gyre system. The present model simulates the eddy-Kuroshio interaction in a more realistic way than previous studies. However, its ability to reproduce the large-meander state needs improvement because the duration is too short compared to observations.

By using the developed ocean general circulation model, an ensemble forecast experiment is conducted to understand predictability of the Kuroshio meandering. The application of the ensemble forecast to the problem addressed seems to be the first comprehensive attempt in the community of physical oceanography. By assimilating sea

surface height anomaly into the model in the preceding 40 days period, the observed Kuroshio meandering manifested south of Japan in November 1999 was successfully predicted two months before the event. The predicted states realized as the ensemble members are classified into two categories: large and non-large-meander. It is found that the intensity of an anticyclonic eddy in the initial state seems to play a key role in selecting one of the two states.

This study provides a basis for operational forecasting of the Kuroshio path south of Japan. Suggested necessary conditions are: 1) modeling of the whole subtropical gyre system over the North Pacific, 2) horizontal high-resolution smaller than 1/10 degree, covering both the Kuroshio-Kuroshio Extension and subtropical front regions, 3) careful treatment of bottom topography and representation of stratification by well-designed vertical grid with more than 20 levels, 4) use of realistic forcing, for example, satellite scatterometer wind, and 5) proper initialization by assimilation using multi satellite data.

Contents

General Introduction	1
Part I Roles of meso-scale eddies in the Kuroshio paths	5
1.1 Introduction	6
1.2 Numerical model	8
1.3 The model results	11
1.3.1 Mean state of the Kuroshio	11
1.3.2 Variability of the surface geostrophic current	12
1.3.3 Meso-scale eddy activity south of Japan	13
1.3.4 Path variations of the Kuroshio	14
1.4 Roles of meso-scale eddies on the Kuroshio path variations	15
1.4.1 Offshore non-large-meander	15
1.4.2 Large-meander like path	16
1.4.3 Energetics of the meander growth	18
1.4.4 Variation of the Kuroshio recirculation	21
1.5 Summary	24
Appendix.1: Linear stability analysis	27
Tables	30
Figures	33
Part II Ensemble forecast of the Kuroshio meandering	59
2.1 Introduction	60
2.2 Hindcast of the Kuroshio meandering in 1999	63
2.2.1 Ocean model	63
2.2.2 Hindcast of the Kuroshio meandering in 1999	64
2.3 Ensemble forecasts	67

2.4	Predictability of the Kuroshio meandering	71
2.5	Summary	74
	Appendix.2: Weight of correction for the analysis equation	76
	Figures	78
	General conclusion	89
	Acknowledgements	95
	References	96

General Introduction

The Kuroshio, one of the most energetic western boundary current, has been extensively studied from data analysis, theoretical, and modeling standpoints. It is quite unique among various western boundary currents that the Kuroshio has three typical paths along the southern coast of Japan. These are the large-meander path, the nearshore non-large-meander path, and the offshore non-large-meander path according to the definition given by Kawabe (1985). The large-meander and non-large-meander paths persist from a few years to a decade, suggesting a link with basin-wide climate variations. Large volume transport of the Kuroshio in the East China Sea is related to the Kuroshio large-meander occurring with a bi-decadal time scale (Kawabe 1995), which is basically determined by the Sverdrup transport variation in the subtropical North Pacific (Qiu and Miao 2000). During the large-meander dominant period from 1975 to 1991, peaks of the Kuroshio volume transport closely connected with ENSO seem to correspond to the large-meander events with several-year interval (Kawabe, 2001).

Recent studies suggest that the transition between the nearshore and the offshore non-large-meander paths during the last decade is influenced by meso-scale eddy activity (Ebuchi and Hanawa 2000, 2003; Mitsudera et al. 2001). Several numerical experiments have been performed recently to examine how an anticyclonic eddy introduced artificially in ocean models triggers the path transition from the nearshore to the offshore non-large-meander path (Mitsudera et al. 2001) or to the large-meander path (Endoh and Hibiya 2001; Akitomo and Kurogi 2001).

Many theoretical works have addressed mechanisms of the Kuroshio large-meander since the pioneering work of Robinson and Taft (1972). Using an eddy-permitting, two-layer primitive equation model of the North Pacific, Qiu and Miao (2000) have recently suggested that the accumulation of low potential vorticity water in the Kuroshio recirculation region influences the Kuroshio path variation. They renewed interest in possible connections of the Kuroshio large-meander to the whole subtropical gyre system

including the low-latitudes as well as the recirculation region, rather than considering the meander simply as a local nonlinear phenomenon (see also Saiki 1982; Yamagata et al. 1985; Yamagata and Umatani 1987). Hurlburt et al. (1996) , using an eddy-resolving, six-layer primitive equation model, also showed that the basin-wide structure of stratification and the basin-wide increasing/decreasing trend of the wind stress change the frequency of the large-meander path through baroclinic instability west of the Izu-Ogasawara Ridge. However, the explicit roles of the meso-scale eddies south of Japan have not been clarified so far in a basin-scale ocean general circulation model (OGCM).

To investigate the Kuroshio path variations resulting from basin-scale eddy-Kuroshio interactions, we have developed a basin-wide eddy-resolving OGCM. Since the first baroclinic Rossby radius south of Japan is about 40km (Emery et al. 1984), a numerical model needs to have a grid size less than 10km to resolve meso-scale eddies. Also, we prefer a basin-scale model to simulate a whole gyre system. To meet these conflicting requirements, we adopted a one-way nesting method (Guo et al. 2003).

Even with a $1/18^\circ$ resolution model, Guo et al. failed to reproduce the realistic Kuroshio path variation. During 7 years simulation from 1991 to 1998, their model showed only the nearshore non-large-meander path, while the real Kuroshio showed frequent path transitions between the nearshore and offshore paths (Guo et al. 2003). Their model area (24° - 44° N, 118° - 150° E) did not completely include two regions with meso-scale eddy activity: the Kuroshio Extension and the subtropical front. To overcome the above problem, we included the two eddy-active regions in the high-resolution ($1/12^\circ$) model. As a result, we succeeded to simulate the Kuroshio path variations due to eddy-Kuroshio interactions in the basin-scale OGCM. The model simulation with wind and heat forcing from 1992-1998 reproduces the offshore non-large-meander path, the nearshore non-large-meander path and the large-meander like path. In Part I based on Miyazawa et al. (2004), we describe details of the Kuroshio path variation in view of the interaction with

meso-scale eddies. Although duration of the simulated large-meander like path is shorter than is observed, analyzing how the large amplitude of the meander appears may be useful for study of the Kuroshio path variations. From analysis of the model simulation, we suggest a scenario for the formation of the Kuroshio large-meander.

Our OGCM simulation suggests that the Kuroshio path variation is strongly affected by internal dynamics, which largely depends on initial state. Therefore, short-term forecast of the real path variation may be feasible by proper initialization of the model state. In Part II based on Miyazawa et al. (2005b), we conduct hindcast experiments of the path transition from the nearshore to offshore non-large-meander in 1999 to investigate the predictability of the real Kuroshio meandering from the viewpoint of the eddy-Kuroshio interactions. Data assimilation of the TOPEX/POSEIDON satellite altimetry allows us to realistically initialize the OGCM. In order to systematically evaluate the impact of difference of initial states, moreover, we perform ensemble forecasts experiment. In particular, we focus on relations between intensity of the initial trigger eddy and resulting meander amplitude of the ensemble forecasts. The application of the ensemble forecast technique to the Kuroshio meandering problem seems to be the first comprehensive attempt in the community of physical oceanography.

This study provides a basis for operational forecasting of the Kuroshio path south of Japan. Both the OGCM and data assimilation method developed in the study were used as prototype components of an operational nowcast/forecast system of the Japan Coastal Ocean (Miyazawa and Yamagata 2003; Miyazawa et al. 2005a). Products of more advanced nowcast/forecast system will contribute to understanding of the ever-mysterious Kuroshio path variation.

Part I

Roles of meso-scale eddies in the Kuroshio paths

1.1 Introduction

The Kuroshio is one of the most energetic western boundary currents associated with high meso-scale eddy activity. It is quite unique among various western boundary currents that the Kuroshio has three typical paths along the southern coast of Japan. As shown in Fig.1.1, these are the large-meander path, the nearshore non-large-meander path, and the offshore non-large-meander path according to the definition given by Kawabe (1985). The large-meander and non-large-meander paths persist from a few years to a decade, suggesting a link with basin-wide climate variations. The large-meander path has not been observed during the last decade. However, the transition between the nearshore non-large-meander path and the offshore non-large-meander path has been frequently observed; the primary period of the path transition is 1.6-1.8 years (Kawabe 1987).

Recent studies suggest that the transition between the nearshore and the offshore non-large-meander paths during the last decade is influenced by meso-scale eddy activity (Ebuchi and Hanawa 2000, 2003; Mitsudera et al. 2001). Analyzing satellite altimetry data, Ebuchi and Hanawa (2003) suggested that anticyclonic/cyclonic eddies trigger the offshore non-large-meander observed from 1993 to 1999. Several numerical experiments have been performed recently to examine how an anticyclonic eddy introduced artificially in ocean models triggers the transition from the nearshore to the offshore non-large-meander path (Mitsudera et al. 2001) or to the large-meander path (Endoh and Hibiya 2001; Akitomo and Kurogi 2001). However, the inflow/outflow models (Mitsudera et al. 2001; Endoh and Hibiya 2001) or non-eddy-resolving models (e.g., Akitomo and Kurogi 2001) cannot capture the meso-scale eddy activity linked to basin-scale processes.

Recent observational studies suggest that two kinds of meso-scale eddy activity exist in this region. The first is westward propagating eddies with a spatial scale of 500km and a time scale less than 3 months, probably originating in the Kuroshio Extension and entering the Kuroshio recirculation region at 30°N (Ebuchi and Hanawa 2000). The second is

meso-scale eddies located farther to the south near 23° N. After being captured by the offshore current of the Kuroshio south of Okinawa (the Ryukyu Current), they are advected by the Kuroshio itself to the Shikoku Basin, where they eventually merge with the eddies propagating from the Kuroshio Extension region (Ichikawa 2001).

Many theoretical works have addressed mechanisms of the Kuroshio large-meander since the pioneering work of Robinson and Taft (1972) (see references of Qiu and Miao 2000). Using an eddy-permitting, two-layer primitive equation model of the North Pacific, Qiu and Miao (2000) have recently suggested that the accumulation of low potential vorticity water in the Kuroshio recirculation region influences the Kuroshio path variation. They renewed interest in possible connections of the Kuroshio large-meander to the whole subtropical gyre system including the low-latitudes as well as the recirculation region, rather than considering the meander simply as a local nonlinear phenomenon (see also Saiki 1982; Yamagata et al. 1985; Yamagata and Umatani 1987). Hurlburt et al. (1996), using an eddy-resolving, six-layer primitive equation model, also showed that the basin-wide structure of stratification and the basin-wide increasing/decreasing trend of the wind stress change the frequency of the large-meander path through baroclinic instability west of the Izu-Ogasawara Ridge. However, the explicit roles of the meso-scale eddies south of Japan have not been clarified so far using a basin-scale ocean general circulation model (OGCM).

The purpose of this part is to investigate possible connections between the Kuroshio path variations and meso-scale eddy activity using an eddy-resolving OGCM. The horizontal grid spacing of the model is $1/12^{\circ}$ in both zonal and meridional directions, which corresponds to about 9km in the Kuroshio region. This grid spacing is much smaller than the first baroclinic Rossby radius in the Northwest Pacific (see Emery et al. 1984). The present model with wind and heat forcing from 1992-1998 reproduces the offshore non-large-meander path, the nearshore non-large-meander path and the large-meander like

path.

This part is organized as follows. In Section 1.2, the model configuration is described. In Section 1.3, the mean state and variability of the model are discussed. Then sea level variations are discussed in connection with the Kuroshio path variation. The model skill for representing meso-scale eddy activities is also argued. In Section 1.4, we describe details of the Kuroshio path variation in view of the interaction with meso-scale eddies. We also examine effects of the meso-scale eddy activity on the intensity of the Kuroshio. Section 1.5 is devoted to summary and discussion.

1.2 Numerical model

The present model is based on one of the world community models, Princeton Ocean Model (POM) (Mellor 1996). The POM is a three-dimensional primitive equation ocean model including thermodynamics. The vertical coordinate of POM is represented by a bottom-following (sigma coordinate) system. The horizontal grids are defined on spherical coordinates. The vertical viscosity and diffusivity are calculated using the level 2.5 turbulent closure scheme of Mellor and Yamada (1982). The horizontal viscosity is calculated by the Smagorinsky-type formulation (Smagorinsky et al., 1965), which is proportional to the square of grid size and horizontal velocity shear with a coefficient of 0.05. The horizontal diffusivity coefficient is assumed to be one half of the viscosity coefficient. The bottom stress is calculated by the quadratic formula with an empirical drag coefficient, the minimum value of which is 2.5×10^{-3} . Coastal boundary conditions are no slip as well as no mass flux.

The model for the North Pacific (Fig.1.2) is run in both low-resolution ($1/4^\circ$ to 1°) and high-resolution ($1/12^\circ$) configurations. The bottom topography of the low-resolution model is created from the $1/12^\circ$ global height data, GETECH DTM5. This low-resolution basin-wide model ranges from 30°S to 62°N and 100°E to 70°W and has 21 sigma levels

in the vertical as in the previous study (Guo et al. 2001). The horizontal resolution varies from $1/4^\circ$ in the region corresponding to the high-resolution model to 1° near the boundary. The high-resolution regional model, with uniform horizontal resolution of $1/12^\circ$, extends from 10° to 50°N , 117°E to 180° (Fig.1.2). This high-resolution model has 45 sigma levels (Table 1.1). The distribution of vertical levels is introduced to resolve the bottom and surface boundary layers. The bottom topography of the high-resolution model is also created from the $1/12^\circ$ data, DTM5. In addition, the 500m-mesh bottom topography provided by Hydrographic Department of Japan is embedded in the coastal sea around Japan.

The bottom topography in both models has been smoothed to reduce the pressure gradient error (Mellor et al. 1994). The maximum bottom slope between two adjacent grid

points is constrained by the inequality, $\frac{|H_1 - H_2|}{|H_1 + H_2|} \leq 0.2$. To reduce the pressure gradient

error, we have adopted a Gaussian smoother with $1/2^\circ$ scale for the low-resolution grid and with $1/12^\circ$ scale for the high-resolution grid. A ‘zero forcing run’ with a horizontally uniform, stable stratification allows us to estimate the current induced by the pressure gradient error. The magnitude of the erroneous velocity due to the pressure gradient error is less than a few cm/s for both of the models. We note here that local topography such as the Koshu Seamount, which may influence the Kuroshio path dynamics south of Japan (Hurlburt et al., 1996; Endoh and Hibiya, 2001), is well resolved in the high-resolution model even after the smoothing.

Northern and southern boundaries of the low-resolution model are treated as open boundaries, along which a radiation condition is adopted on external mode velocities, together with a one-sided advection scheme for temperature and salinity. Both temperature and salinity fields are specified on open boundaries using monthly climatology data (Levitus and Boyer 1994; Levitus et al., 1994). The internal mode velocities on open

boundaries are assumed to vanish.

Variables on all lateral boundaries of the high-resolution regional model are determined by values interpolated bilinearly from the low-resolution basin model (Guo et al. 2003). Vertical boundary variables for the high-resolution model with 45 sigma levels are created from the low-resolution model with 21 sigma levels by linear interpolation. The radiation condition considering the sea surface height of the lower-resolution model is adopted on external mode velocities to avoid reflection of gravity waves from the open boundary. Daily mean variables of the low-resolution model are stored on a disk for the purpose of one-way nesting. The bottom topography near the boundary of the high-resolution model is the same as that of the low-resolution model to allow smooth connection of both models by linear interpolation of sigma coordinate variables.

Sea ice formation and river runoff are not included in these simulations. Since nudging to the monthly climatology of temperature and salinity in the Okhotsk Sea improves water mass properties in the mixed water region north of the Kuroshio Extension (H. Mitsudera 2000, personal communication), we followed their recipe in both the Okhotsk Sea and the Bering Sea. This procedure may be regarded as a kind of parameterization for sea ice and lateral freshwater effects. The sea surface temperature is nudged to the observed temperature with a restoring time scale of 7 days in both regions.

The model is driven by wind stresses, and heat and salt fluxes. The wind stress field is calculated on a weekly basis from ERS-1 and -2 satellite scatterometer data with a $1^\circ \times 1^\circ$ resolution. The Reynolds and Smith (1994)'s sea surface temperature field used in the simulation is blended from ship, buoy and bias-corrected satellite data with a $1^\circ \times 1^\circ$ resolution also on a weekly basis. The surface heat flux is applied using the Haney type formula (Haney 1971); the coefficient used in the retroaction term is $35 \text{Wm}^{-2} \text{K}^{-1}$. Salinity at the surface is restored to the monthly mean climatology (Levitus et al. 1994) with a time scale of 30 days.

The present simulation is conducted with two steps: an initial spin-up experiment and an experiment with forcing from 1992-1998. In the spin-up experiment, the two models are started from a state of rest with annual-mean temperature and salinity derived from the $1/4^\circ \times 1/4^\circ$ climatology data (Boyer and Levitus 1997). The spin-up period is 20 years for the coarse-resolution model and 12 years for the fine-resolution model. They are forced by monthly mean climatological wind stresses derived from ERS-1 and -2 wind data and monthly mean climatological heat flux (Da Silva et al. 1994) modified with the monthly mean SST data. The simulation used for the present analysis is started from the final year of the spin-up experiment using the weekly mean wind stress and the monthly mean climatological heat flux modified with the weekly mean SST data from 1 January 1992 to 31 December 1998.

1.3 The model results

1.3.1 Mean state of the Kuroshio

Figure 1.3 shows the mean sea surface height field from the high-resolution model during the simulation period from 1992 to 1998. The model reproduces the Kuroshio-Kuroshio Extension system well with reasonable separation latitude at around 35°N . In addition, the anticyclonic recirculation gyre is resolved on the southern side of the Kuroshio, which is comparable to the observed recirculation (e.g., Hasunuma and Yoshida 1978). We also note that the model climatology of the Kuroshio path south of Japan is the nearshore non-large-meander path.

The streamfunction averaged for the period from 1992 through 1998 is shown in Fig.1.4. The volume transport of the Kuroshio across the PN line in the East China Sea (see Fig.1.1) and that for the Ryukyu Current east of the Nansei Islands are about 25 Sv and 15 Sv, respectively, which are comparable to observations (Kawabe. 1995; Zhu et al. 2003).

Therefore, the present model resolves successfully the two upstream branches of the Kuroshio. However, the eastward volume transport across the ASUKA line south of Japan (Fig.1.1) reaches 79 Sv, which is much larger than the mean value of 57 Sv observed from 1992 to 1997 by Imawaki et al. (2001). The volume transport associated with the Kuroshio Countercurrent is about 39 Sv in the model while the corresponding volume transport south of Shikoku is only 15 Sv in the observation.

1.3.2 Variability of the surface geostrophic current

In order to examine ocean variability near the surface, the eddy kinetic energy (EKE) field derived from satellite altimetry data such as TOPEX/POSEIDON (T/P) is quite useful. Because of their global coverage, satellite data effectively capture the spatial pattern of eddy activity (Stammer 1997). In the present study, we use the NASA/GSFC Ocean Pathfinder collinear data set for the T/P altimeter mission over the period between September 1992 and December 1998.

The EKE is calculated from the along-track gradient in the sea surface height anomaly assuming the geostrophic approximation. Before this calculation, the model sea surface height anomaly is interpolated on the satellite track. Then the EKE along the satellite track is interpolated to half-degree-regular-grids using an optimal interpolation method.

Figure 1.5a shows that the satellite-derived EKE is higher than $0.03 \text{ m}^2 \text{ s}^{-2}$ in the western subtropical region between 15°N and 40°N . In particular, the North Equatorial Current and the Kuroshio-Kuroshio Extension show values higher than $0.08 \text{ m}^2 \text{ s}^{-2}$. The flow field south of Japan also shows high EKE, which reflects the path variation of the Kuroshio. As shown in Fig.1.5b, the present high-resolution model successfully reproduces those satellite-derived features. The maximum EKE in the Kuroshio-Kuroshio Extension region is larger than $0.3 \text{ m}^2 \text{ s}^{-2}$ in the model, which is comparable to the observation. The high EKE in the Kuroshio region is attributed not only to meso-scale eddy activity but also

to the path migration of the Kuroshio (Mizuno and White 1983). The realistic EKE distribution in the model mainly results from the high horizontal resolution (Guo et al. 2003). However, the model does not reproduce well the observed EKE in the central part of the subtropical gyre. This may reflect the deficiency of resolving mid-ocean eddies in the low-resolution model.

1.3.3 Meso-scale eddy activity south of Japan

Using the T/P data, Ebuchi and Hanawa (2000) have reported that significant meso-scale eddy activity with time scale of 40-200 days is seen to the south of Japan (27° - 30° N, 135° - 155° E). In a subsequent paper, they have suggested that coalescence of the meso-scale eddy with the main stream may trigger the path variation of the Kuroshio (Ebuchi and Hanawa, 2003).

In order to compare statistical properties of the eddy activity with observations, we plot power spectra of sea surface height anomaly calculated using the T/P data and the model output (Fig.1.6). Before this calculation, the model sea surface height anomaly is interpolated on the satellite track. Although the model fails to simulate the eddy activity with time scales of 40–200 days south of Japan (27° - 30° N, 135° - 155° E), it successfully simulates the eddy activity in a slightly more northern region (29° - 32° N 135° - 155° E). The horizontal scale evaluated from the filtered sea surface height anomaly in the latter region is 500 km (Fig.1.7), which is comparable with the observation. The westward phase speed is estimated using the linear least squares fitting for maximum correlation in space-time lag correlation maps (Fig.1.8). Modeled westward phase speed is 5.5 cm s^{-1} , which is almost the same as the observed value of 5.4 cm s^{-1} . The vertical sections for simulated eddies over the Izu-Ogasawara Ridge are shown in Fig.1.9. The eddy has a diameter of about 400 km and a maximum swirling speed of about 60 cm s^{-1} and extends to a depth of 1000 m. Displacement of the 15°C isotherm reaches about 200 m at the

center. All these properties correspond well to observations (Ebuchi and Hanawa 2000; Mitsudera et al. 2001).

1.3.4 Path variations of the Kuroshio

Three different types of the Kuroshio path south of Japan are simulated in the present model which uses atmospheric forcing from January 1992 to December 1998. Two correspond to the nearshore non-large-meander and the offshore non-large-meander, following the definition of Kawabe (1985). The other path is similar to the large-meander. The mean path during the simulation period corresponds to the nearshore non-large-meander path (Fig.1.3). The real Kuroshio shows only transitions between the offshore and nearshore non-large-meander paths during the simulation period (Ebuchi and Hanawa 2003).

It is well known that the change of the Kuroshio path is associated with sea level changes along the southern coast of Japan. According to tide gauge data, the sea level difference between Kushimoto and Uragami (see Fig.1.1 for locations) during the large-meander state is negative (about -100mm) and less variable than during the non-large-meander state (Kawabe 1995). During the period from 1992 to 1998, the large-meander has not occurred (Fig.1.10a). In the present model, this feature is reproduced well as shown in Fig.1.11a. The modeled Kuroshio path from November 1993 to July 1994 and from January 1998 to May 1998 is similar to the large-meander path. The sea level difference between Kushimoto and Uragami is negative and less variable during these periods as in the observations of the large-meander, even though the duration is much shorter than is observed. The actual large-meander path persists for a period from a few years to a decade.

Kawabe (1985) showed that the sea level at Hachijojima (see Fig.1.1 for location) is useful for distinguishing the offshore non-large-meander from the nearshore

non-large-meander. When the sea level at Hachijojima is high, the main axis of the Kuroshio is close to the Japan coast. On the other hand, the sea level at Hachijojima is low, when the Kuroshio is away from the coast of Honshu. During the period from 1992 to 1998, the real Kuroshio shows path transitions between the nearshore and offshore paths (Fig.1.10b). The time series of the model sea level at Hachijojima indicates the existence of two basic states. The nearshore non-large-meander is characterized by sea level ranging between 0 to 400mm and the offshore non-large-meander is for the range between -700 to -300 mm (see arrows in Fig.1.11b). Thus the model appears to reproduce both non-large-meander paths during the simulation period. We note that a low sea-level state at Hachijojima in the model appears to correspond to the state of negative sea-level difference between Kushimoto and Urugami. This feature is inconsistent with observation; the typical large-meander shows high sea level state at Hachijojima (Kawabe 1985).

In summary, the model reproduces both of two non-large-meander states, but its ability to reproduce the large-meander state needs improvement because the duration is too short compared to observations. Thus we must distinguish the simulated large meander like path from the real large-meander. The low sea level state at Hachijojima, which has been frequently observed in the decay phase of the large-meander (Kawabe 1995), may be associated with the short duration of the large-meander like path in the present model. Nevertheless, the existence of the brief large-meander like path states in the model is worthy of further investigation; the present model appears to capture almost all key elements in the Kuroshio large-meander formation.

1.4 Roles of meso-scale eddies on the Kuroshio path variations

1.4.1 Offshore non-large-meander

The sea level at Hachijojima exhibits a low state for a short period of about one month

three times from February 1993 to August 1993 (see arrows in Fig.1.11b). These short-term variations correspond to the offshore non-large-meander as mentioned in the previous section. We analyze the formation of the offshore non-large-meander here in detail.

As shown in Fig.1.12, small anticyclonic eddies are found along the offshore side of the Kuroshio from the Luzon Island to the Kuroshio recirculation region in the summer of 1992. Anticyclonic eddies passing through the Tokara Strait influence the Kuroshio path there and induce subsequent small meanders further downstream, southeast of Kyushu (Fig.1.12b). Ichikawa (2001) has discussed the downstream propagation of the anticyclonic/cyclonic eddies along the Kuroshio in Nansei Island using the T/P, ERS-1 and ERS-2 altimetry data. The small anticyclonic eddies propagating downstream are absorbed by a large anticyclonic eddy located near the Izu-Ogasawara Ridge as shown in Fig.1.12d, 1.13a. The large eddy then propagates westward and collides with the Kuroshio east of Kyushu about three months after the eddy formation (Fig.1.13b). The Kuroshio to the east of the Kyushu is intensified and then meanders east of the Kii Peninsula in February of 1993 (Fig.1.13c). This eddy-Kuroshio interaction process is similar to a real event observed in 1998 (Mitsudera et al. 2001; Ebuchi and Hanawa 2003). The anticyclonic eddy associated with this offshore non-large-meander evolves by absorbing small eddies near the Izu-Ogasawara Ridge and finally separates from the Kuroshio. Then the whole process is repeated two more times (e.g., Fig.1.13d).

1.4.2 Large-meander like path

The Kuroshio took the large-meander like path after three episodes of interaction with an anticyclonic eddy during the state of the offshore non-large-meander as described in Subsection 1.4.1. The large-meander like path thus generated is associated with negative sea level difference between Kushimoto and Uragami from November 1993 to July 1994 (Fig.1.11a). The anticyclonic eddy indicated by the arrow in Fig.1.14a starts moving

westward. Then the eddy collides with the Kuroshio (Fig.1.14b) and is advected back eastward by the current. Associated with this process, the large-meander like path grows southeast of the Kii Peninsula (Fig.1.14b, 1.14c and 1.14d). This large-meander like path is strengthened by absorbing a cyclonic eddy east of the Izu-Ogasawara Ridge and then sheds a strong eddy, that is, a cyclonic ring. This results in a nearshore non-large-meander path (not shown).

The second large-meander like path occurs suddenly in January 1998 (Fig.1.15). The weak cyclonic eddy south of Shikoku is first captured by the Kuroshio, as indicated by the arrow in Fig.1.15a. The meander southeast of the Kii Peninsula grows just after that as shown in Fig.1.15b, 1.15c, and 1.15d. The second large-meander like path also absorbs the cyclonic eddy east of the Izu-Ogasawara Ridge, and then moves toward the east of the Izu-Ogasawara Ridge and returns to the non-large-meander (not shown).

In order to analyze the meander growth, the vertical velocity at 400m depth and the abyssal flow at 4000m depth are shown for the two large-meander cases and for one non-large meander case (Fig.1.16). Large anomalous downward velocity is found on the east half of the meander trough, whereas anomalous upward velocity is found on the west half. Abyssal anticyclonic circulation exists below the upper downwelling region. Cyclonic circulation occurs at mid-depth (2000–3000m), below the upwelling region (not shown). These features are consistent with the dynamical constraint of potential vorticity conservation. The large-meander like path (Fig.1.16a,b) is associated with the strengthened abyssal anticyclonic circulation around the Kosu Seamount and shows a contrast to the offshore non-large-meander path (Fig.1.16c), as previously simulated by Hurlburt et al. (1996) and Endoh and Hibiya (2001).

Figure 1.17 shows the kinetic energy at 4000m depth averaged in 31.5°-32.5°N, 132°-137°E. There are four peaks ($> 0.4 \times 10^{-4} m^2 s^{-2}$) during the simulation period. Three of them correspond to the large-meander paths and are indicated by arrows. The

fourth peak, in October 1994, is due to passage of the cyclonic eddy through the analysis region. The offshore non-large-meander (e.g., the peak on August 13, 1993) is associated with much smaller kinetic energy. The marked rise in the abyssal kinetic energy during the onset phase of the large-meander like path suggests vertical kinetic energy transfer due to baroclinic energy conversion. In the next subsection, we address the energetics of the meander growth.

1.4.3 Energetics of the meander growth

To examine how the meander grows, we have analyzed local energetics in a way similar to Masina et al. (1999) and Wells et al. (2000). The results are also compared with a standard linear stability analysis to clarify mechanisms of the initial growth. Although the simulated large-meander like paths are short-lived compared with the observed large-meander, the present analysis is useful in understanding the genesis of the large-meander like path.

The local energy transfer from mean kinetic energy to eddy kinetic energy associated with barotropic instability is expressed as follows:

$$K = -\left(\overline{u'u'} \frac{\partial \bar{u}}{\partial x} + \overline{u'v'} \left(\frac{\partial \bar{u}}{\partial y} + \frac{\partial \bar{v}}{\partial x} \right) + \overline{v'v'} \frac{\partial \bar{v}}{\partial y} \right). \quad (1.1)$$

where the overbar and prime quantities represent the mean and fluctuations in time; $\bar{u}(\bar{v})$ is the eastward (northward) mean velocity and $u'(v')$ is the eastward (northward) perturbed velocity. When K is positive, the barotropic energy transfer may generate disturbances. Magnitude of the vertical stress terms $-\left(\overline{u'w'} \frac{\partial \bar{u}}{\partial z} + \overline{v'w'} \frac{\partial \bar{v}}{\partial z} \right)$ is negligibly small compared with that of the horizontal deformation work terms (1.1) (not shown). Similarly, the energy transfer from mean potential energy to eddy kinetic energy is judged

by the following term:

$$P = -g \frac{\overline{u'\rho'} \frac{\partial \bar{\rho}}{\partial x} + \overline{v'\rho'} \frac{\partial \bar{\rho}}{\partial y}}{\frac{d\rho_b}{dz}} . \quad (1.2)$$

where g is the gravity acceleration, and $\rho', \bar{\rho}, \rho_b(z)$ are the perturbed, mean, and background density fields. When P is positive, the baroclinic energy transfer may generate disturbances. A part of P is transformed into eddy kinetic energy through the buoyancy term $B = -g \overline{\rho'w'}$, where w' is the perturbed vertical velocity. However, the complicated distribution of vertical velocity due to rough bottom topography prevents us from obtaining a meaningful view from the plot of B (Wells et al. 2000).

Figure 1.18a shows a meridional section at 136°E of the time-averaged eddy kinetic energy $(\overline{u'^2} + \overline{v'^2})/2$ during the period when the first meander grows. We find two peaks; one is at the Kuroshio core of the non-large-meander path (33°N) and another is on the offshore side of the Kuroshio (32.2°N). Meridional sections of the conversion terms K at 136°E (Fig.1.18b) show two positive K regions (on the onshore side at 33.7°N and on the offshore side at 32.7°N) within the upper 300m. On the other hand, the maximum of P is found at the Kuroshio core near 33°N (Fig.1.18c). This corresponds to the maximum of the eddy kinetic energy on the onshore side (Fig.1.18a). We also note that the positive P region extends to the main thermocline at 600m depth. This suggests that the evolving cyclonic disturbance due to baroclinic instability may influence the movement of the Kuroshio core of the non-large-meander path during the onset phase of the large-meander like path. Barotropic instability appears to be responsible for further growth of the meander because the maximum of the eddy kinetic energy on the offshore side at 32°N (Fig.1.18a) is accompanied only by the maximum in K . The energetics for the other large-meander like path show similar features (not shown). As shown in Fig.1.19, time series of three monthly mean eddy kinetic energy, barotropic conversion and baroclinic conversion averaged over

31°-33.5°N, 135°-136°E exhibit two peaks within the periods when the large-meander like path occurs.

Time series of both vertical and horizontal velocity shear averaged along the Kuroshio main stream show that the vertical shear of the Kuroshio increases prior to the onset of the large-meander like path (Fig.1.20). This leads to enhancement of the baroclinicity. The horizontal shear of the Kuroshio also increases prior to the large-meander like path, leading to a favorable condition for barotropic instability. Those pre-conditions permit the Kuroshio to generate the meander through the interaction with finite-amplitude disturbances, that is, meso-scale eddies. Zhu et al. (2001) also observed increase of both vertical and horizontal shear of the Kuroshio south of Shikoku prior to the path transition from the nearshore to the offshore non-large-meander during the period from 1994 to 1995.

We, therefore, analyze the stability of the preconditioned Kuroshio using a two-dimensional inviscid primitive equation model (cf. Xue and Mellor 1993). The preconditioned velocity profile at longitude of 136°E from 31°N to 33.5°N is used for the analysis. The bottom topography and the velocity profile are approximated using the analytical functions as described in the Appendix 1. Figure 1.21 shows the growth rate and the phase speed for the unstable modes corresponding to above two meanders. The most preferred mode has an e-folding time of 3.0-3.4 days and wavelength of 240-260km. The phase speed for the most unstable wave is 35 km/day and does not show significant dependence on the downstream wave number. Characteristics of the most unstable mode are summarized in Table 1.2. The energetics of the unstable mode is calculated using the baroclinic conversion term P, the buoyancy term B and the barotropic conversion term K. As shown in Table 1.2, the ratios of B and K to P show that baroclinic energy transfer is mainly responsible for the growth of the unstable wave.

Similar characteristics of the meander simulated by the OGCM were estimated from the sequences of sea surface height (Table 1.3). The ratio of K/P estimated in the onshore

region for the OGCM indicates that the baroclinic instability dominates in the onshore side during the initial growth. On the other hand, barotropic instability is responsible for the growth in the offshore region. The simulated meander grows and moves more slowly than expected from the linear stability analysis. The wavelength is larger than the theoretical prediction. The structure of the unstable disturbance (Fig.1.22a) does not correspond well to that of the simulated disturbance in the OGCM (Fig.1.18a). The vertical structures for the barotropic conversion term K and the baroclinic conversion P (Fig.1.22b, c) are not so similar to those in the OGCM (Fig.1.18b, c). The linear stability analysis can not well explain the meander growth in the OGCM.

1.4.4 Variation of the Kuroshio recirculation

The present analysis of the model results suggests that the pre-conditioned Kuroshio may generate the large-meander like path through the interaction between the Kuroshio and either an anticyclonic or a cyclonic eddy. According to Kagimoto and Yamagata (1997), the anticyclonic Kuroshio recirculation is intensified by a merger of anticyclonic eddies. Therefore we discuss roles of the Kuroshio recirculation at the preconditioning phase. To achieve this, analysis of the vorticity budget is useful.

The vorticity budget is calculated using the following equation (Ezer and Mellor 1994; Kagimoto and Yamagata 1997).

$$\frac{\partial}{\partial t} \left(\frac{\partial(\bar{v}D)}{\partial x} - \frac{\partial(\bar{u}D)}{\partial y} \right) = - \left(\frac{\partial A_y}{\partial x} - \frac{\partial A_x}{\partial y} \right) - \left(\frac{\partial(f\bar{u}D)}{\partial x} + \frac{\partial(f\bar{v}D)}{\partial y} \right) + J(P_b, D) + \text{curl}(\tau_s - \tau_b) \quad (1.3)$$

where D is the depth, (\bar{u}, \bar{v}) are the vertical averaged velocities, (A_x, A_y) are the vertically integrated advection plus diffusion terms in the zonal and the meridional momentum equations, respectively, f is the Coriolis parameter, P_b is the bottom pressure, and τ_s, τ_b are the wind and the bottom stresses, respectively. J denotes the Jacobian operator. The term on the left hand side is the vorticity tendency term, and the terms on the

right hand side are the advection plus diffusion of the vorticity, the planetary geostrophic divergence, the bottom pressure torque, and the curl of wind and bottom stresses. The second term on the right hand side of Equation (1.3) is reduced to the planetary beta effect when the time dependence of the surface elevation is negligible (Kagimoto and Yamagata 1997).

Figure 1.23a shows the time series of vorticity ($\partial \bar{v}D/\partial x - \partial \bar{u}D/\partial y$) averaged in the Kuroshio recirculation region (30° - 33° N, 133° - 140° E). The area-averaged anticyclonic (i.e., negative) vorticity is significantly intensified just before the occurrence of the large-meander like path. The anticyclonic vorticity averaged in the area excluding the cyclonic meander region shows a more drastic variation. The time evolution of all terms in (1.3) is shown in Fig.1.23b. We note that diffusion is negligible in comparison with advection; the wind stress is negligible in comparison with the bottom stress in this region.

During the non-large-meander period, the negative beta-advection and nonlinear advection terms are almost balanced with the positive bottom pressure and stress torques. This suggests that the Kuroshio interacts with the bottom slope through the bottom pressure torque during the period. The advection intensifies the anticyclonic vorticity during the non-large-meander period; each negative peak of the advection term corresponds to intrusion of the anticyclonic eddies. In particular, the anticyclonic vorticity is supplied by the advection from summer of 1992 to autumn of 1993 in the model (Fig.1.12, 1.13).

When the first large-meander like path occurs, the balance among terms drastically changes. The beta-advection term changes from a negative value to a positive value owing to the strong southward flow. The nonlinear advection term and bottom stress torque frequently change sign owing to large variation of the cyclonic meander and the anticyclonic recirculation. Because of lack of constant supply, the anticyclonic vorticity in the recirculation region weakens during the large-meander period. The second

large-meander like path occurs after the anticyclonic vorticity is again significantly intensified in summer of 1997. In the end of 1996, although the anticyclonic vorticity is intensified, the meander does not grow. Figure 1.24 suggests that rapid decline in the anticyclonic vorticity due to interaction between the anticyclonic and cyclonic eddies may affect the Kuroshio path.

The time series of the model Kuroshio volume transport across the PN and ASUKA lines suggests a cause of the intensification of the Kuroshio recirculation (Fig.1.25). The volume transport across the PN line increases seasonally when the anticyclonic eddies pass through the PN line in summer (Kagimoto and Yamagata 1997). The interannual increase of the Kuroshio volume transport across the PN line during the period from 1993 to 1994 and the period from 1997 to 1998 is also due to the interannual enhancement of the eddy activity. Since the anticyclonic eddies intrude into the Kuroshio recirculation region and circulates in the region (see Fig.1.12, 1.13), the volume transport across the ASUKA line is highly variable. The intensification of the anticyclonic Kuroshio recirculation corresponds to merger of anticyclonic eddies traced back to the region of the northeast of the Luzon Island (e.g., Fig.1.12). In 1995, the recirculation is reduced by intrusion of a cyclonic eddy despite the merger of the anticyclonic eddies from the upstream region.

Both theoretical and observational studies (e.g., White and McCreary 1976; Kawabe 1995) suggest that the Kuroshio path south of Japan is related to variation of the volume transport and the surface velocity at upstream locations, e.g., the PN line. Figure 1.26 shows relations among the Kuroshio volume transport, the surface velocity, and the large meander like path from the present model. The large-meander like path is basically associated with large transport and large surface velocity on an interannual time scale. This is consistent with another model result, (Kagimoto 1999), and supports the relation obtained from observations (Kawabe 1995). This typical tendency corresponds to the first meander from November 1993 to July 1994. However, the large-meander like path exists

even when the transport and surface velocity are near normal. The latter case corresponds to the second meander from January 1998 to May 1998. We suggest that the supply of anticyclonic eddies from the upstream region as shown by the increase of the volume transport in 1997 destabilizes the Kuroshio prior to the second meander (Fig.1.25a).

1.5 Summary

We have discussed the results from the OGCM experiment for the period from 1992 through 1998 using the high-resolution nested grid model for the North Pacific. It has turned out that the present model successfully reproduces several important features. Those features are: 1) the propagation of anticyclonic eddies and their merger with the Kuroshio recirculation in the Shikoku Basin, 2) frequent occurrence of the offshore non-large-meander owing to the interaction between the Kuroshio and the anticyclonic eddy, 3) the intensification of the Kuroshio recirculation (identified by the increase of volume transports across the ASUKA lines) due to supply of anticyclonic vorticity prior to the large-meander like path, 4) the large-meander like path triggered by the interaction between the anticyclonic eddy and the strong Kuroshio recirculation, and 5) the demise of the meander after shedding the cyclonic ring intensified by the merger of the cyclonic eddy.

A synthesis of these results leads to the following scenario for the formation of the Kuroshio large-meander. At the beginning, anticyclonic eddies are activated near Taiwan or the Philippine coast and advected by the Kuroshio into the Shikoku Basin. The transport across the PN line increases by the successive arrival of those anticyclonic eddies and the anticyclonic Kuroshio recirculation south of Shikoku is intensified by the merger of those eddies. Then, the Kuroshio large-meander is generated through the interaction between the intensified Kuroshio recirculation and the anticyclonic/cyclonic eddies. During the meandering period, the meandering cyclonic jet matures by absorbing a cyclonic ring

propagating from the Kuroshio Extension and eventually sheds the cyclonic ring. Thus, the large-meander state ends. The above scenario suggests the importance of eddy activities to the Kuroshio meandering and provides a key to predict the ever-mysterious phenomenon of the Kuroshio meander; the eddy activities introduce a favorable condition for the Kuroshio large-meander through intensification of the Kuroshio recirculation. Since the simulated large-meander like path is unstable, the scenario provides no favorable conditions for the long-lived meander.

So far, observational studies have suggested that the Kuroshio large-meander occurs through generation of a small meander southeast of Kyushu (so-called trigger meander according to Solomon (1978)). The present model shows that the anticyclonic/cyclonic eddies propagate westward along 29° - 32° N (see Fig.1.6d) and interact directly with the Kuroshio south of Shikoku. Since the actual eddies may interact with the Kuroshio southeast of Kyushu, the concept of the trigger meander might have captured this possible phenomenon (Endoh and Hibiya 2001).

The simulated large-meander like path does not persist long and it changes into the offshore non-large-meander. The meander east of the Izu-Ogasawara Ridge and the cyclonic eddy south of the Kuroshio Extension influence the stability of the large-meander in the model (see Fig.1.14 and 1.15). This study suggests that the persistence of the Kuroshio large-meander is strongly affected by the meso-scale eddies generated by flow instabilities. Ichikawa and Imawaki (1994) reported the merger of the Kuroshio large-meander and the cyclonic eddy originated from the Kuroshio Extension using Geosat data. They did not clarify how this event influenced the amplitude of the large-meander. More intensive observational studies are certainly needed to clarify the interaction of meso-scale eddies with the Kuroshio path variation.

In the present simulation, the large-meander like path occurs through the intensification of the Kuroshio recirculation caused by the interannual variation of the Kuroshio transport

across the PN line. The volume transport of the Kuroshio increases through the amplification of the anticyclonic eddies originated in the region near the Luzon Island as indicated by the local maximum of the EKE there (Fig.1.5b; also see Fig.1.12, 1.13a,d). More detailed analysis of eddy activity near the Luzon Island is certainly necessary.

Appendix.1: Linear stability analysis

Linear instability of the velocity profile of the Kuroshio is investigated using a two-dimensional, inviscid primitive equation model (cf. Xue and Mellor 1993) to clarify mechanisms of the initial growth of the meander. The governing equations for the disturbances are

$$\left. \begin{aligned} \frac{\partial u}{\partial t} + U \frac{\partial u}{\partial x} - fv + v \frac{\partial U}{\partial y} + w \frac{\partial U}{\partial z} + \frac{1}{\rho_0} \frac{\partial p}{\partial x} &= 0 \\ \frac{\partial v}{\partial t} + U \frac{\partial v}{\partial x} + fu + \frac{1}{\rho_0} \frac{\partial p}{\partial y} &= 0 \\ b - \frac{1}{\rho_0} \frac{\partial p}{\partial z} &= 0 \\ \frac{\partial u}{\partial x} + \frac{\partial v}{\partial y} + \frac{\partial w}{\partial z} &= 0 \\ \frac{\partial b}{\partial t} + U \frac{\partial b}{\partial x} + v \frac{\partial B}{\partial y} + w \frac{\partial B}{\partial z} &= 0 \end{aligned} \right\} \quad (1.A.1)$$

where u, v and w represent x, y , and z components of the perturbation velocity vector; p is the perturbation pressure, and b is the perturbation buoyancy, $b = -g\rho(y, z)/\rho_0$. A steady current $U(y, z)$ is assumed to flow in parallel to the coast, which is in thermal wind balance, for example, $fU_z = B_y$ where subscripts indicate partial derivatives. The boundary conditions are

$$\left. \begin{aligned} v &= 0 & \text{at} & \quad y = 0 \\ p, u, v &\rightarrow 0 & \text{as} & \quad y \rightarrow \infty \\ w &= 0 & \text{at} & \quad z = 0 \\ w &= -v \frac{\partial h}{\partial y} & \text{at} & \quad z = -h(y) \end{aligned} \right\} \quad (1.A.2)$$

For later convenience, we introduce a bottom-following coordinate:

$$\zeta = 1 + \frac{z}{h(y)} \quad (1.A.3)$$

Then the vertical velocity is transformed into

$$\omega = w - (\zeta - 1)v \frac{\partial h}{\partial y}. \quad (1.A.4)$$

We assume perturbed disturbances of the form

$$\left. \begin{aligned} u &= \text{Re}[\tilde{u}(y, \zeta) \exp(i(\sigma + kx))] \\ v &= \text{Re}[i\tilde{v}(y, \zeta) \exp(i(\sigma + kx))] \\ u &= \text{Re}[\tilde{\omega}(y, \zeta) \exp(i(\sigma + kx))] \\ b &= \text{Re}[i\tilde{b}(y, \zeta) \exp(i(\sigma + kx))] \\ p &= \text{Re}[i\tilde{p}(y, \zeta) \exp(i(\sigma + kx))] \end{aligned} \right\} \quad (1.A.5)$$

where k is the downstream wave number and $\sigma = \sigma_r + i\sigma_i$, the frequency. The above system is solved by the spectral technique. It has turned out that a truncation level of 28 is sufficient to obtain a converged solution. Interested readers are referred to Xue and Mellor (1993) for details of the spectral technique.

In the present analysis, the meridional section of Kuroshio from 31° to 33.5° N at 136° E is adopted. The bottom topography including a sharp continental slope is approximated by the following function (Xue and Mellor 1993):

$$h(y) = H_s + \frac{1}{2}(H_d - H_s) \left\{ 1 + \tanh \frac{y - y_m}{\alpha} \right\}, \quad (1.A.6)$$

where H_s and H_d are the minimum depth and the maximum depth in the domain, respectively. The width of the slope is given by α and the maximum slope, $\frac{H_d - H_s}{2\alpha}$, is realized at $y = y_m$. The four parameters (H_s, H_d, α, y_m) are given by 1110m, 4600m, 20km, 80km, respectively; they are determined by the least squares method from the model topography. The background velocity and horizontal gradient of buoyancy field are given by the following formula as in Xue and Mellor (1993).

$$\begin{aligned}
U(y, z) &= U_0 \exp\left(\frac{z}{z_s} - Y_i^2\right) \\
Y_i = Y_i(y) &= \left[y - y_f \left(1 - \frac{z}{z_s A}\right)\right] \frac{1}{y_d} \\
A &= A_0 + 2 \frac{z}{H_d} \\
y_d &= \begin{cases} y_{d1} - \frac{z(y_{d2} - y_{d1})}{H_d} - \frac{y_{d2} - y_{d1}}{H_d} & (\text{if } Y_i \leq 0) \\ y_{d2} & (\text{if } Y_i > 0) \end{cases} \\
B_y(y, z) &= \frac{fU_0}{z_s} \left\{ 1 - 2Y_i \left(\frac{y_f A_0}{y_d A^2} - Y_i \frac{z_s}{y_d} \frac{dy_d}{dz} \right) \right\} \exp\left(\frac{z}{z_s} - Y_i^2\right) \\
\frac{dy_d}{dz} &= \begin{cases} -\frac{y_{d2} - y_{d1}}{H_d} & (\text{if } Y_i \leq 0) \\ 0 & (\text{if } Y_i > 0) \end{cases}
\end{aligned} \tag{1.A.7}$$

where U_0 is the maximum velocity of the Kuroshio, y_f is the distance of the location of the surface velocity maximum from the northern boundary, y_d is the width of the Kuroshio, z_s is the velocity decreasing rate against depth, and A is the southward tilt of the maximum velocity with increasing depth. The above six parameters ($U_0, z_s, y_f, y_{d1}, y_{d2}, A_0$) are determined by the least squares method for the 10-day mean velocity data just before the meander occurs. Parameters on 12 October 1993 and on 9 January 1998 are summarized in Table 1.A.1. To obtain $B(y, z)$, $B_y(y, z)$ in (1.A.7) is integrated numerically. The integration begins at the southern boundary since isodensity surface are nearly flat. Profiles of U and B are shown in Fig.1.A.1.

Tables

Table 1.1 Sigma coordinate used in the high-resolution model

Layers	Sigma coordinate	Layers	Sigma coordinate
1	0.000	26	-0.325
2	-0.002	27	-0.350
3	-0.005	28	-0.375
4	-0.010	29	-0.425
5	-0.015	30	-0.475
6	-0.025	31	-0.525
7	-0.035	32	-0.575
8	-0.045	33	-0.625
9	-0.055	34	-0.675
10	-0.065	35	-0.725
11	-0.075	36	-0.775
12	-0.085	37	-0.825
13	-0.095	38	-0.875
14	-0.105	39	-0.900
15	-0.120	40	-0.925
16	-0.135	41	-0.950
17	-0.150	42	-0.970
18	-0.165	43	-0.980
19	-0.180	44	-0.990
20	-0.195	45	-1.000
21	-0.210		
22	-0.225		
23	-0.250		
24	-0.275		
25	-0.300		

Table 1.2 Characteristics of the most unstable wave for two velocity profiles. B/P denotes the ratio of the buoyancy term B to the baroclinic conversion term P , and K/P denotes the ratio of the barotropic conversion term to the baroclinic conversion term P .

	growth rate (1/day)	phase speed (km/day)	wavelength (km)	K/P	B/P
Profile on 12 Oct. 1993	3.4×10^{-1}	35	260	0.120	0.863
Profile on 9 Jan .1998	2.9×10^{-1}	35	240	0.077	0.875

Table 1.3 Characteristics of the meanders simulated by the OGCM. K/P in the onshore region denotes the ratio of the barotropic conversion term to the baroclinic conversion term P in 32.5° - 33.5° N, 135° - 136° E, and K/P denotes that in 31.0° - 33.5° N, 135° - 136° E.

	growth rate (1/day)	phase speed (km/day)	wavelength (km)	K/P in the onshore region	K/P
Meander on Oct. 1993	0.7×10^{-1}	12	600	0.208	0.655
Meander on Jan .1998	0.7×10^{-1}	6	720	0.221	0.427

Table 1.A.1 Parameters of two velocity profiles

	$U_0(m/s)$	$Z_s(m)$	$y_f(km)$	$y_{d1}(km)$	$y_{d2}(km)$	A_0
Profile on 12 Oct. 1993	1.60	650	110	36	74	3.5
Profile on 9 Jan .1998	1.38	655	100	34	66	4.3

Figures

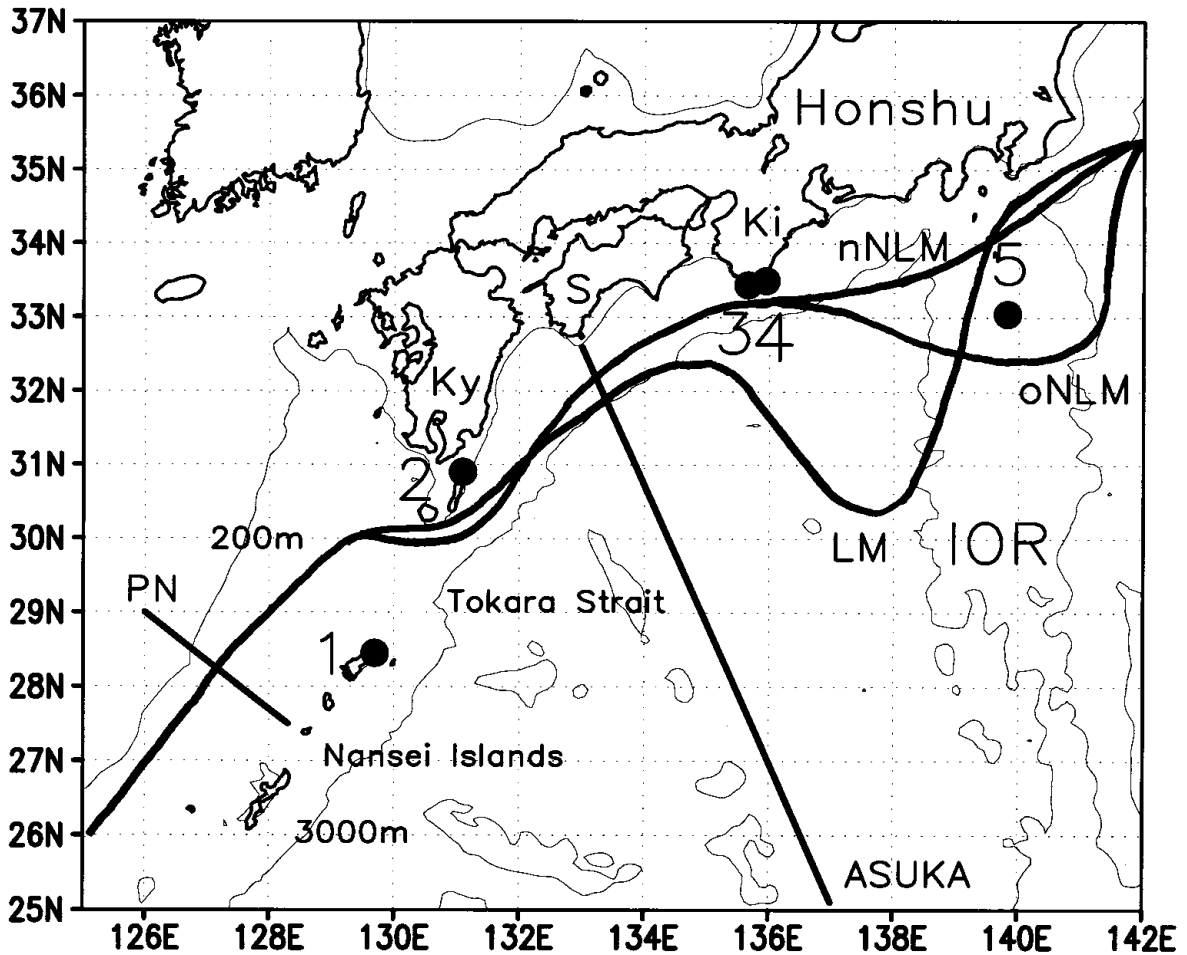


Figure 1.1 Tide gage stations and typical paths (LM: large-meander path, oNLM: offshore non-large-meander path, nNLM: nearshore non-large-meander path) of the Kuroshio. The numbers denote the tide stations and the abbreviations represent locations; 1: Naze, 2: Nishinoomote, 3: Kushimoto, 4: Uragami, 5: Hachijojima, Ki: Kii Peninsula, S: Shikoku, Ky: Kyushu, and IOR the Izu-Ogasawara Ridge. We note that Uragami (4) is located slightly downstream of Kushimoto (3). PN and ASUKA denote the CTD line of the JMA Nagasaki Marine Observatory and the line of the ASUKA observation group, respectively.

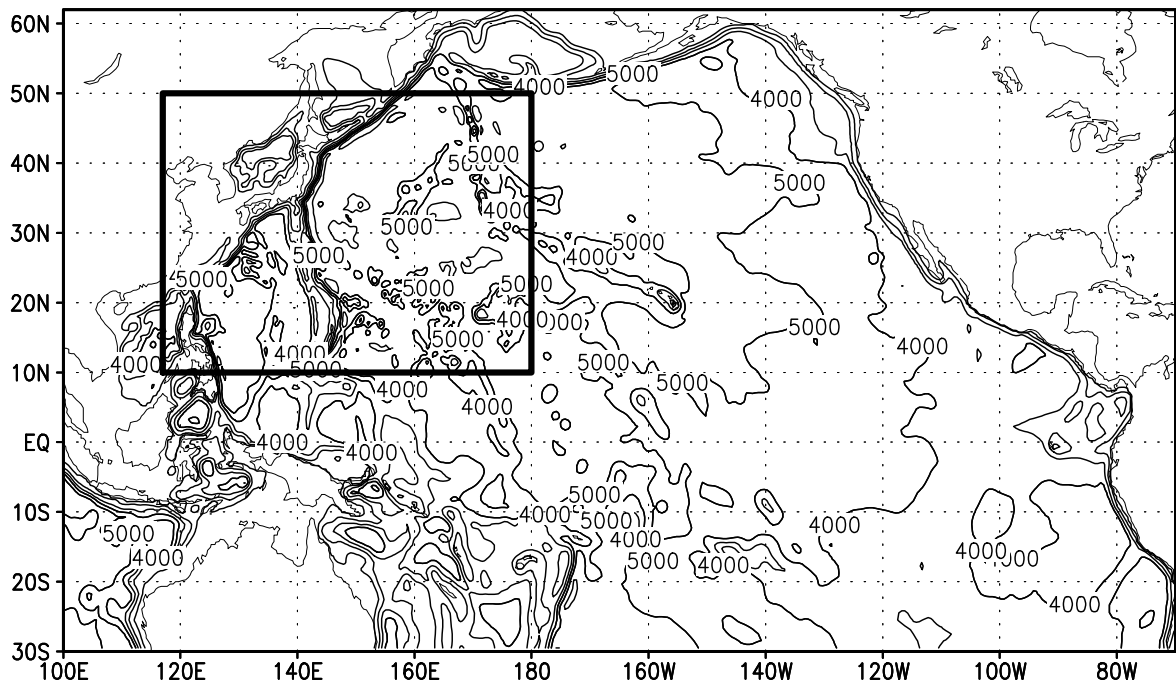


Figure 1.2 Bottom topography. The nested area is indicated with a bold rectangle.

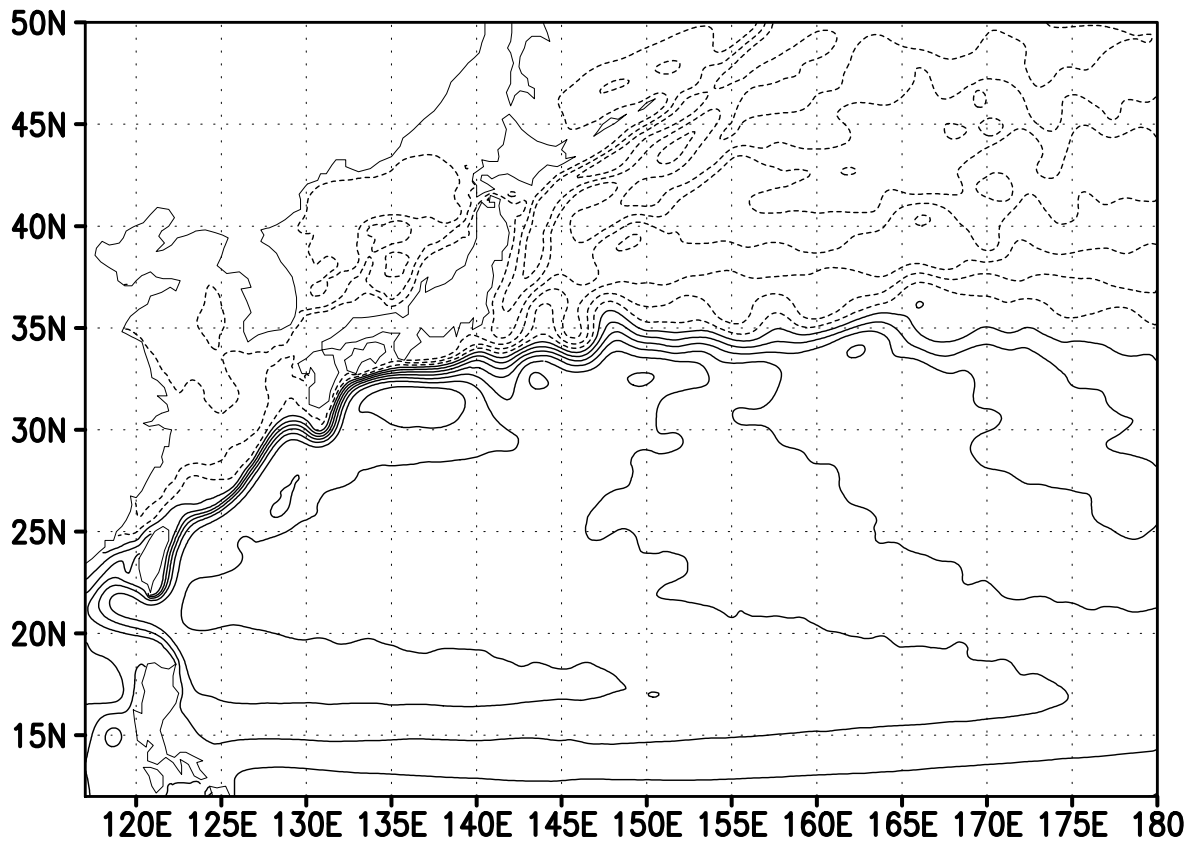


Figure 1.3 Mean sea surface height of the model from 1992 to 1998. Contour interval is 0.1 m.

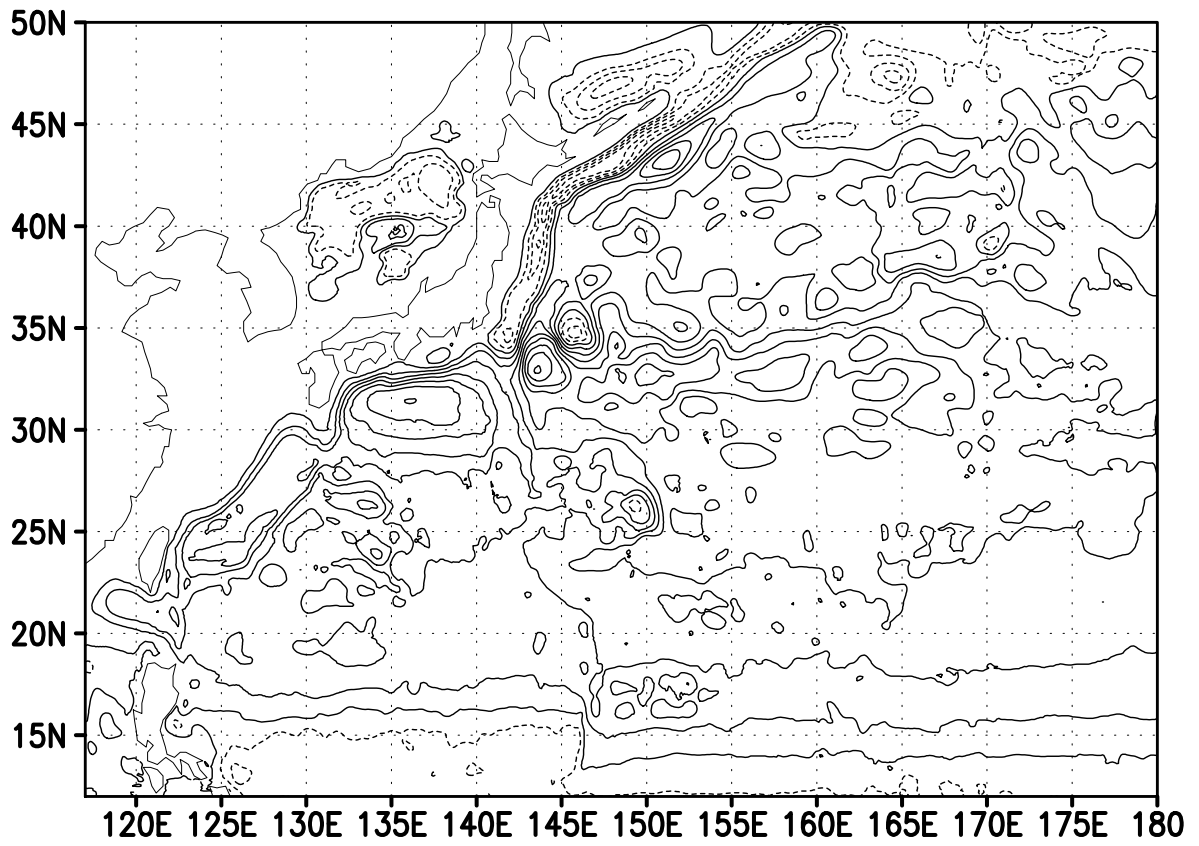
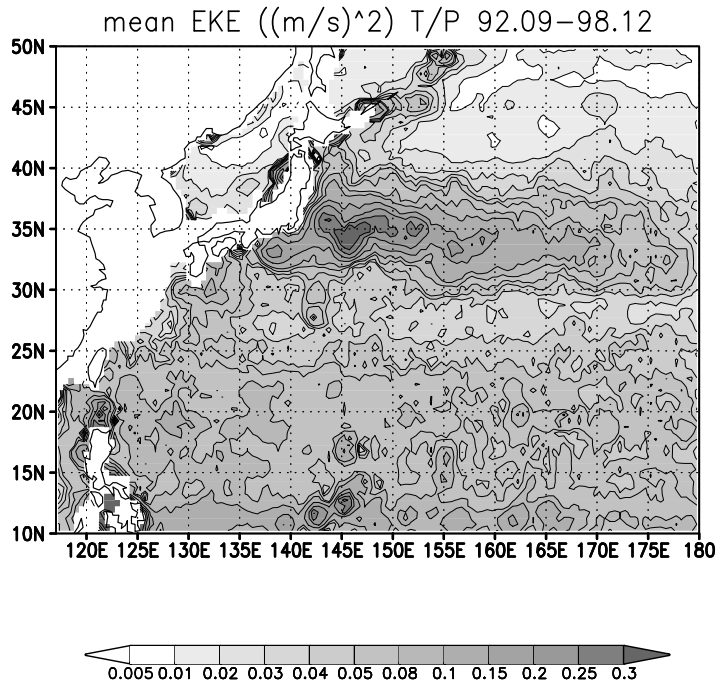


Figure 1.4 Mean streamfunction of the model from 1992 to 1998. Contour interval is 10 Sv.

(a)



(b)

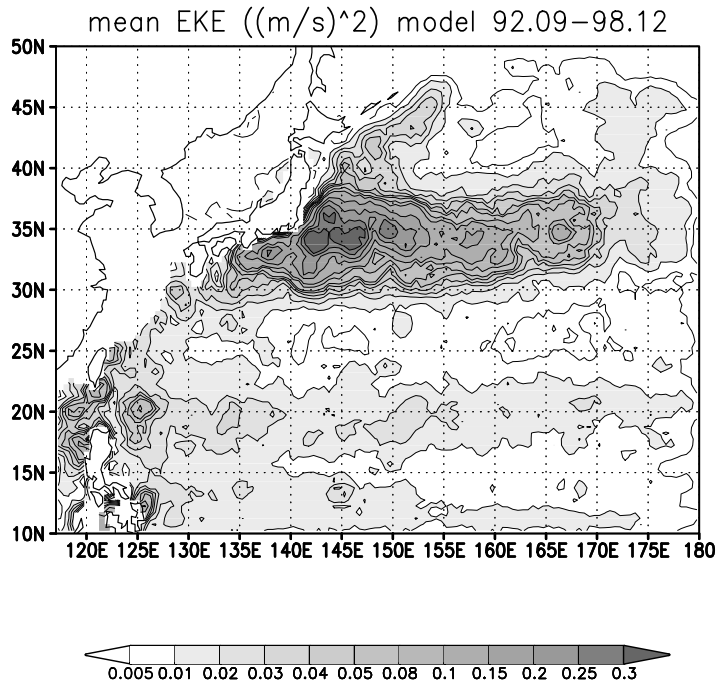


Figure 1.5 Mean eddy kinetic energy (in ms^2) calculated from sea surface height anomaly (September 1992–December 1998). (a) TOPEX/POSEIDON altimetry. (b) Model result.

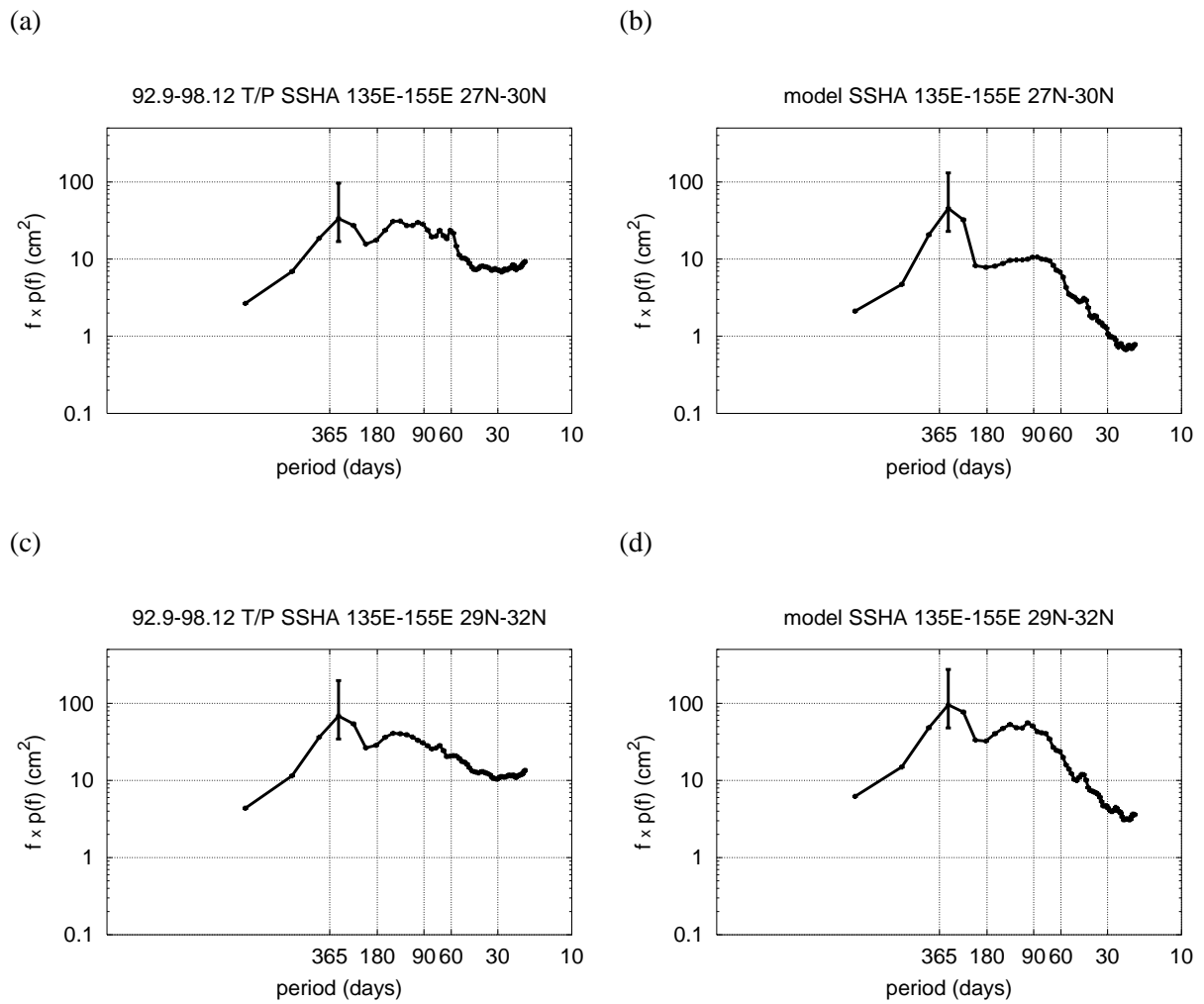
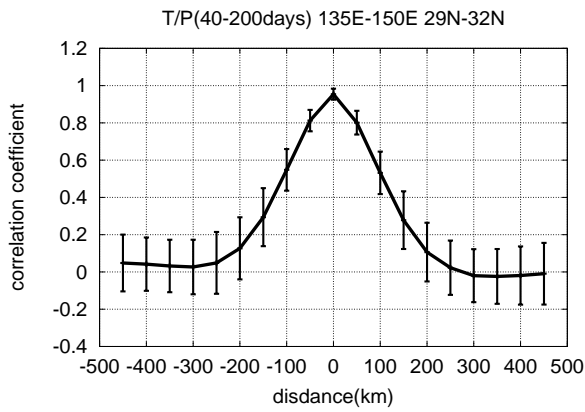


Figure 1.6 Power spectra of sea surface height anomaly. (a) TOPEX/POSEIDON data averaged in the region (27°-30°N, 135°-155°E), (b) the model result averaged in the region (27°-30°N, 135°-155°E), (c) TOPEX/POSEIDON data averaged in the region (29°-32°N, 135°-155°E), and (d) the model result averaged in the region (29°-32°N, 135°-155°E). An error bar indicating 95% confidence level is shown in each figure.

(a)



(b)

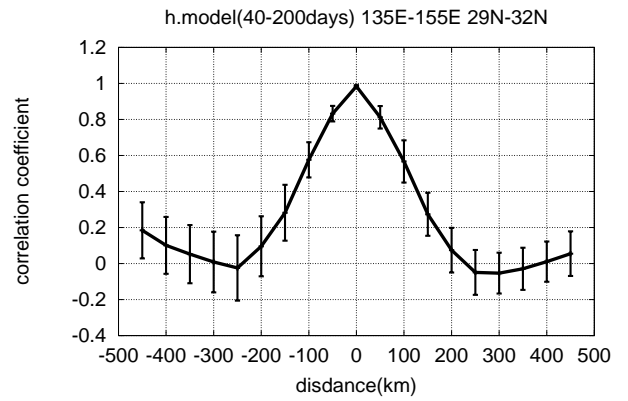
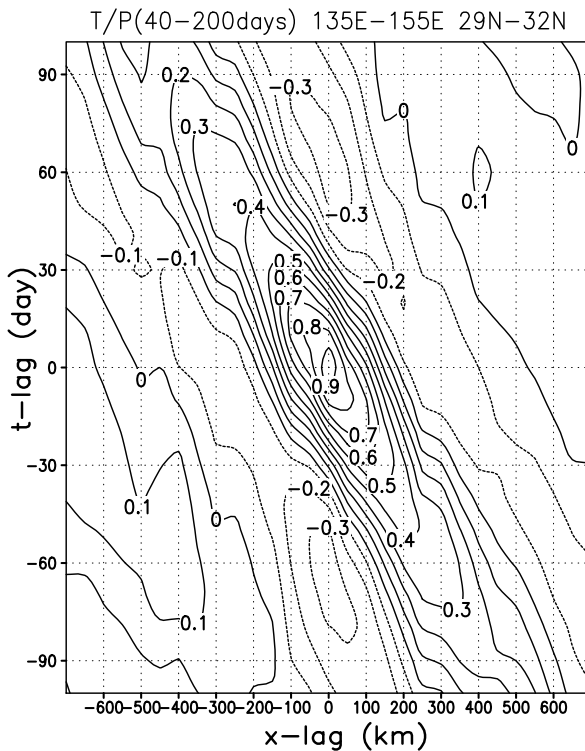


Figure 1.7 Along-track lag correlation of filtered sea surface height anomaly averaged in the region (29°-32°N, 135°-155°E). (a) TOPEX/POSEIDON. (b) the model result. Standard deviation is plotted with interval of 50km lag.

(a)



(b)

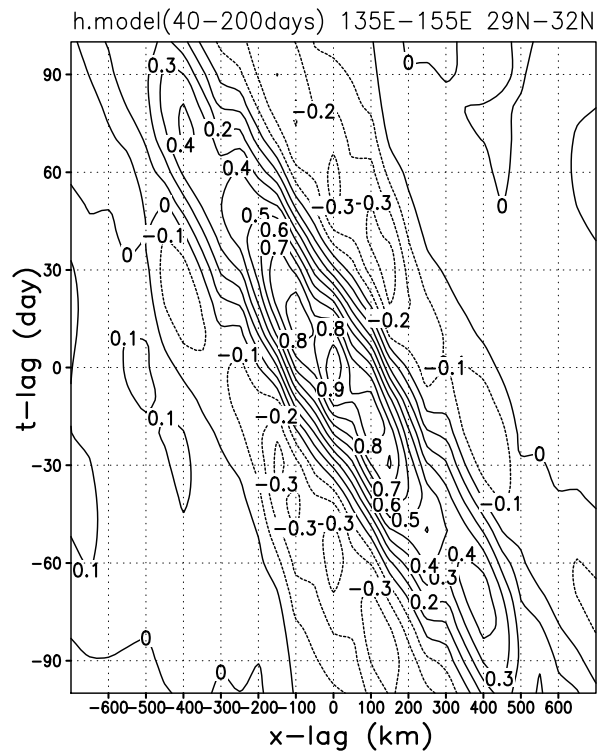


Figure 1.8 As in Fig.1.7 except for cross-track space-time lag correlation.

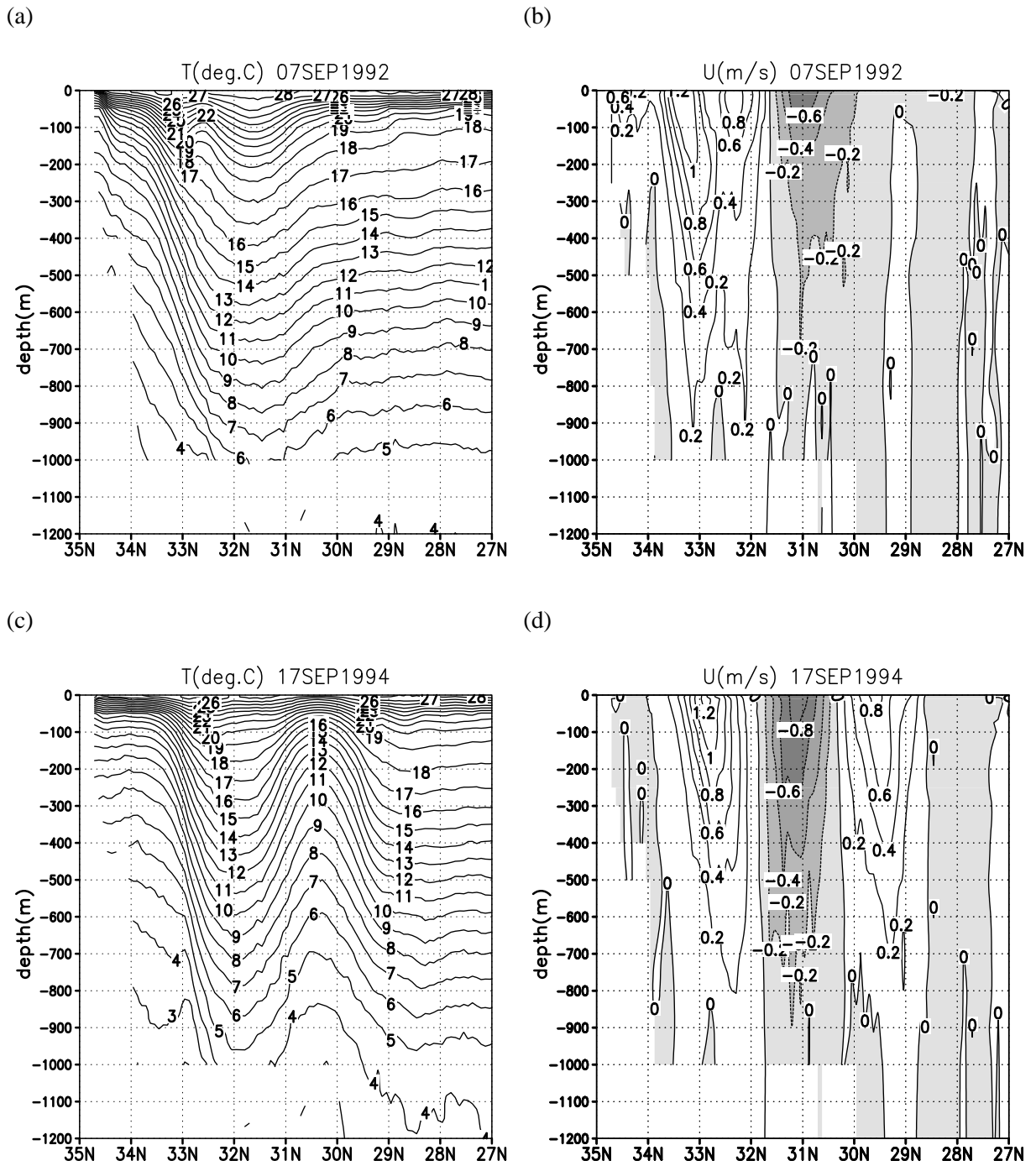


Figure 1.9 Depth-latitude sections at 139°E. (a) Temperature and (b) eastward velocity of a simulated anticyclonic eddy on 7 September 1992. (c) Temperature and (d) eastward velocity of a simulated cyclonic eddy on 17 September 1994. Contour interval of temperature is 1°C and that of velocity is 0.2 ms^{-1} .

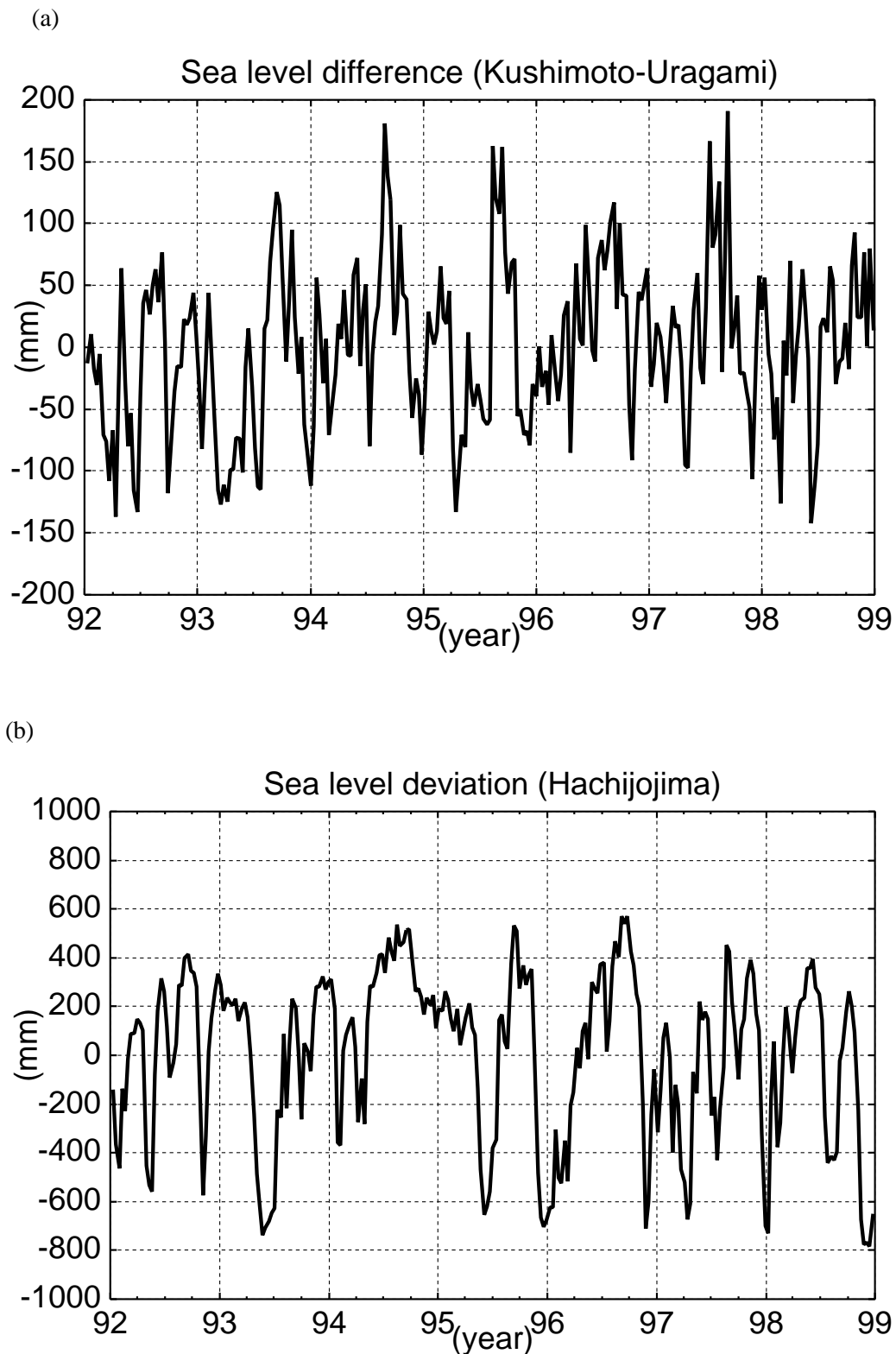


Figure 1.10 (a) Time series of observed sea level difference between Kushimoto and Uragami. (b) Time series of observed sea level at Hachijojima. Both data are averaged over 10 days and the reference value is the mean for the period from January 1992 to December 1998. The sea level data were corrected for barometric pressure using daily mean values.

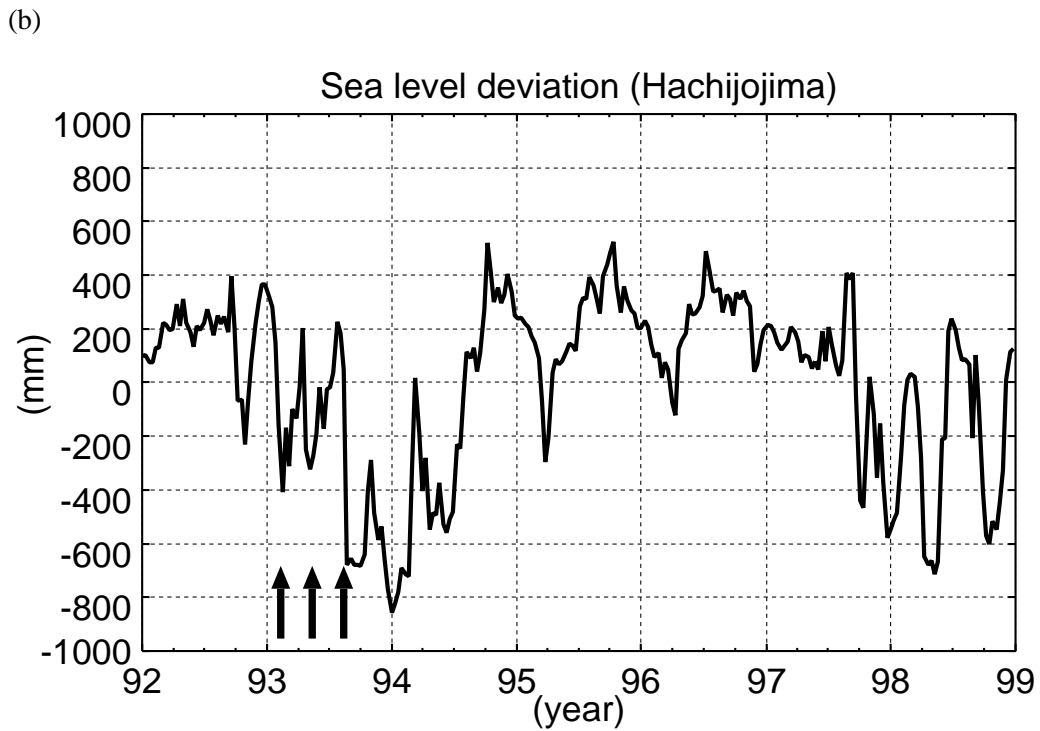
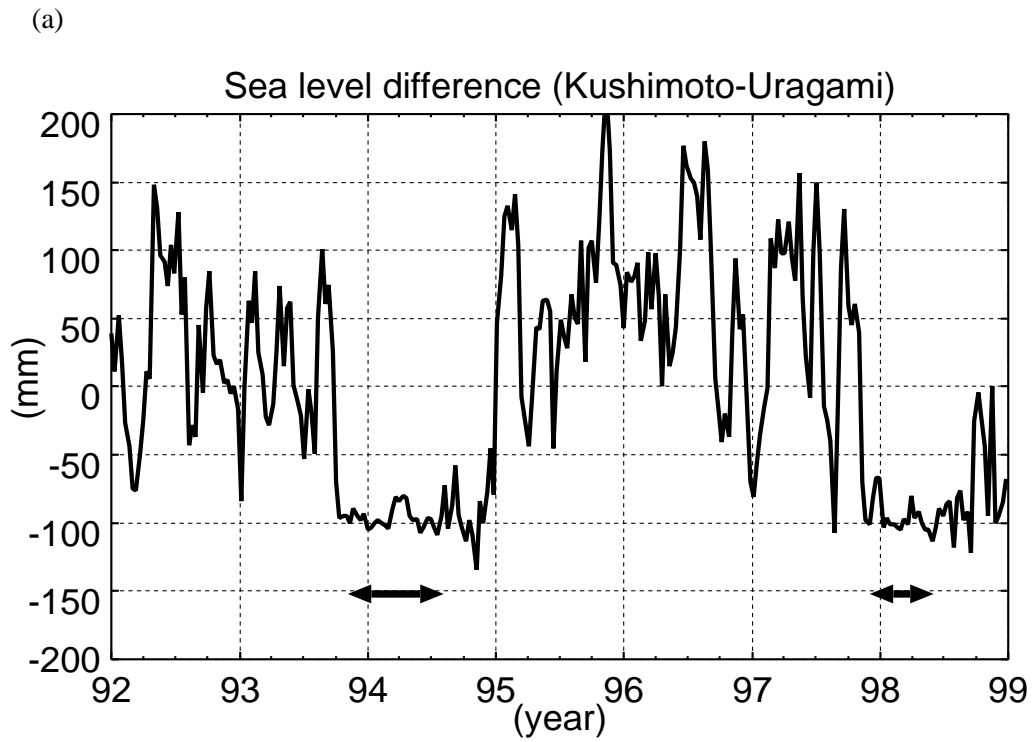


Figure 1.11 As in Fig.1.10 except for the model result. Lines with arrows denote the large-meander period. The arrows denote the onset of the offshore non-large-meander path.

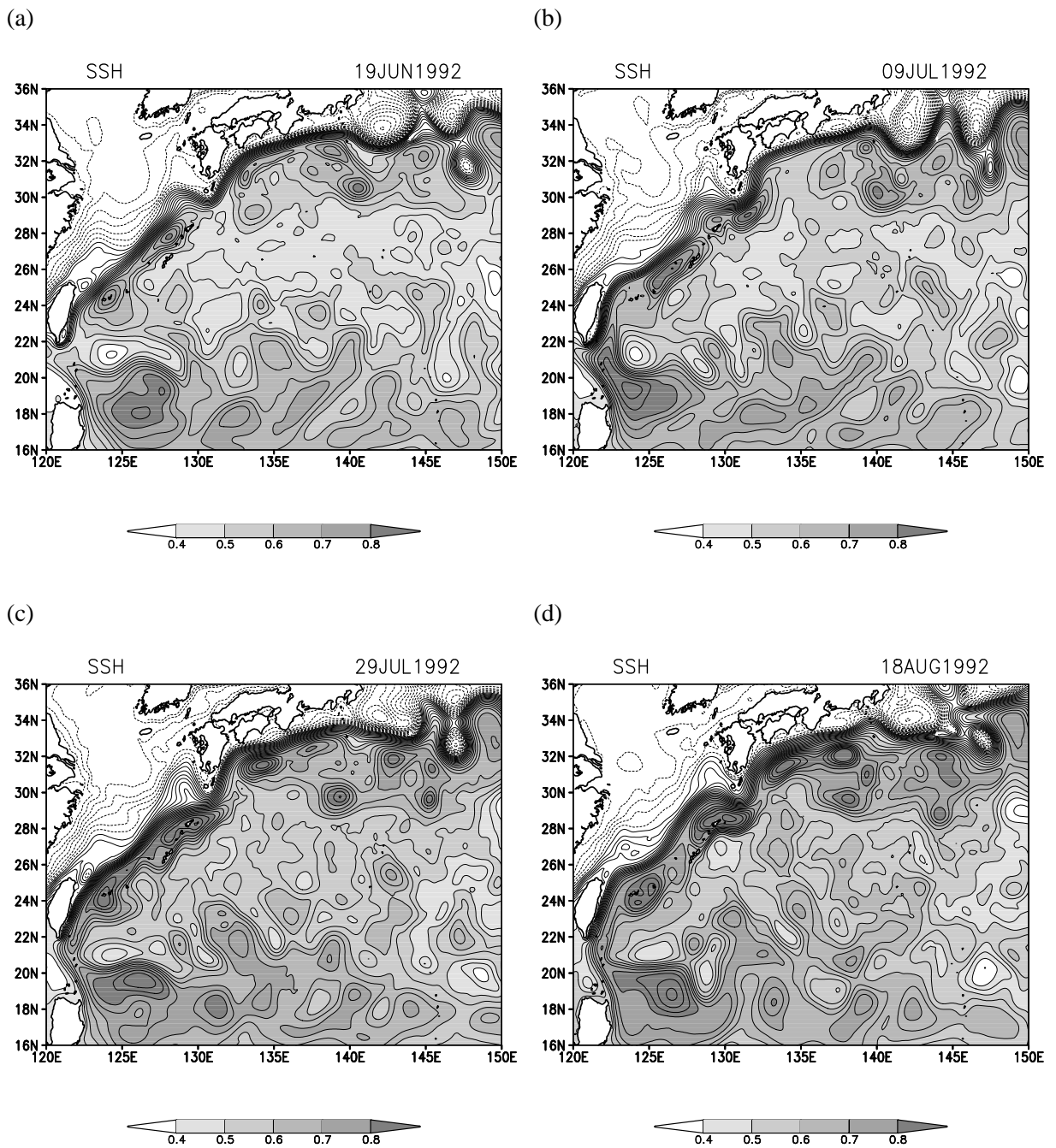


Figure 1.12 Evolution of sea surface height showing the downstream propagation of the anticyclonic eddies Contour interval is 0.05m. Regions $> 0.6\text{m}$ are shaded. (a) 19 June 1992. (b) 9 July 1992. (c) 29 July 1992. (d) 18 August 1992.

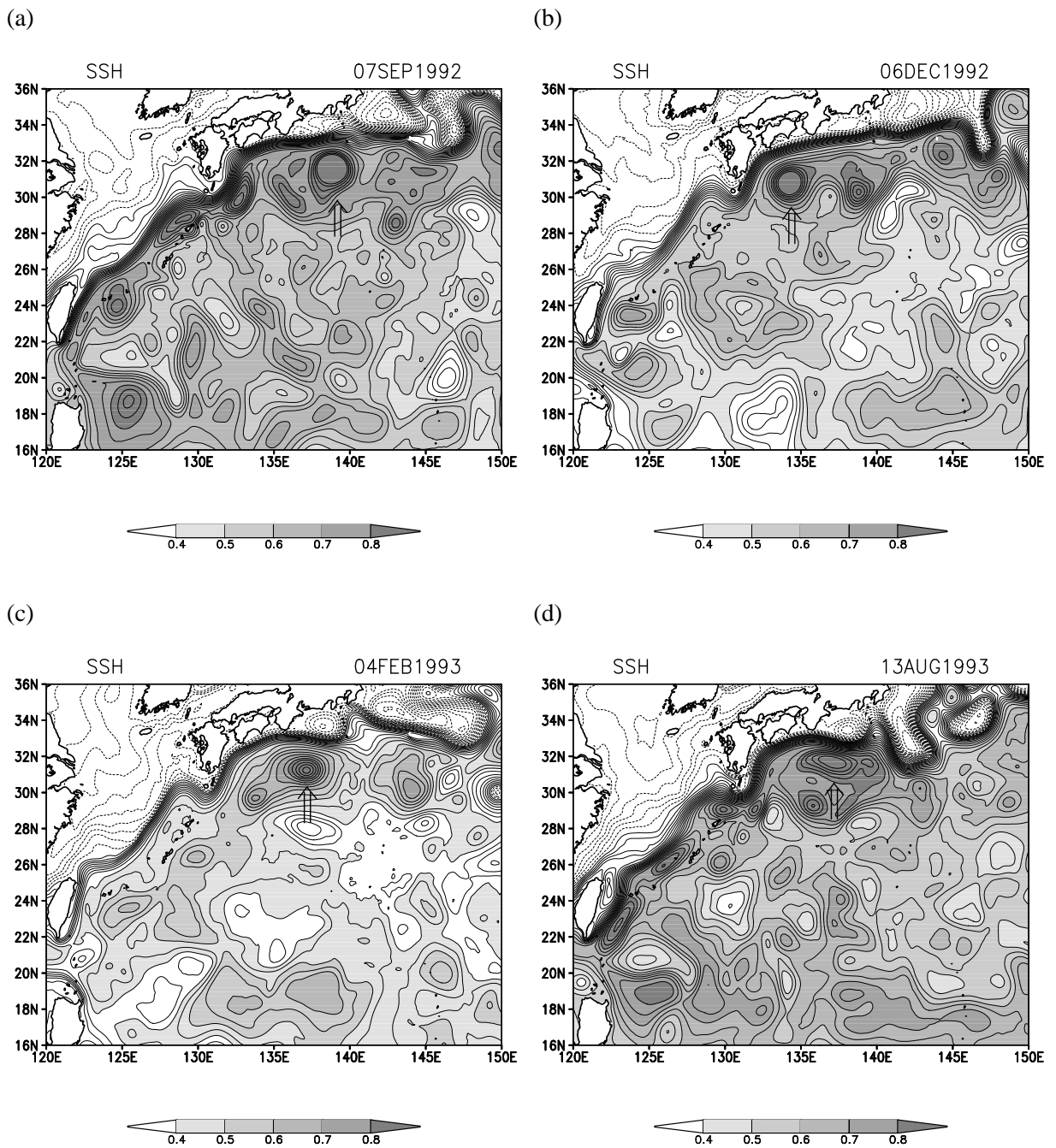


Figure 1.13 As in Fig.1.12 except for showing the interaction of the anticyclonic eddy (indicated by arrows) and the Kuroshio. (a) 7 September 1992. (b) 6 December 1992. (c) 4 February 1993. (d) 13 August 1993.

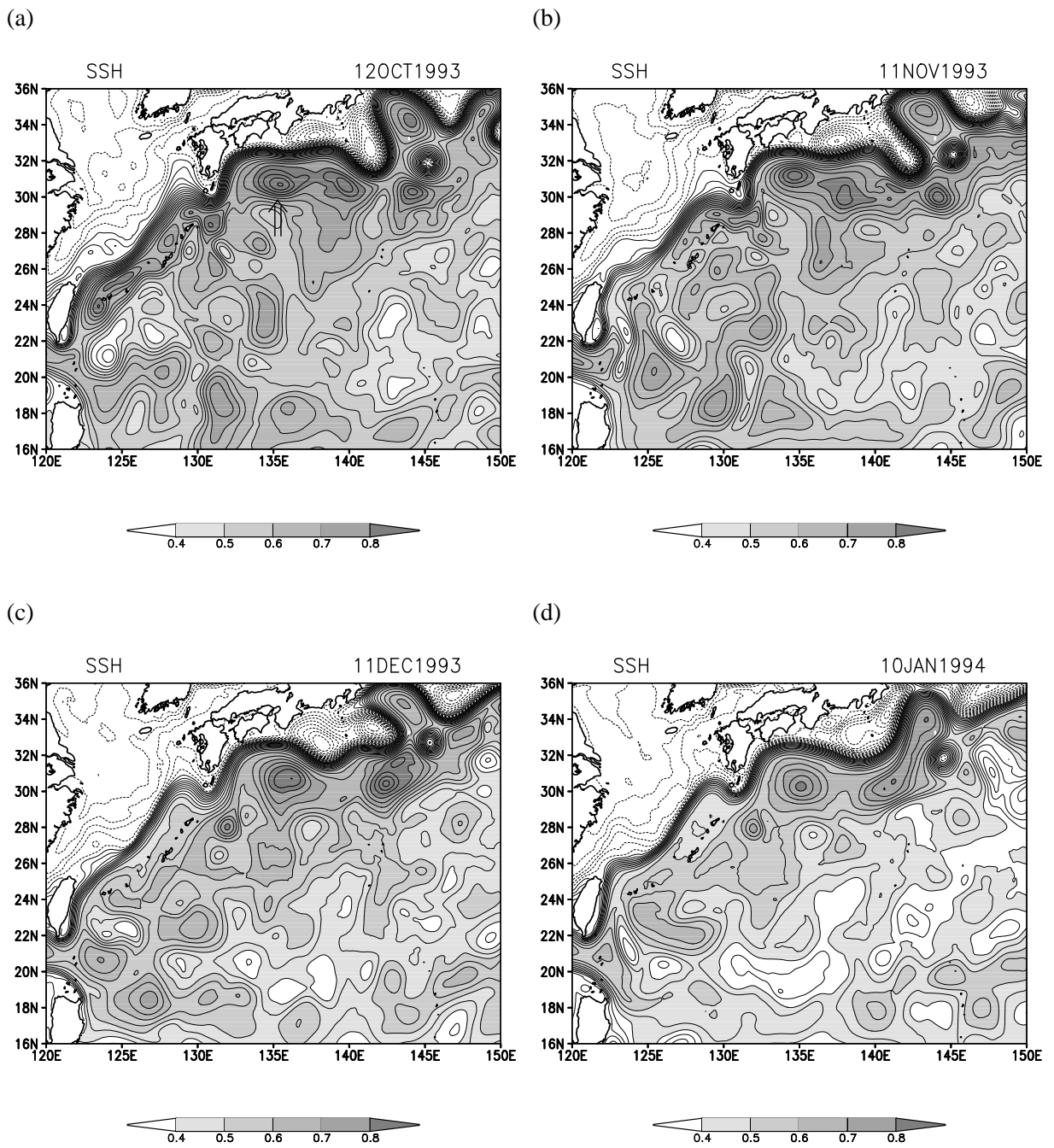


Figure 1.14 As in Fig.1.12 except for showing the amplification of the Kuroshio meander due to the interaction with the anticyclonic eddy (indicated by an arrow in (a)). (a) 9 February 1994. (b) 1 March 1994. (c) 21 March 1994. (d) 10 April 1994.

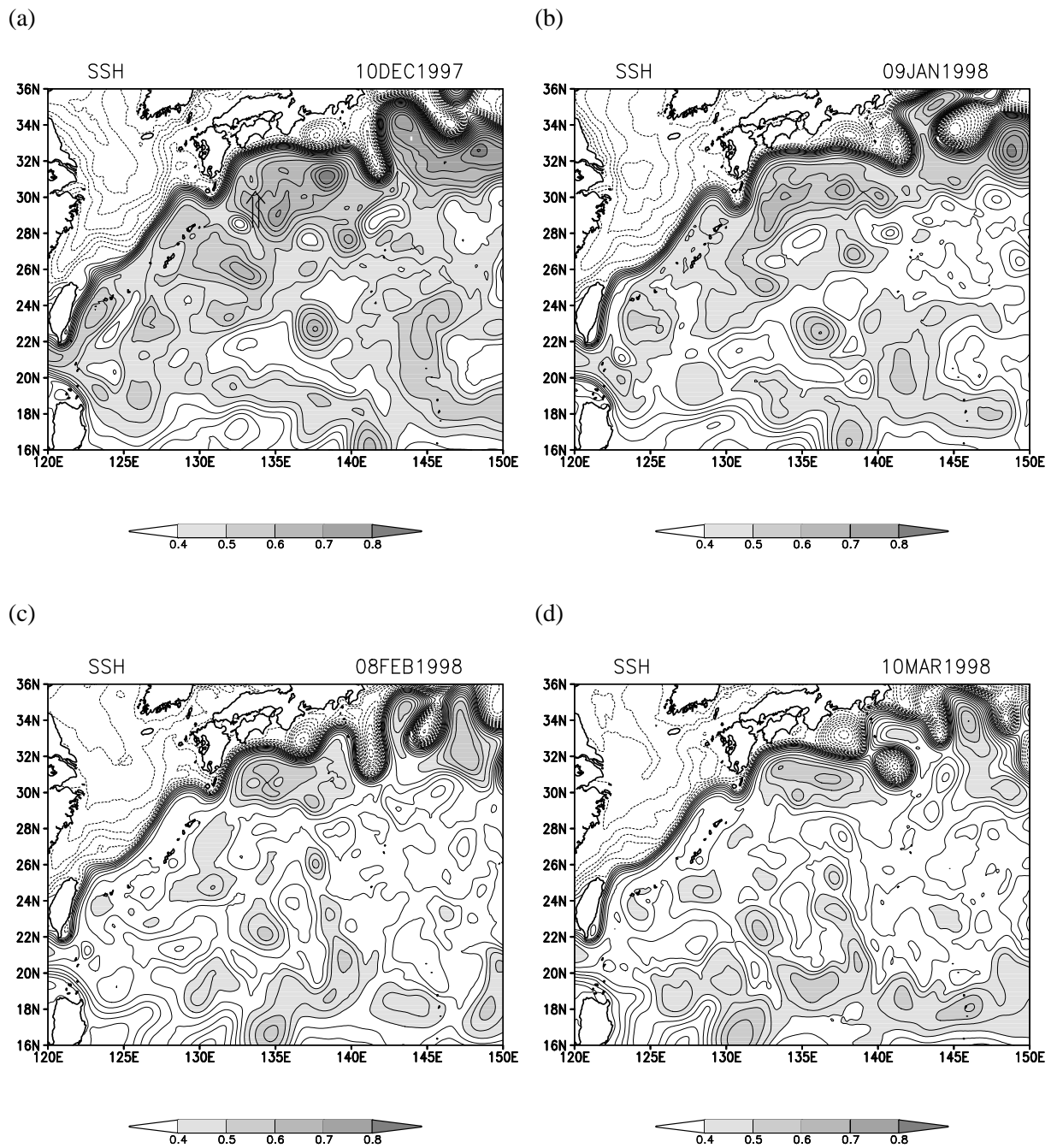


Figure 1.15 As in Fig.1.12 except for showing the amplification of the Kuroshio meander due to the interaction with the cyclonic eddy (indicated by an arrow in (a)). (a) 10 December 1997. (b) 9 January 1998. (c) 8 February 1998. (d) 10 March 1998.

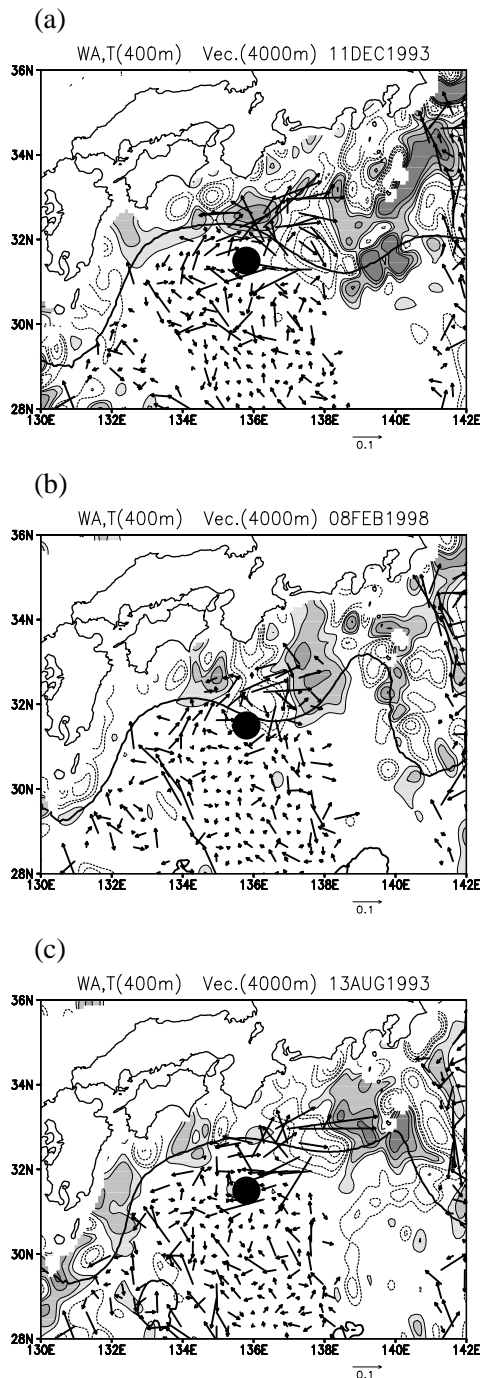


Figure 1.16 Snapshots of the smoothed vertical velocity at 400m of depth. (a) The large-meander case on 13 August 1993. (b) The large-meander case on 21 March 1994. (c) The offshore non-large meander case on 8 February 1998. The shaded region denotes upwelling and the dashed contour denotes downwelling. The Koshu Seamount is indicated by a closed circle in each panel. The contour interval is $-0.03, -0.02, -0.01, -0.005, 0.005, 0.01, 0.02, 0.03 \text{ cms}^{-1}$. The horizontal velocity at 4000m depth is also shown by the vectors. To show the Kuroshio path, the temperature contour of 13°C at 400m depth is denoted by the thick line.

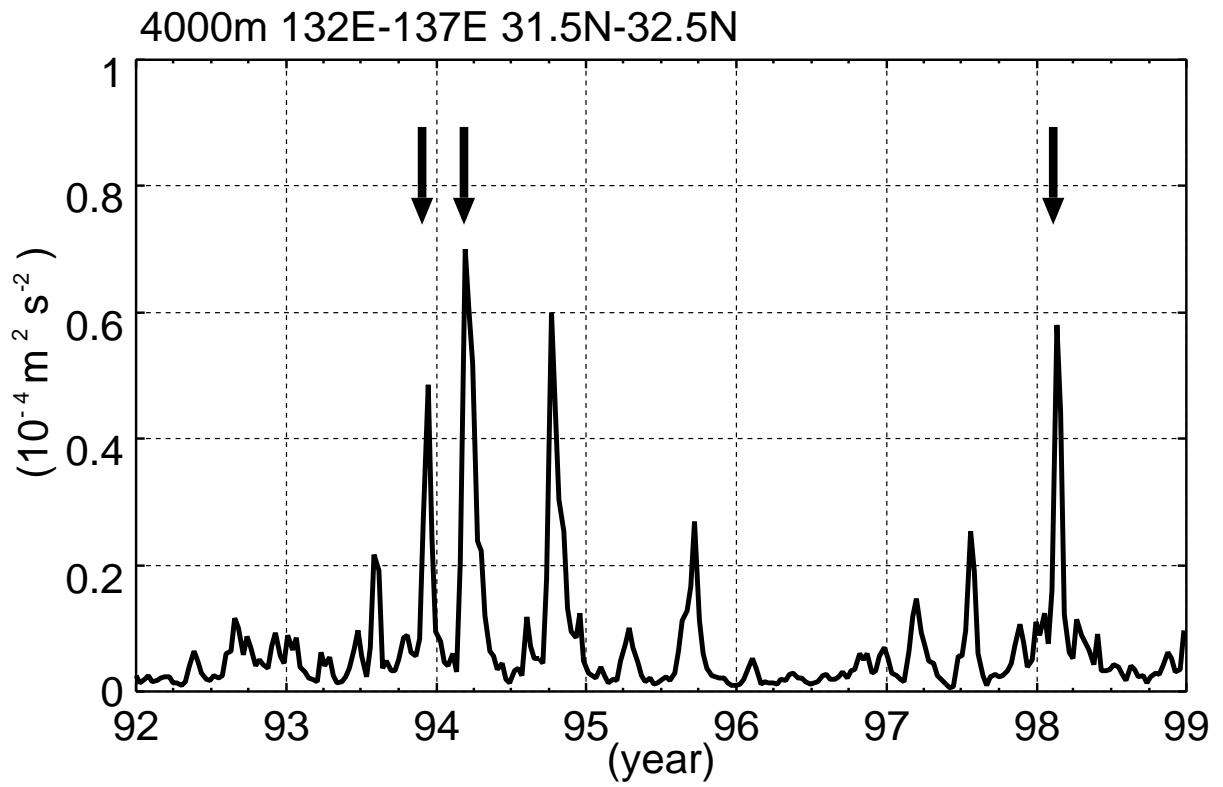


Figure 1.17 Time series of kinetic energy at 4000m depth averaged over 31.5°-32.5°N, 132°-137°E.

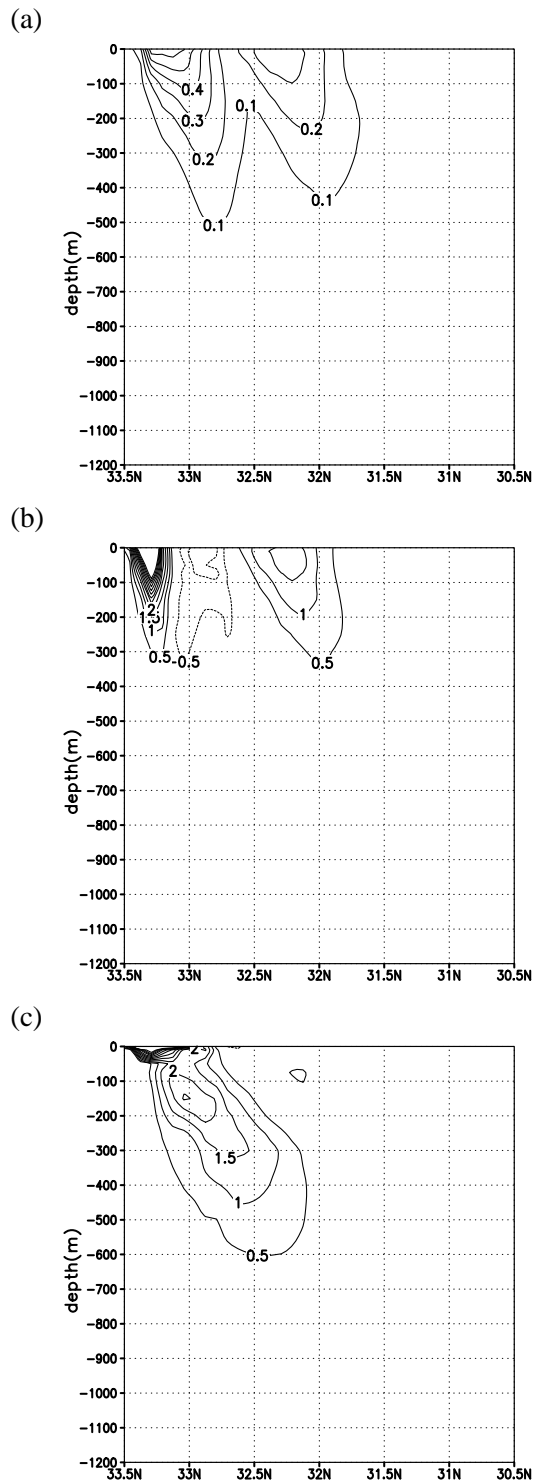


Figure 1.18 Depth-latitude sections at 136E for (a) time mean eddy kinetic energy (contour interval is $0.1 \text{ m}^2\text{s}^{-2}$), (b) time mean barotropic conversion (contour interval is $0.5 \times 10^{-6} \text{ m}^2\text{s}^{-3}$), and (c) time mean baroclinic conversion (contour interval is $0.5 \times 10^{-6} \text{ m}^2\text{s}^{-3}$). The period of time mean is from 2 October 1993 to 10 January 1994. A diamond in (a) indicates mean position of the Kuroshio.

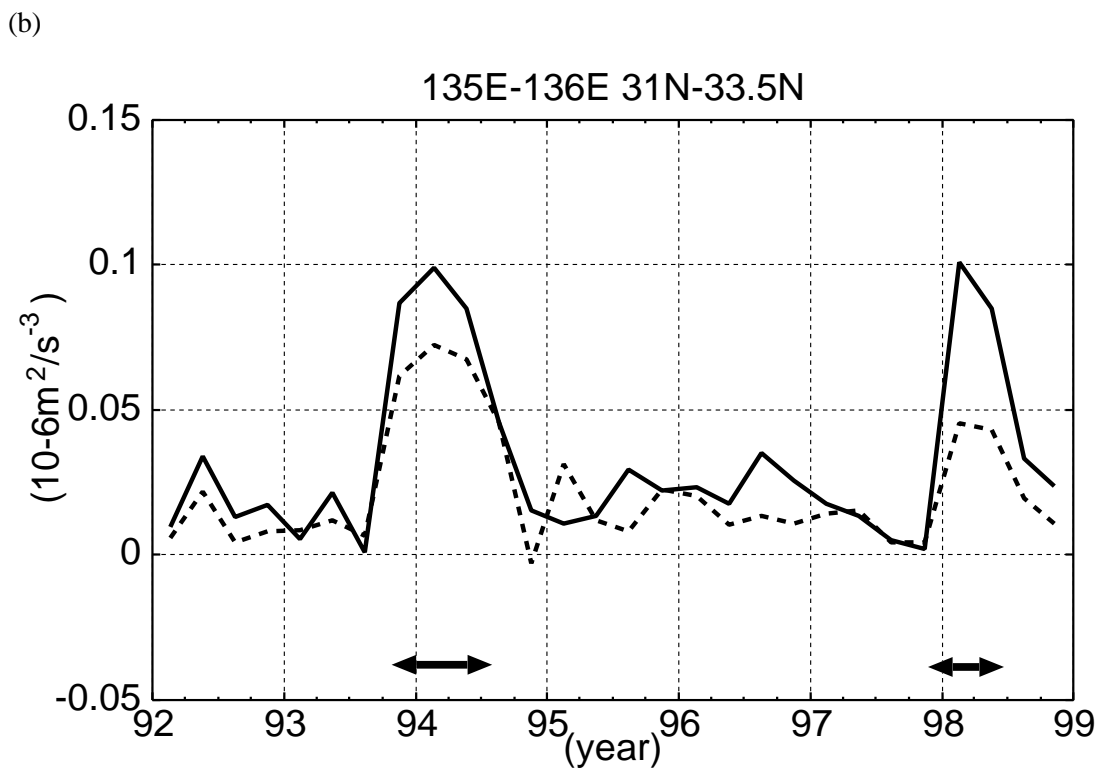
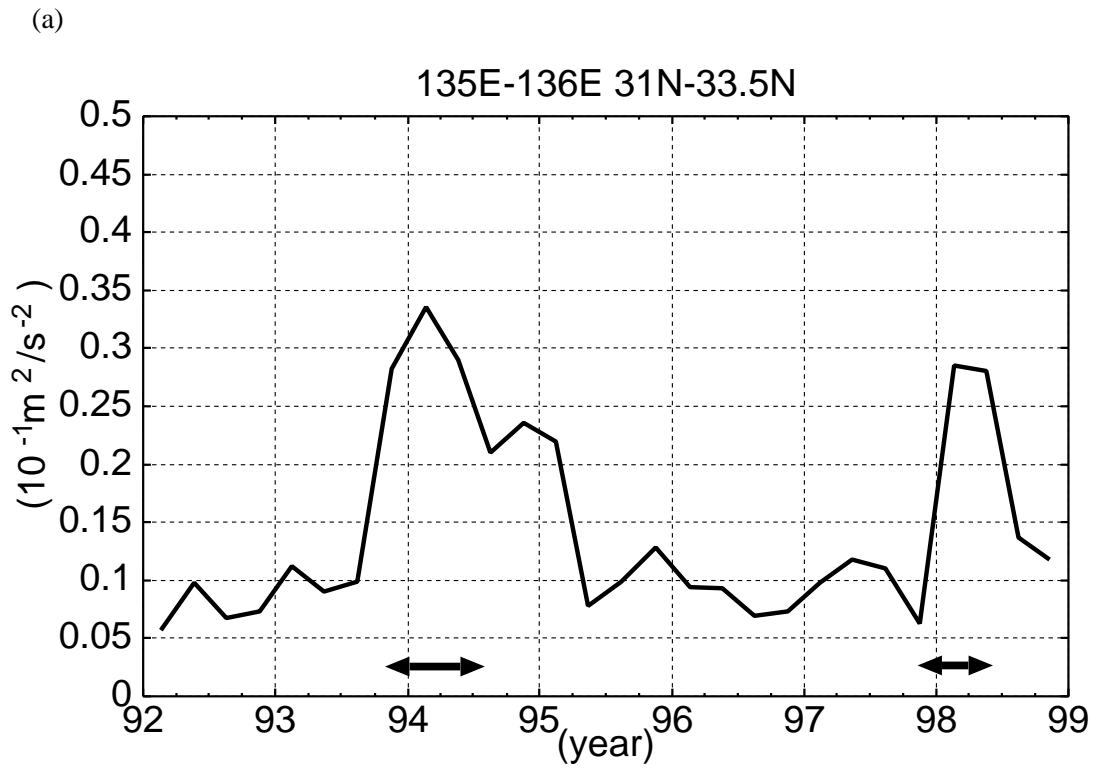


Figure 1.19 (a) Time series of three monthly mean kinetic energy averaged over 31° - 33.5° N, 135° - 136° E. (b) As in (a) except for baroclinic conversion (thick line) and barotropic conversion (dashed line).

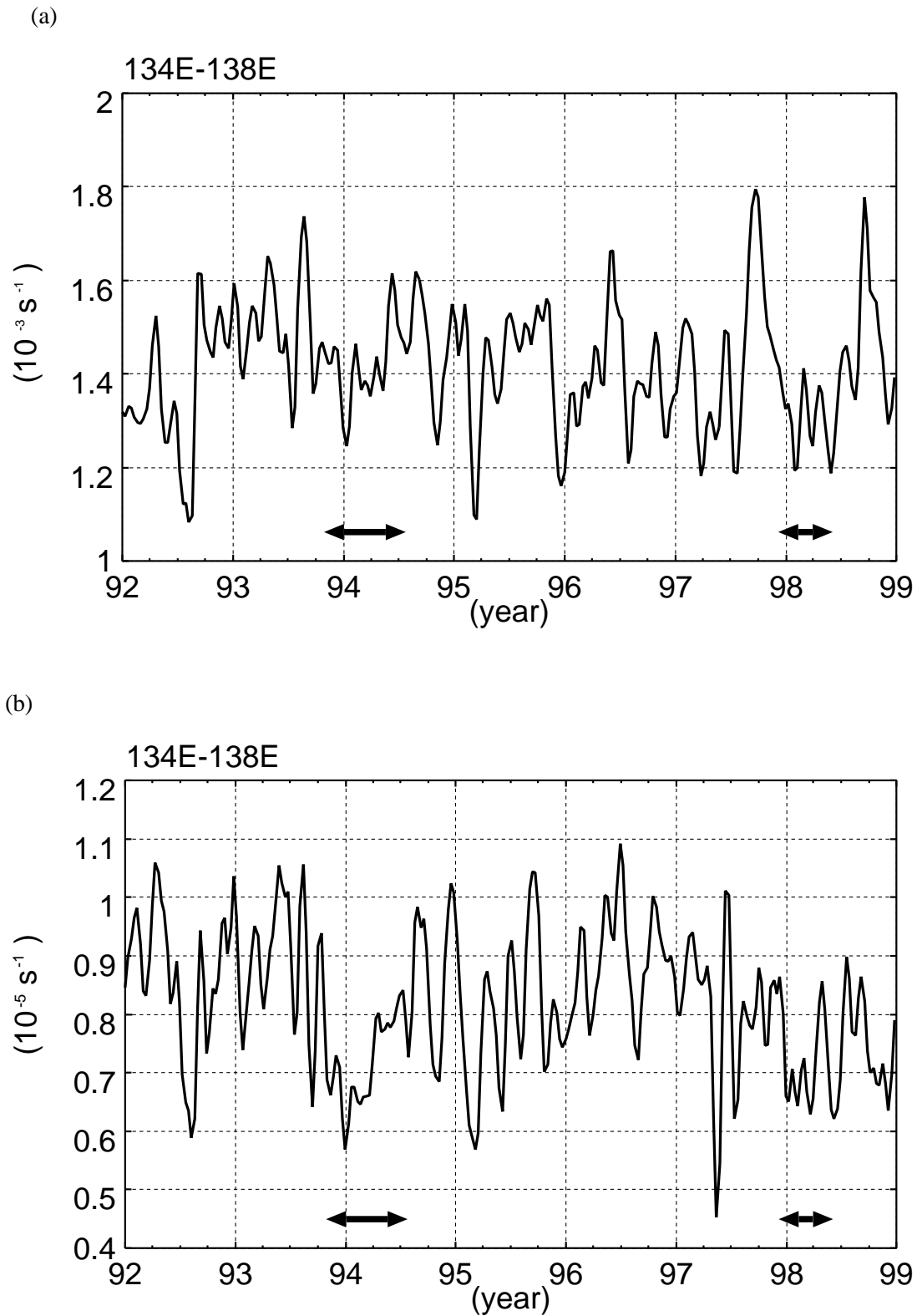


Figure 1.20 Time series of the RMS velocity shear of the Kuroshio main stream in 134°-138°E and in 100m to 1000m. The Kuroshio main stream is defined as the region in which mean velocity is larger than 0.4 m s^{-1} . Variations with time scale shorter than 30 days are removed. (a) Vertical shear. (b) Horizontal shear.

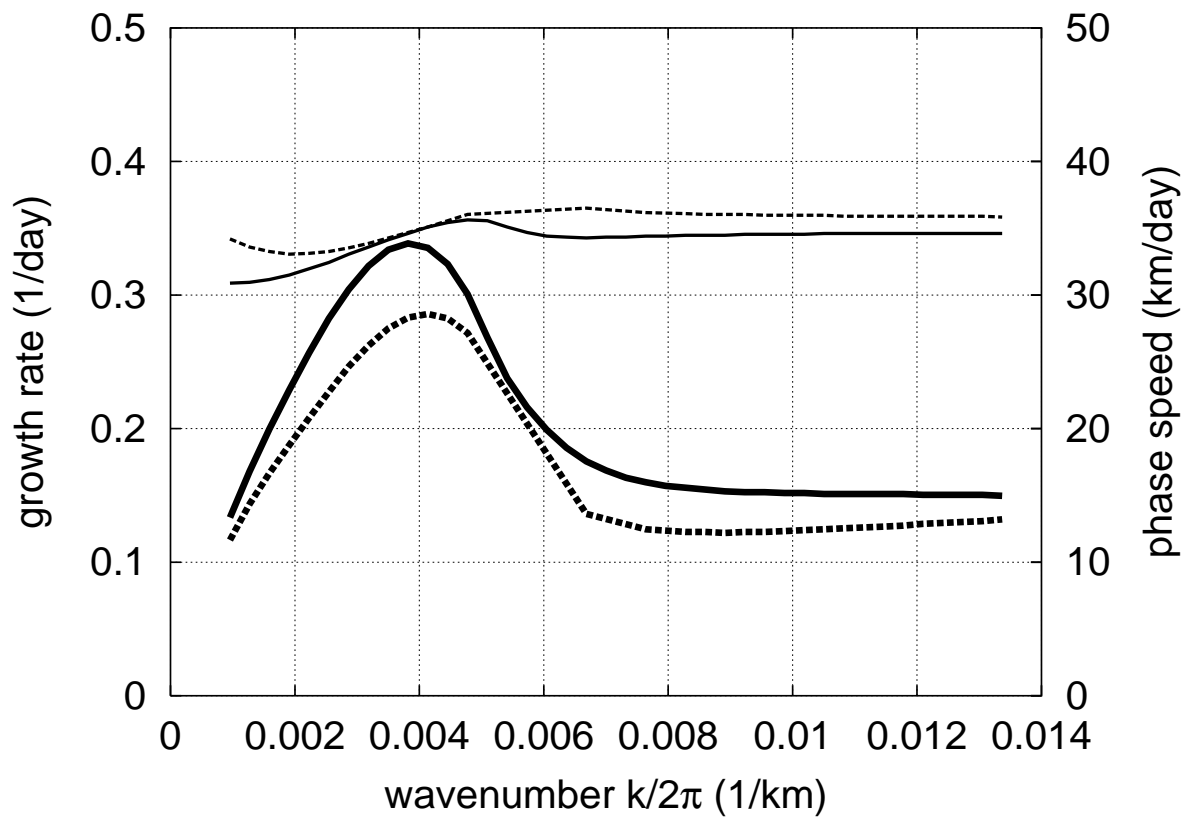


Figure 1.21 Growth rate and phase speed for the velocity profiles at 136°E on 12 October 1993 (solid line) and on 9 January 1998 (dashed line). Thick lines denote growth rate and thin lines denote phase speed.

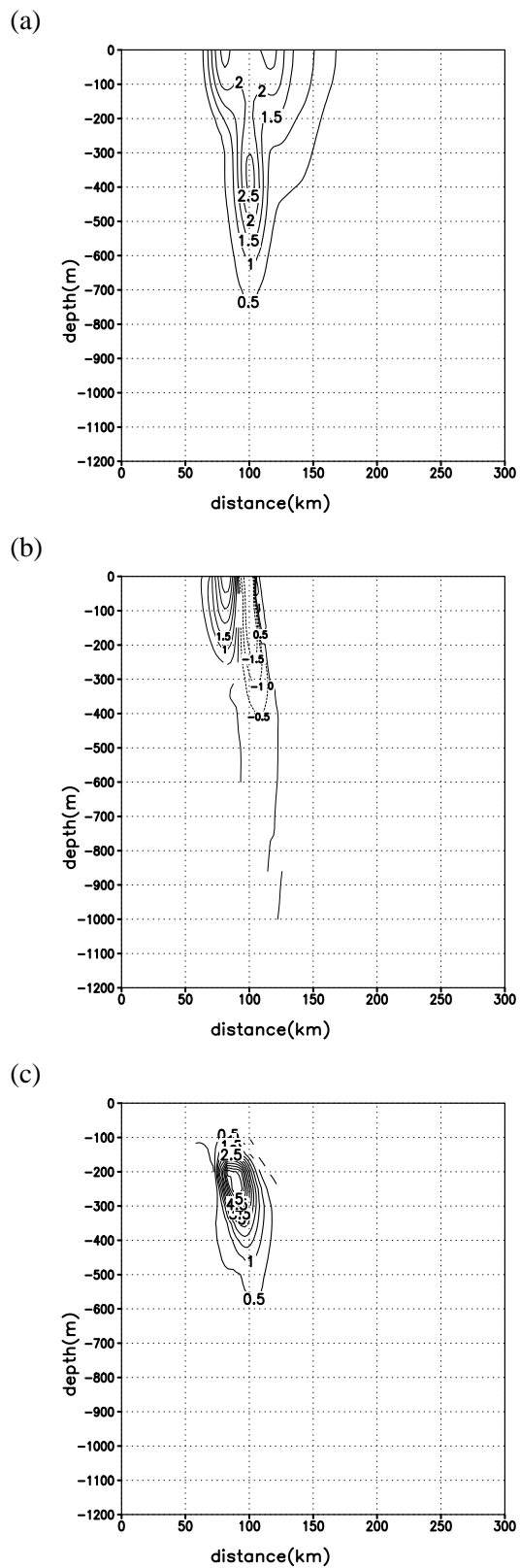


Figure 1.22 Depth-latitude sections at 136°E for (a) structure of the growing disturbances ($\bar{u}^2 + \bar{v}^2$), (b) barotropic conversion (c) baroclinic conversion.

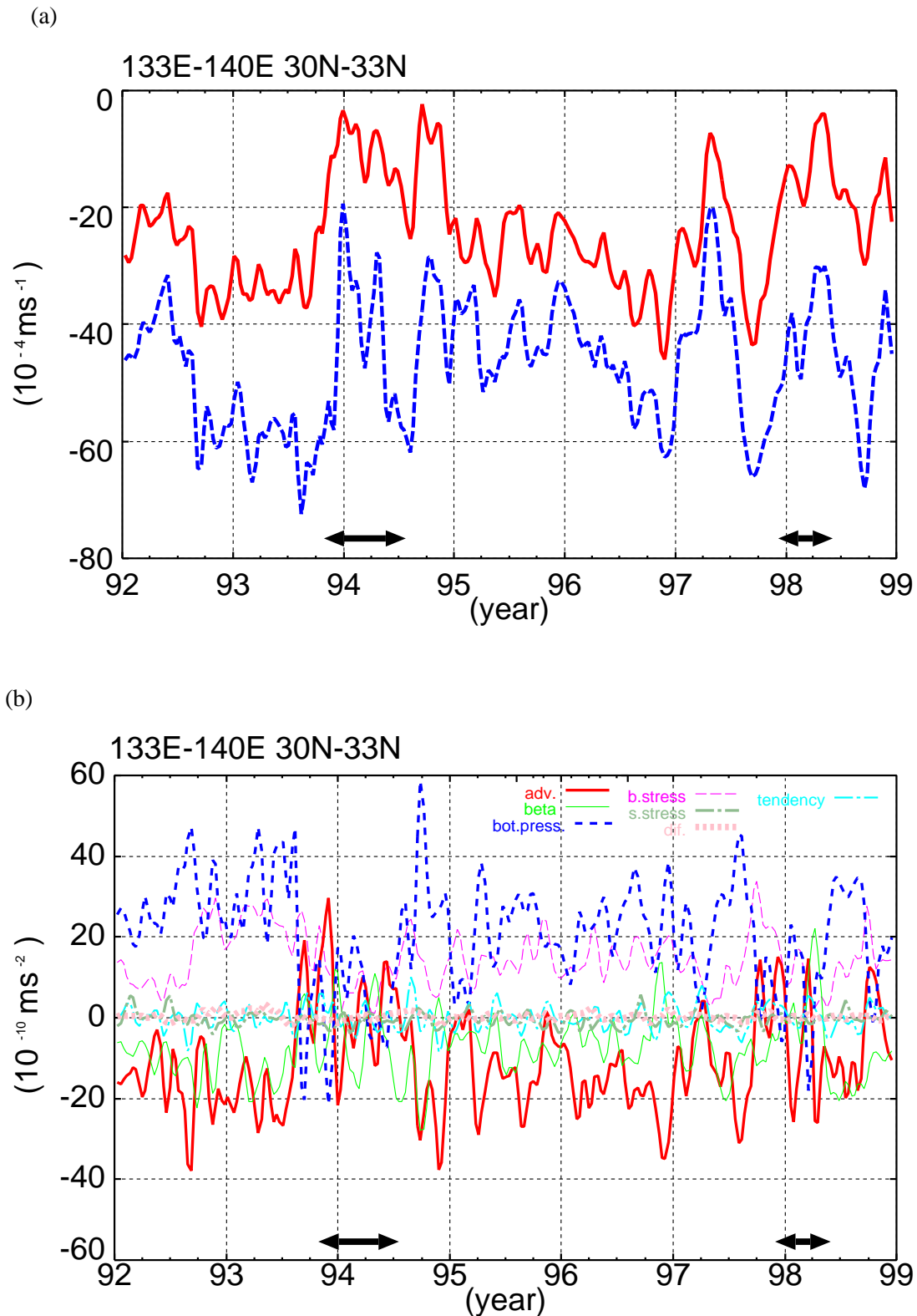


Figure 1.23 (a) Time series of mean vorticity of vertically integrated velocities in 30°-33°N, 133°-140°E (solid line). Dashed line denotes mean vorticity in the area excluding the Kuroshio meander. Variations with time scale shorter than 30 days are removed. (b) Time series of torque balance in 30°-33°N, 133°-140°E. Variations with time scale shorter than 30 days are removed.

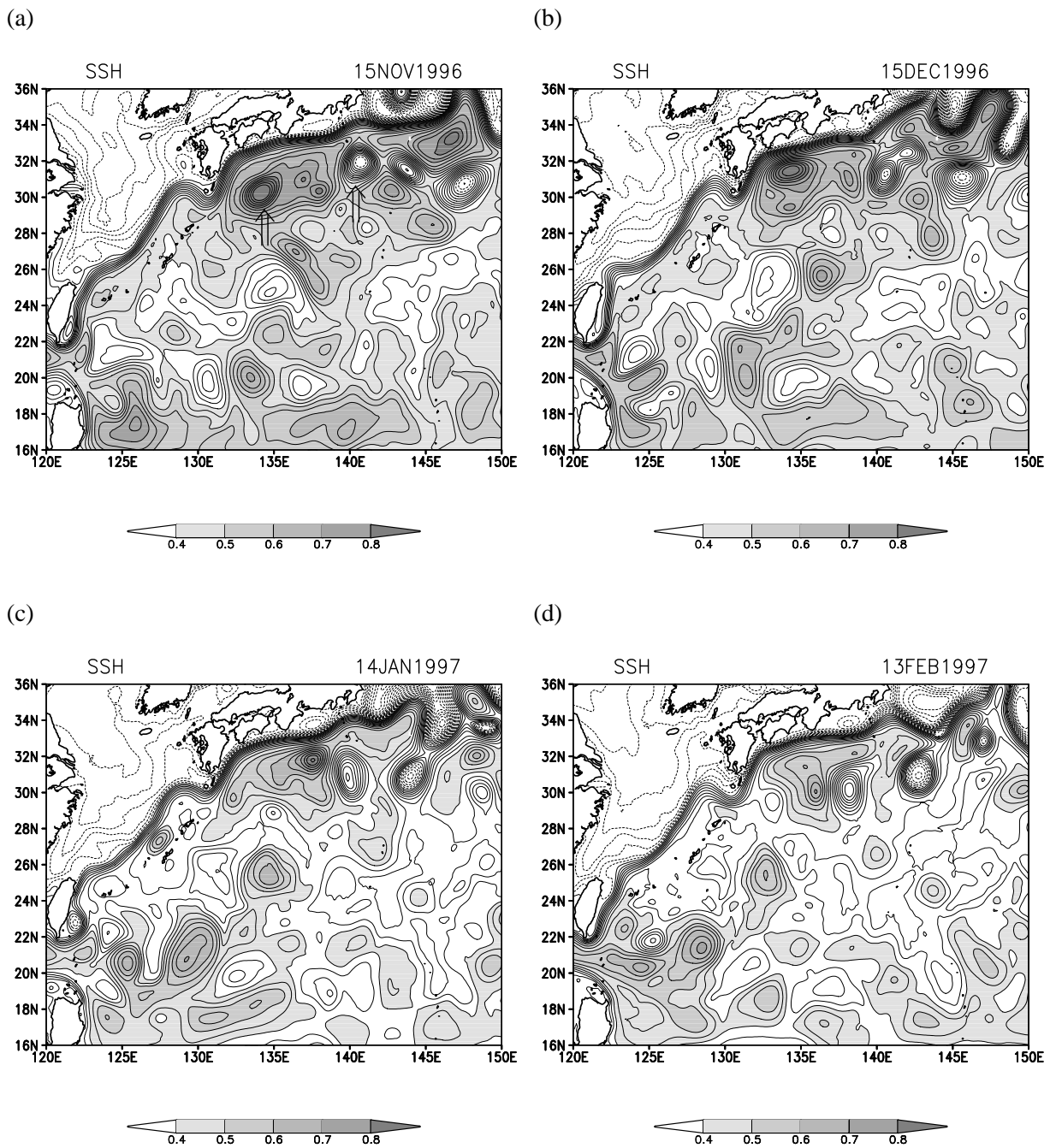


Figure 1.24 As in Fig.1.12 except for showing the interaction between the anticyclonic and cyclonic eddies. (indicated by arrows) (a) 15 November 1996. (b) 15 December 1996. (c) 14 January 1997. (d) 13 February 1997.

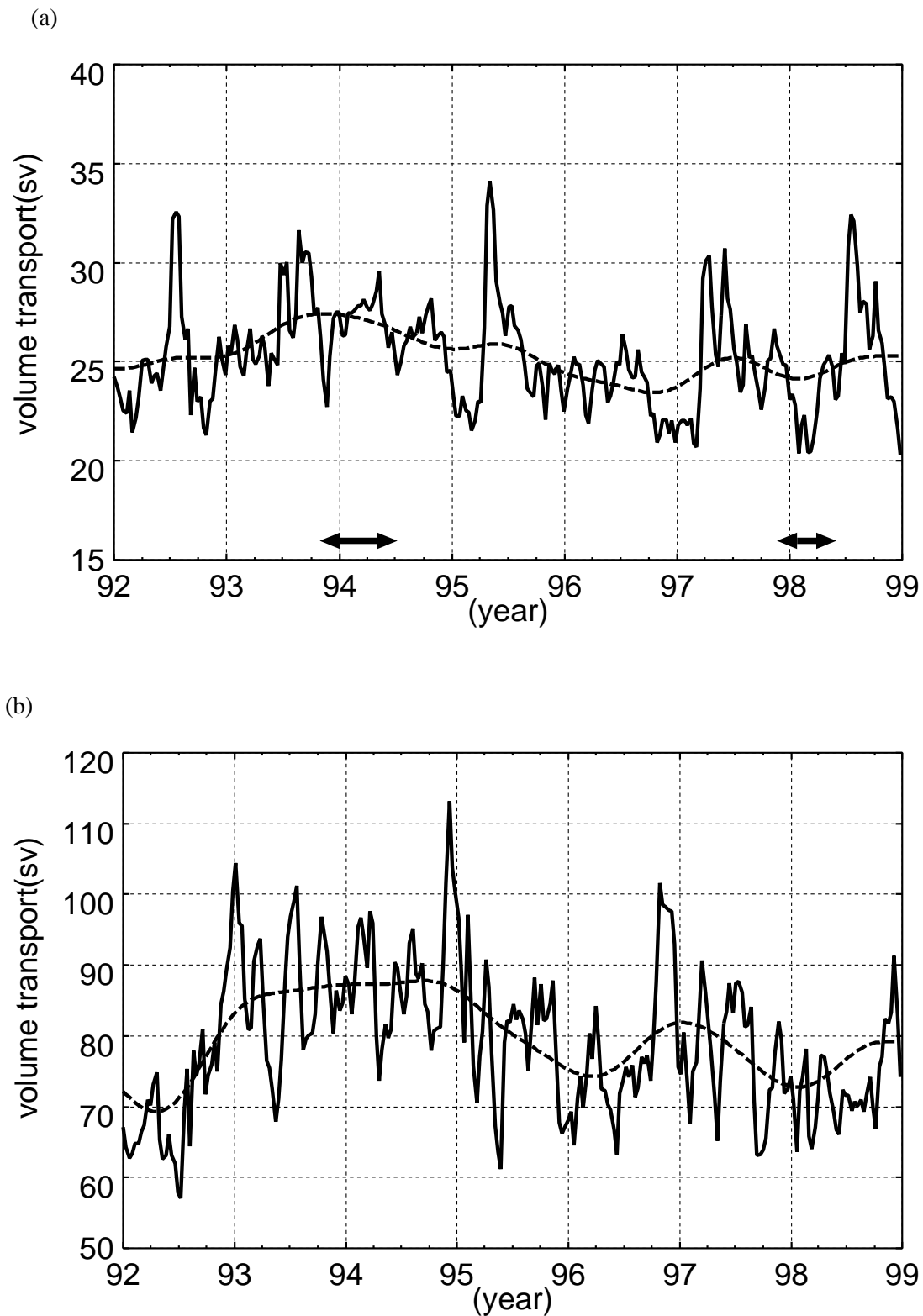


Figure 1.25 Time series of the model Kuroshio transport across (a) the PN line relative to 700m and (b) the ASUKA line upper 1000m from 1992 to 1998. Thin line denotes the filtered estimate (longer than 1 year) of the volume transports.

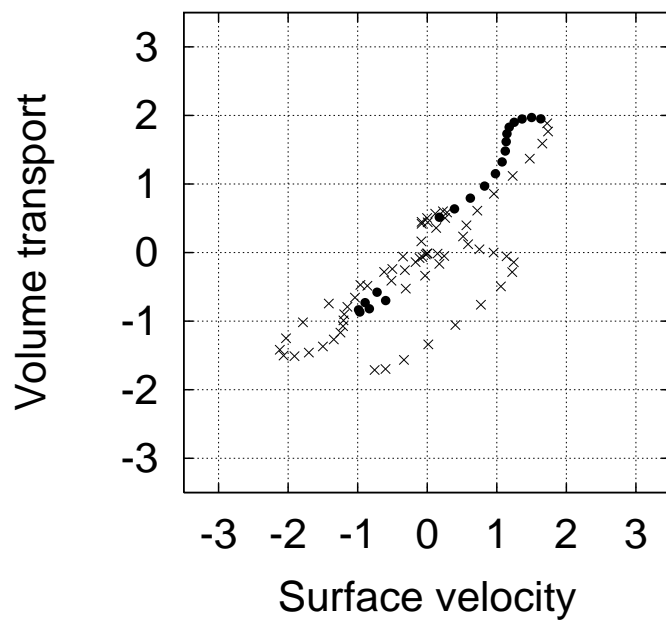


Figure 1.26 Relations between the surface velocity of the Kuroshio (in the Tokara Strait) and the volume transport (across the PN line). Closed circles correspond to the large-meander and crosses correspond to the non-large-meander. The unit is one standard deviation from the mean. The surface velocity in the Tokara Strait is estimated from the sea level difference between Naze and Nishinoomote (1 and 2 in Fig.1.1, respectively).

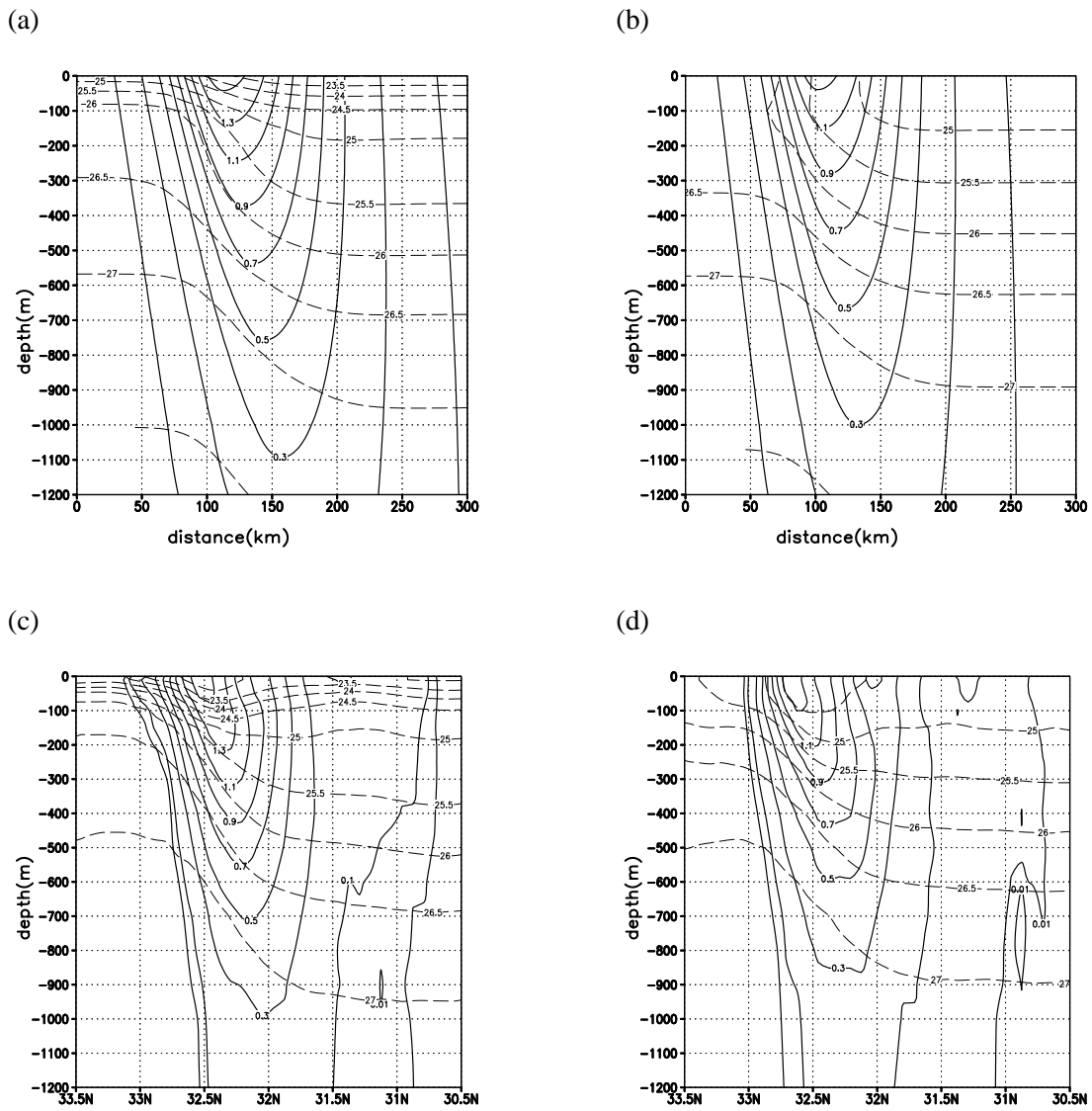


Figure 1A.1 The Kuroshio front at 136°E. Thick contour denotes velocity (m/s). Dashed contour denotes density (σ_θ). (a) Profile approximated by using formulae (A.1.7) on 12 October 1993. (b) As in (a) on 9 January 1998. (c) Snapshot of the OGCM simulation on 12 October 1993. (d) As in (c) on 9 January 1998.

Part II

Ensemble forecast of the Kuroshio meandering

2.1 Introduction

The transition of the Kuroshio path between the large-meander state and the non-large-meander one has been extensively investigated by both theoretical and observational studies. The theoretical studies (e.g., Masuda 1982) suggest that the Kuroshio can possess multiple equilibria under the same external conditions. Kawabe (1995) discussed the equilibrium states of the Kuroshio system and showed that the large meander appears when the upstream volume transport is relatively large.

As in the atmospheric blocking, we may classify the theoretical studies into two categories: nonlocal (e.g., White and McCreary 1976; Masuda 1982) and local approaches (Yamagata and Umatani 1989). The former adopts the lee-wave theory for Rossby wave and formulates the Kuroshio bimodality problem as a boundary value problem in which the phase speed C of Rossby wave satisfies suitable inlet and outlet conditions imposed at respective boundaries near the strait south of Kyushu and the one at the Izu-Ogasawara Ridge. In this case, the large-meander state exists when the upstream current U satisfies either subcritical ($U+C<0$) or critical ($U+C=0$) conditions. On the other hand, Yamagata and Umatani (1987; 1989) demonstrated that, for a supercritical condition ($U+C>0$), the observed large-meander can be interpreted as a manifestation of the geometrically trapped nonlinear solitary wave. Mitsudera and Grimshaw (1994) extended the theory into a baroclinic case and showed that the specified local topography can generate a stationary large-amplitude wave through baroclinic instability process satisfying a supercritical condition. The observational study of Kawabe (1995) supports the local approach at least for the meander formation (Mitsudera and Grimshaw 1994). Recent modeling studies using realistic topography suggest that even a local seamount south of Japan is important for the formation of the Kuroshio large-meander (Hurlburt et al. 1996; Endoh and Hibiya 2001; Part I).

In the framework of the above local approach, transitions between multiple equilibria

are governed by initial disturbances if the given state is within the appropriate dynamical regime (Yamagata and Umatani 1987; Mitsudera and Grimshaw 1994). In fact, this conjecture was tested numerically and the transitions between different states are successfully simulated in some modeling studies (e.g., Endoh and Hibiya 2001). The Kuroshio volume transport has been either large or intermediate since 1975, however, the stable large-meander has not occurred in the last decade (see Quick Bulletin of Ocean Conditions by the Japan Coast Guard; Qiu and Miao 2000). Therefore, if the real Kuroshio state falls in one of the multiple equilibrium states since 1975, it is interesting to investigate, based on hindcast experiments using a realistic ocean general circulation model (OGCM), how the Kuroshio path variation is sensitive to the initial disturbances.

Recent observational studies using the satellite altimeter and the *in-situ* Acoustic Doppler Current Profilers (ADCPs) showed that meso-scale eddies are very active south of Japan (Ebuchi and Hanawa 2000). Regional numerical studies (Mitsudera et al. 2001; Endoh and Hibiya 2001) employing the inflow-outflow boundary conditions also demonstrated that a meso-scale eddy triggers the Kuroshio large-meander or offshore non-large-meander. Ebuchi and Hanawa (2003), using the satellite altimetry data, reported that three offshore non-large-meanders in 1993, 1998, and 1999 were triggered by anticyclonic eddies. In Part I, we were successful in simulating the Kuroshio path variation induced by the eddy-Kuroshio interaction using a basin-wide eddy-resolving OGCM.

So far, a few studies have examined possibility of operational numerical predictions of the Kuroshio path south of Japan. Komori et al. (2003), using a reduced gravity model initialized by assimilating the TOPEX/POSEIDON altimetry data, estimated the predictability limit which falls within the range extending from 30 to 90 days and they further pointed out that the estimate of this kind would heavily depend on the model dynamics employed. Kamachi et al. (2004) conducted hindcast experiments of the Kuroshio path during from 1993 to 1999 using an eddy-permitting ($1/4^\circ$ grid) OGCM

with assimilated the TOPEX/POSEIDON data. The predictability limit of their forecast system is reported to be about 80 days. They suggest that the eddy-Kuroshio interaction is an important potential mediator causing the transition from the nearshore to offshore non-large-meander. However, they have not discussed the generation mechanism of the large-meander.

In addition to a single trajectory forecast experiment, Kamachi et al. (2004) performed an ensemble forecast with five ensemble members accompanying the transition from nearshore to offshore non-large-meander. Their ensemble mean forecast yielded slightly better forecasting skill than the unperturbed forecast. However, since their experiment was very preliminary, neither detailed features of the spread in their ensemble experiment nor sensitivity of the prediction on the imposed initial errors was discussed in their study.

No conventional method on ensemble generation has been established yet for multimodal dynamical systems such as the Kuroshio path south of Japan. For a simple dynamical system with multiple attractors, Miller and Ehret (2002) evaluated the performance of ensemble runs with several different methods of generation, however, the performance of such a complex dynamical system as the one under consideration remains to be investigated further. As the first step towards such studies, we utilize here an iterative ensemble generation process called “breeding method” (Toth and Kalnay 1993). The breeding method may well simulate the development of growing errors in the assimilation cycle.

In this part, we discuss the event in the year 1999 using an eddy-resolving OGCM with the TOPEX/POSEIDON altimetry data assimilated into the initial field. We conduct a hindcast experiment of the Kuroshio path for a period of 80 days after the last cycle of the assimilated initialization. To the best of our knowledge, the present work is the first comprehensive attempt to investigate the predictability of the Kuroshio meandering using the ensemble forecast approach. Since the eddy dynamics is an important factor in the

Kuroshio path variation as discussed in Part I, the present use of the eddy-resolving OGCM is vital and enables us to examine meaningful case-by-case variation in the model ensemble.

This part is organized as follows. In Section 2.2, a hindcast experiment of the event in 1999 as a single trajectory forecast is described. Section 2.3 covers the results of the ensemble forecast experiment, in particular, the characteristics relating to both the skill and spread in the ensemble run are argued. In Section 2.4, looking into the ensemble forecast of 80 days, we discuss the possible dynamical roles played by eddies in triggering the bifurcation of the bimodal Kuroshio paths. Section 2.5 is devoted to summary of this part.

2.2 Hindcast experiment of the Kuroshio meandering

2.2.1 Ocean model

The present ocean model is based on Princeton Ocean Model (POM) (Mellor 1998), one of the most popular community models in the world. A high-resolution regional model with spatial grid of 1/12 degree and 35 sigma levels is embedded in a low-resolution basin-wide model with a spatial grid of about 1/4 degree and 21 sigma levels. The inner model domain covers the northwest Pacific (12° - 56° N, 117° - 180° E) and its lateral boundary conditions are determined from the basin-wide model using the one-way nesting method (Guo et al. 2003). Details of the model configuration are described in Part I.

The model is driven by wind stresses, and heat and salt fluxes. Both wind stress and heat flux fields are calculated from the 6-hourly NCEP/NCAR reanalysis data (Kalnay et al. 1996) using the bulk formula (Rosati and Miyakoda 1989). Salinity at the ocean surface is restored to monthly mean climatology data (Levitus et al. 1994) with a time scale of 30 days. Simulation of the low-resolution model is started from a state of rest with the annual-mean temperature and salinity fields created from a 1/4 degree climatology data

(Boyer and Levitus 1997). The low-resolution model is spun up by the monthly mean surface forcing for 10 years. Then the model is further driven by 6-hourly surface forcing covering from 1st of January 1991 to 30th of November 1999. The high-resolution model is also forced from a state of rest with the climatological temperature and salinity fields but with 6-hourly surface forcing applied from 8th of August 1996 to 30th of November 1999.

2.2.2 Hindcast of the Kuroshio meandering in 1999

According to Quick Bulletin of Ocean Conditions published by the Japan Coast Guard (left panels of Fig.2.1), the real Kuroshio took an offshore non-large-meander path from November 1999 to June 2001. A hindcast experiment without initialization failed to reproduce this offshore non-large-meander episode. Therefore, TOPEX/POSEIDON sea surface height anomaly (SSHA) data in the period starting from 26th of July to 7th of September 1999 have been successively assimilated to the simulated fields in the high-resolution model with the time interval of 10 days.

For the indirect estimation of temperature and salinity fields, we adopt a practical approach similar to the optimal analysis equation proposed by Mellor and Ezer (1991). The analyzed estimate of the forecast variable T^f at depths from 50m to 2000m is calculated as follows:

$$T^a = T^f + P_{T\eta} F_{T\eta} (\Delta\eta^o - \Delta\eta^f), \quad (2.1)$$

where T^a and T^f are analyzed and forecast quantities; $P_{T\eta}$ is a weight of correction and $F_{T\eta}$ is a regression coefficient calculated statistically from the model results without assimilation; $\Delta\eta^o$ and $\Delta\eta^f$ denote the observed and the simulated SSHA, respectively. $\Delta\eta^f$ in (2.1) is calculated by subtracting the temporal mean from the SSH obtained through the one year model simulation in 1998. The observed along-track SSHA referencing to the Ohio University Mean Sea Surface, provided by the Colorado Center for Astrodynamic Research Real-Time Altimeter Data Group (Lillibridge et al. 1997), is

interpolated to the model grid with an interval of 10-days using an optimum interpolation method (Kuragano and Kamachi 1999). The latitudinal mean value of the SSHA corresponding to the large-scale, seasonal variation is subtracted from the SSHA to assimilate only meso-scale variation (Wakata, personal communication). The weight of correction $P_{T\eta}$ in (2.1) is calculated so that it minimizes the analyzed error $\langle (T^a - T^t)^2 \rangle$, where $\langle \cdot \rangle$ denotes an expected value and T^t represents a true state. $P_{T\eta}$ has the following form:

$$P_{T\eta} = \frac{E_s}{E_o + E_s + 1/C_{T\eta}^2 - 1}, \quad (2.2)$$

where $E_s = \langle (\Delta\eta^f - \Delta\eta^t)^2 \rangle / \langle \Delta\eta^{t^2} \rangle$ and $E_o = \langle (\Delta\eta^o - \Delta\eta^t)^2 \rangle / \langle \Delta\eta^{t^2} \rangle$ are the normalized simulation and observation error variances of SSHA, respectively. The quantity $C_{T\eta}$ is the correlation coefficient between the SSHA and the temperature/salinity. Derivation of equation (2.2) is described in Appendix 2. The normalized simulation error variance E_s is empirically determined to be 2.8 in the region south of Japan (27° - 38° N, 130° - 145° E) and 1.5 in the other. We conduct ensemble forecasts to reduce this uncertainty of error estimate. Interpolation error variance obtained from the optimum interpolation of along-track SSHA is specified as E_o . The normalizing factor $\langle \Delta\eta^{t^2} \rangle$ as the variance of true SSHA is to be substituted by the variance of observed SSHA, since there is no other way to give an approximate estimate of this quantity.

In order to achieve smooth assimilation, both temperature and salinity fields are nudged to the analyzed variables in (2.1) with a restoring time scale of 0.3 days during a tentatively set time span of 6 days in the middle of which observational data are provided and the analysis (2.1) is calculated using the temperature/salinity and SSHA fields forecasted at 3

days before the observation time. The grid data of SSHA created from 26th of July 1999 to 7th of September 1999 were assimilated into the original simulation. Then the time integration proceeded with constant surface forcing and lateral boundary condition evaluated at the last initialization time.

Right panels of Fig. 2.1 show evolution of the assimilated sea surface height after the last initialization. The anticyclonic eddy stays southeast of the Kyushu Island in the initial state. Then it propagates eastward toward the Kii Peninsula in October 1999 and generates the meander in November 1999 as observed (left panel of Fig.2.1). Thus, we see that the initialization with the aforementioned data assimilation processes leads to a successful prediction of the meander of the Kuroshio, though the predicted field on 26th of November 1999 underestimates the meander amplitude with its position shifted to the east compared with the observation.

To measure the forecasting skill quantitatively, we use both RMS error $e_1 = \sqrt{(\eta^f - \eta^r)^2}$ and anomaly correlation of sea surface height $c_1 = \frac{\overline{\Delta\eta^f \Delta\eta^r}}{\left(\overline{\Delta\eta^{f^2} \Delta\eta^{r^2}}\right)^{1/2}}$ for a reference sea surface height η^r , where $\bar{A} \equiv \frac{1}{N} \sum_{j=1}^N A_j$ (N denotes number of grid points in

the Kuroshio region, 28° -35° N, 130° -140° E); the RMS error is normalized by the value 0.19m which is the RMS variation in the Kuroshio region calculated from the one year model simulation in 1998. In the reference assimilation run, we utilize not only the TOPEX/POSEIDON but also the ERS-2 data to effectively approximate a true state. We call this additional assimilation run simply as the reference run. Figure 2.2a exhibits that a skill of the forecast (thick line with closed circles) is superior to those of non-assimilated simulation (long dashed line with crosses) and persistence (short dashed line with squares) during the meander period from 27th of October to 26th of November. The persistence

means the skill of the initial state for the whole forecast period. The forecasting skill exceeds the level of the modeled climatic variation more than 70 days after the last initialization. Another measure of skill, anomaly correlation, also shows the same feature as the RMS error (Fig. 2.2b).

2.3 Ensemble forecasts

Ensemble forecasts were conducted using 10 perturbed initial states generated by the breeding method (Toth and Kalnay 1993). First, on 26th of July 1999, two dimensional random perturbation $\Delta\eta_{ptb}$ with a horizontal correlation scale of 0.7 degree (Evensen 1994) is added to the analyzed value T^a_c of the assimilation run described in Section 2.2, in the region (27° - 38° N, 130° - 145° E) with upper 1000m depth ,

$$T^a_{ptb} = T^a_c + F_{\eta T} \Delta\eta_{ptb} \quad (2.3)$$

where $\Delta\eta_{ptb}$ is assumed to have zero mean and RMS magnitude of 0.05m. At every assimilation time during the period from 5th of August to 7th of September 1999, the difference of sea surface height anomaly (SSHA) between the perturbed run $\Delta\eta^f$ and the assimilation run $\Delta\eta_c$ is added to the adjusted value of the assimilation run as follows:

$$T^a_{ptb} = T^a_c + F_{\eta T} C_{0.05m} (\Delta\eta^f - \Delta\eta_c) \quad (2.4)$$

where $C_{0.05m}$ is a coefficient to make RMS value of $C_{0.05m} (\Delta\eta^f - \Delta\eta_c)$ equal to 0.05m. To simplify the rescaling of model states, we adjust only SSHA.

The theory of the ensemble forecast is based on the following important assumptions: 1) the model is perfect and forecast error growth is caused only by initial state error through internal dynamics of the model, 2) each individual integration in an ensemble is equally likely to represent the true state evolution, 3) an initial ensemble represents true analysis error distribution within sampling limits (Murphy 1988). The ensemble mean forecast is expected to have better forecasting skill statistically than an unperturbed forecast by smoothing out small-scale features, which are significantly influenced by the uncertainty of

the initial state. Theoretical estimate of RMS error of ensemble mean forecast for M ensemble members is $\langle e_M \rangle = \sqrt{(M+1)/2M} \langle e_1 \rangle$ where e_M and e_1 are RMS errors of an ensemble mean forecast and a single forecast, respectively; $\langle \rangle$ denotes an expected value (Murphy 1988). An additional assumption that variations in anomaly intensity are small yields an estimate of anomaly correlation of the form:

$$\langle c_M \rangle = \left\{ \frac{M}{1 + (M-1)\langle c_1 \rangle} \right\}^{1/2} \langle c_1 \rangle \quad \text{where } c_M \text{ and } c_1 \text{ are anomaly correlations of an}$$

ensemble mean forecast and a single forecast, respectively (Murphy 1988). These two theoretical relations indicate that ensemble mean forecast is better than in the skill than a single forecast on average. In the present study, we investigate the skill measured by both the RMS error and anomaly correlation averaged over the Kuroshio region (28° - 35° N, 130° - 140° E) in an ensemble forecast experiment, where the theoretical relations are not necessarily satisfied.

Figure 2.3a compares forecasting skills in ensemble mean measured by both the RMS error (solid line with closed circles) and anomaly correlation (dashed line with closed circles) with those of the unperturbed forecast. The RMS error of the ensemble mean forecast is comparable with that of the unperturbed forecast during the early period from September to October. During the late one from the end of October to a month ahead, however, the skill of the ensemble mean forecast shows some improvement; the RMS error almost agrees with a theoretical estimate (thin solid line). Anomaly correlation also indicates the improvement of the skill in the ensemble mean forecast during the late period, though the improvement is not so evident as that of the RMS error. The skill of the ensemble mean forecast does not agree well with the theoretical estimate because the model is not perfect; other error sources beside the initial state error would affect the forecasting skill. In addition, the initial states of the ensemble may be not well sampled over true analysis error distribution, which cannot be known easily

To demonstrate potential impact of the ensemble forecast, we perform ‘perfect’ model experiments in which one ensemble member is assumed to be a ‘true’ state and the other members ($M=9$) are regarded as perturbed members from it in our ensemble forecast. In this experiment, any run can be considered as a true state so that there are 10 ensemble runs in total. Difference between ‘true’ state run and ensemble forecast members is only initial state in the perfect model experiment. The initial ensemble, moreover, is assumed to represent true analysis error distribution within sampling limit. As shown in Fig.2.3b, the improvement of the averaged skill of our ensemble mean forecasts in the perfect model experiment is consistent with the theoretical estimate. In particular, anomaly correlation almost completely coincides with the theoretical estimate.

The spread of the ensemble provides useful information about predictability; the growth of spread indicates loss of forecasting skill. Here we adopt the RMS difference of individual ensemble members from the ensemble mean as a measure of the ensemble spread. Figure 2.4 indicates that the spread gradually increases with reduction of the forecast skill shown in Fig.2.3. Theoretical relation between the spread and the RMS error of a single forecast is given by $\langle s_M \rangle = \sqrt{(M-1)/2M} \langle e_1 \rangle$ under the theoretical assumptions. Since the relation of RMS error is given by $\langle e_M \rangle = \sqrt{(M+1)/2M} \langle e_1 \rangle$, we

have the relation: $\langle s_M \rangle \sqrt{M+1} / \langle e_M \rangle \sqrt{M-1} = 1$ (e.g., Takano 2002). Figure 2.5 compares

the time sequences of $s_M \sqrt{M+1} / e_M \sqrt{M-1}$ calculated from RMS errors and difference

respectively given in Figs. 2.3 and 2.4 for two cases where the RMS errors measured by comparing the unperturbed forecast with the reference run and those evaluated in the perfect model experiment. The perfect model experiment (solid curve with closed circles) exhibits that the size of the ensemble spread is consistent with the theoretical estimate. The performance of the ensemble forecast, of course, depends on the validity of the

assumptions. The real experiment (dashed curve with closed squares), however, clearly shows temporal variations; the value less than one in the early period becomes larger in October and exceeds one early in November. This increasing tendency is related to the bifurcation of the Kuroshio path, as is discussed in the next paragraph.

Fig.2.6 shows that the predicted Kuroshio meander defined as the ensemble mean of the 80-day forecast (thick curve) has larger amplitude in the region west of 140° E than the unperturbed forecast (dashed curve), which might be consistent with both Quick Bulletin of Ocean Conditions (lowest left panel of Fig. 2.1) and the reference run (Dot-dashed curve). However, since the Kuroshio path variation south of Japan has the multi-modal structure (e.g., Kawabe 1995), we must be careful in interpreting the ensemble mean forecast. Figure 2.6 indicates that the 80-day forecast ensemble members (thin curves) of the Kuroshio path south of Japan are classified into three patterns: weak meander (two members), weak meander east of the Izu Islands (three members), and strong meander (five members). The ensemble mean forecast of the present case seems to be a mixture of the multi-modal states. Exact skill evaluation of the ensemble mean forecast of the Kuroshio path variation needs more experiments for more various situations. In the present study, attention is focused on the variation of the Kuroshio path generated by the ensemble forecast.

The resulting Kuroshio paths shown in Fig.2.6 are characterized using an index calculated from sea surface variables at 32.5° N, 138° E. Figure 2.7a shows the time evolution of such an index in the ensemble. The index exhibits clear difference in the Kuroshio meander amplitude; low (high) level indices correspond to strong (weak) meander. The unperturbed forecast reproduces a weak meander east of the Izu Islands. The bifurcation of the Kuroshio path contributes to rapid increase of the ensemble spread in November as shown in Fig. 2.4.

It is well known that the change of the Kuroshio path is associated with sea level

changes along the southern coast of Japan (Kawabe 1995). According to the tide gauge data, the deviation from long-time mean of the sea level difference between Kushimoto and Uragami (see Fig.2.6 for locations) during the large-meander state is negative (about -10 mm) and less susceptible to change. As shown in Fig.2.7b, although all ensemble members predict reduction of the sea level difference between Kushimoto and Uragami, three members corresponding to the weak meander east of the Izu Islands show some rise in the sea level difference in November. The sea level at Hachijojima (see Fig.2.6 for location) is used as another path index of the Kuroshio axis which characterizes two non-large-meander states: the offshore non-large-meander (low level) and the nearshore non-large-meander (high level). The typical large-meander state is also characterized by high sea level at Hachijojima. The sea levels at Hachijojima in the ensemble members bifurcate into low and high states in November 1999 (Fig.2.7c); the low sea level appears in the three members corresponding to the weak meander east of the Izu Islands. In short, the Kuroshio path indices obtained from the members of the strong meander found in Fig.2.7a have more similar features to the large-meander than those obtained from the members of weak meander, which correspond to the nearshore or offshore non-large-meander.

In the next section, we will discuss the predictability of the Kuroshio meandering south of Japan from the viewpoint of eddy dynamics triggering and leading to the remarkable difference found in the 80 days ensemble forecast.

2.4 Predictability of the Kuroshio meandering

We plot the relation between the intensity of the initial trigger eddy and resulting meander amplitude of the ensemble forecasts in Fig. 2.8. Although the 50 days ensemble forecasts do not bifurcate into two branches yet (Fig.2.8a), striking path bimodality manifests itself in the 80 days ensemble forecasts. Therefore, the path state within the 50

days is more predictable. Figure 2.8b indicates that strong anticyclonic eddies may basically induce the large-meander. We note that one member stays at a weak meander state. In the latter case, the initial anticyclone is distorted and eventually splits into two weak anticyclones in September 1999. Then the weak anticyclone causes the weak meandering in November 1999. Note that the bifurcation of the meander types has no dependence on the upstream volume transport of two kinds: the Kuroshio main stream in the East China Sea and the Ryukyu current east of the Nansei Islands. For ensemble members, the volume transport of the Kuroshio main stream measured across the PN-line in the East China Sea ranges from 29 to 33Sv.

The previous studies (Hurlburt et al. 1996; Endoh and Hibiya 2001; Part I) have suggested that baroclinic energy conversion is related to the deep anticyclonic circulation associated with the Kuroshio meander. Figure 2.9 shows time evolution of the kinetic energy at the depth of 4000m averaged in the area of 31° - 33° N, 135° - 138° E. The large kinetic energy associated with the deep anticyclonic circulation is certainly found in ensemble members producing the large-meander (solid lines) in the 80-day forecast on 26th of November 1999. However, the deep anticyclonic circulation is not yet excited in the 50-day forecasts on 27th of October 1999. This difference is consistent with the characteristics of the meander growth shown in Fig. 2.8. We note that no difference is found in the kinetic energy of initial ensemble members.

Figure 2.10 compares evolution of the anticyclonic eddy activities depicted at sea surface height (upper 0.9m) and deep flow field in three different paths: the nearshore non-large-meander (nNLM), offshore non-large-meander (oNLM), and large-meander (LM). We can recognize clear intensity difference of the anticyclonic eddy southeast of Kyushu in the initial states. As the Kuroshio meander grows in November, both the upper and lower layer anticyclones in the LM case are significantly intensified compared with the NLM cases. As shown in Fig.2.11, time evolution of the kinetic energy of the anticyclonic

eddy at both 200m and 4000m depths demonstrate the distinctive concurrent evolution of the upper and lower layer circulations in the ensemble members corresponding to the large-meander. Figure 2.11 also exhibits that intensity of the initial anticyclonic eddy basically determines that of subsequent evolution of the eddy.

To specify a time scale of the trigger eddy, we introduce three non-dimensional parameters governing the geostrophic dynamics on a beta plane: the beta parameter ($\hat{\beta} = \beta L / f$), stratification parameter ($\hat{s} = (R_d / L)^2$), and Rossby number ($\hat{\epsilon} = \hat{s}(\Delta H_1 / H_1)$) (Pedlosky 1987). The notations employed here are as follows: f is the Coriolis parameter ($7.3 \times 10^{-5} 1/s$), β the meridional gradient of f ($2.0 \times 10^{-11} 1/sm$), L the horizontal length scale (120km), R_d the internal deformation radius (40km at 30° N according to Emery et al. (1984)), H_1 depth of the thermocline (550m), and ΔH_1 is variation of the thermocline (50m to 80m for depth of 26.5 sigma-t). For the anticyclonic eddies in the ensemble initial states, we have $\hat{\beta} = 0.033$, $\hat{s} = 0.11$, and $\hat{\epsilon} = 0.010 - 0.016$. This suggests that they fall into the subset of the planetary geostrophic regime (PG2) in Williams and Yamagata (1984) or the frontal geostrophic regime in Cushman-Roisin (1986)). If we introduce a two-layer model, the inverse time scale of the frontal geostrophic eddy is given by $\omega = (H_1 / H) \hat{\epsilon} = (P_2 / P_1) \hat{\epsilon}$ (Cushman-Roisin et al. 1992), where H is the total depth of 4000m; P_1, P_2 are pressure scales of the upper and lower layers, respectively. For the eddies in the ensemble experiments, this time scale ranges from 72 days to 115 days. It is determined by the slow lower-layer velocity field related to pressure P_2 there. The time scale might be consistent with the limit of the predictability in the present study, i.e., 50-80 days. The OGCM simulation suggests that the time scale of the trigger eddy is longer than time scale due to advection by the Kuroshio main stream, i.e., 10 days. The time scale of the predictability is related to behavior of the eddy itself rather than the simple advection of the eddy by the Kuroshio.

2.5 Summary

We have demonstrated that our forecast with a state-of-the-art OGCM initialized on 7th of September 1999 by assimilating sea surface height data successfully predicts the meandering of the Kuroshio south of Japan as observed in November 1999. The experiment yields a forecasting skill for 70 days in the sense that the RMS error of sea surface height anomaly does not exceed the magnitude of the model climatic variation and those obtained from the non-assimilated simulation and persistence. The time scale agrees with that evaluated by the previous studies (Komori et al. 2003; Kamachi et al. 2004). While we obtained the hopeful results from the ensemble forecast experiment, further extensive studies of this kind are needed to assess the effects of the ensemble forecast on the forecast skill. In the present study, we focused our attention on the transitions from the nearshore non-large-meander to the large or offshore non-large-meander.

The meanders occurred in the ensemble members for the 80-day forecast are classified into two categories: the large-meander and the non-large-meander. The bifurcation occurs more than 50 days after the initialization. In the present case, the ensemble mean of the 80-day forecast seems to be a mixture of the multi-modal states, which is similar to climatological mean state of the Kuroshio path. Skill improvement using the ensemble mean forecast would be validated by conducting many forecast experiments for various situations of the Kuroshio path transition.

A novel feature we found in our experiments presented here is a fact that the intensity of an initial anticyclonic eddy plays a key role for the subsequent development of the Kuroshio meander classified into two categories, i.e., a strong anticyclone induces the large-meander. Figure 2.8b suggests that a critical level of the intensity exists. 0.05m of the analysis error of sea surface height anomaly, which corresponds to 50m of the depth variation of 26.5 Sigma-t, averaged in the upstream region may be enough for the bifurcation of the Kuroshio path forecasts in the ensemble. Interpolation error of sea

surface height anomaly used in the present study almost always exceeds 0.05m over the whole Kuroshio region. Thus we can not ignore the uncertainty in forecast of the Kuroshio meandering associated with the multi-modality, though analysis error might be theoretically expected to become smaller than the interpolation error.

The present study suggests the importance of the local eddy dynamics in the Kuroshio recirculation region to the bifurcation of the Kuroshio path. However, detailed mechanism is still unclear. Further intensive studies are needed on interactions between the Kuroshio and meso-scale eddies.

The ensemble forecast is a promising way to study predictability of the Kuroshio path. Further development of the ensemble forecast method (e.g., Yamane and Yoden 2001) would lead us to deeper understanding of the Kuroshio path variation.

Appendix.2: Weight of correction for the analysis equation

Following Mellor and Ezer (1991), we derive the equation (2.2). The errors of the observed and forecast sea surface height anomaly (SSHA) are defined according to

$$\Delta\eta^o - \Delta\eta^i = \delta\eta^o, \quad \Delta\eta^f - \Delta\eta^i = \delta\eta^f. \quad (2.A.1)$$

On the other hand, the errors arising from our assimilation adjustment (analysis) described in Eq. (2.1) are defined according to

$$T^a - T^i = \delta T^f + P_{T\eta} \left(F_{T\eta} (\Delta\eta^o - \Delta\eta^f) + \delta T^c \right), \quad (2.A.2)$$

where δT^c is an error associated with the incomplete correlation between SSH and temperature/salinity, and $\delta T^f = T^f - T^i$. Using Eqs. (2.A.1) and (2.A.2), the assimilation adjustment error variance $\langle (T^a - T^i)^2 \rangle$ is expressed as follows,

$$\langle (T^a - T^i)^2 \rangle = \langle \delta T^{f^2} \rangle + P_{T\eta}^2 \left(F_{T\eta}^2 \left(\langle \delta\eta^{f^2} \rangle + \langle \delta\eta^{o^2} \rangle \right) + \langle \delta T^{c^2} \rangle \right) - 2P_{T\eta} F_{T\eta} \langle \delta\eta^f \delta T^f \rangle. \quad (2.A.3)$$

In the derivation of Eq. (2.A.3), the forecast, observation and correlation errors are assumed to be uncorrelated.

To determine the weight $P_{T\eta}$, we minimize the adjustment error given in Eq. (2.A.3) by

looking into the condition: $\frac{\partial \langle (T^a - T^i)^2 \rangle}{\partial P_{T\eta}} = 0$, which leads to

$$P_{T\eta} = \frac{F_{T\eta} \langle \delta\eta^f \delta T^f \rangle}{F_{T\eta}^2 \left(\langle \delta\eta^{f^2} \rangle + \langle \delta\eta^{o^2} \rangle \right) + \langle \delta T^{c^2} \rangle}. \quad (2.A.4)$$

Using further assumption of the form

$$\langle \delta\eta^f \delta T^f \rangle = F_{T\eta} \langle \delta\eta^{f^2} \rangle \quad (2.A.5)$$

and the derivation of the correlation error (Mellor and Ezer 1991)

$$\langle \delta \Gamma^{c^2} \rangle = F_{T\eta}^2 \langle \Delta \eta^{t^2} \rangle \left(\frac{1}{C_{T\eta}^2} - 1 \right), \quad (2.A.6)$$

we can write,

$$P_{T\eta} = \frac{\langle \delta \eta^{f^2} \rangle}{\langle \delta \eta^{f^2} \rangle + \langle \delta \eta^{o^2} \rangle + \langle \Delta \eta^{t^2} \rangle \left(\frac{1}{C_{T\eta}^2} - 1 \right)} \quad (2.A.7)$$

where $\langle \Delta \eta^{t^2} \rangle$ is variance of true SSHA. Normalization of the error variances in equation

(2.A.7) gives equation (2.2).

Figures

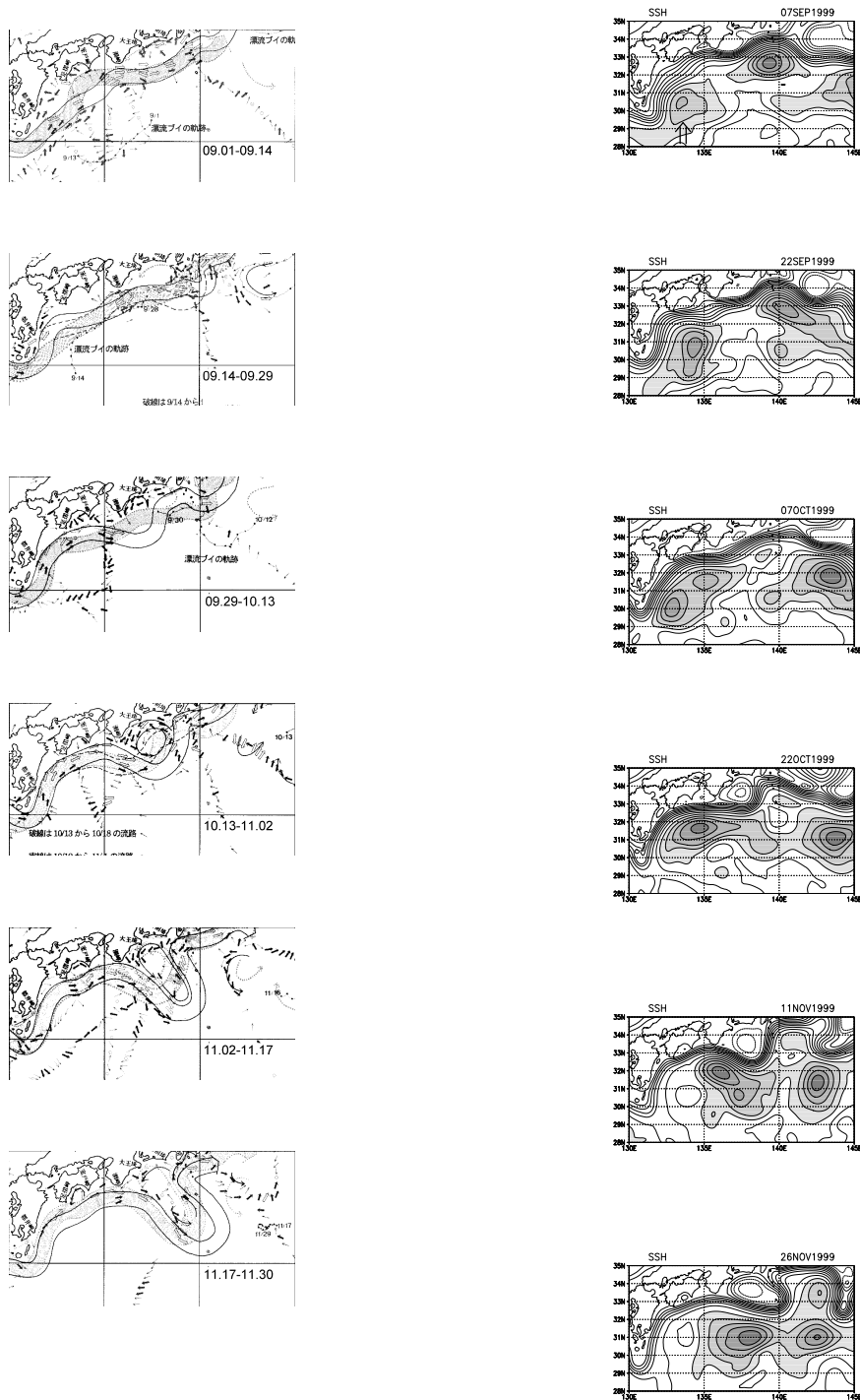
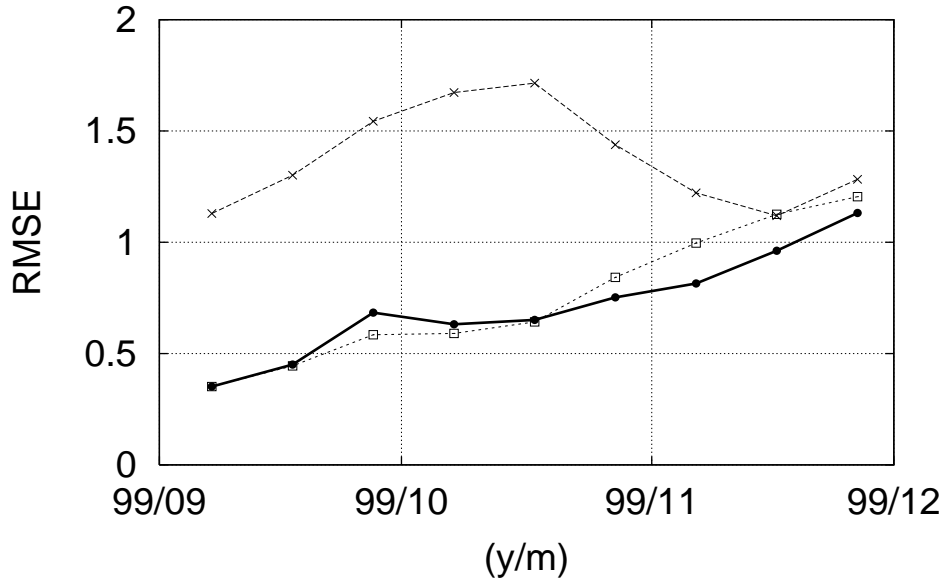


Figure 2.1 Left panels: bi-weekly mean observed Kuroshio path during the period from September 1999 to November 1999, reported in the Quick Bulletin Ocean Conditions provided by Hydrographic and Oceanographic Department, Japan Coast Guard. The grey path corresponds to the last and the white path to the current path. Right panels: the model sea surface height in 5-day mean of the unperturbed forecast. Contour interval of sea surface height is 0.1m.

(a)



(b)

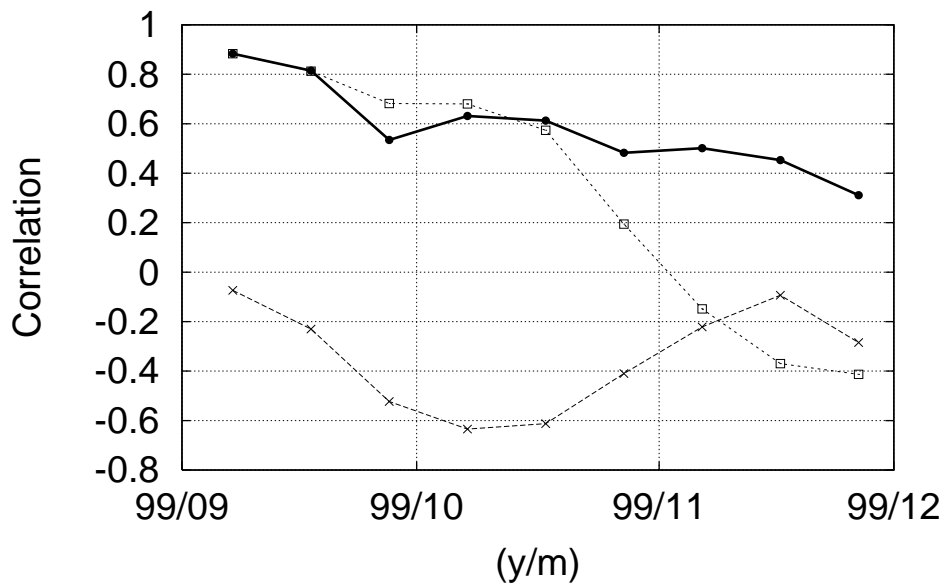
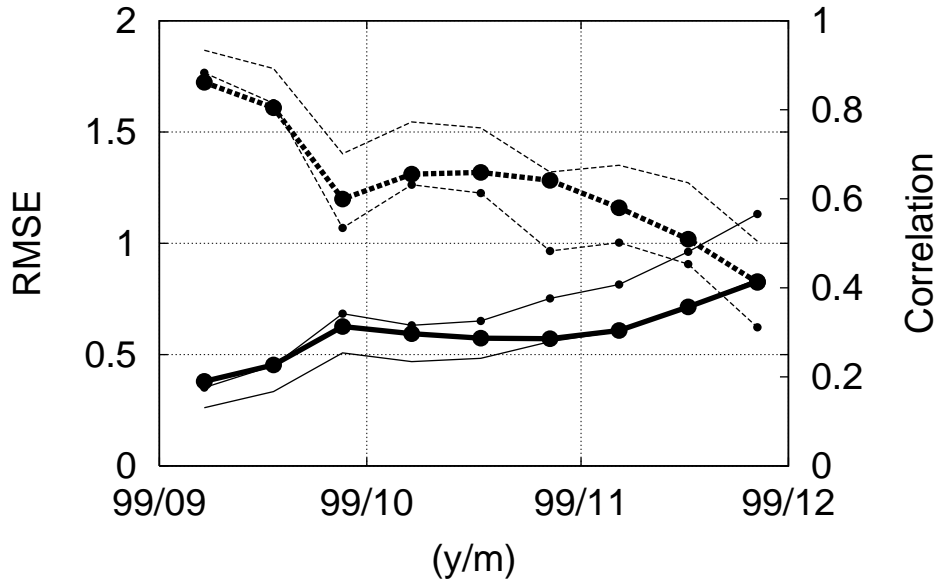


Figure 2.2 (a) Evolution of RMS errors of sea surface height anomaly for the reference run over the Kuroshio region, 28° - 35° N, 130° - 140° E. The RMS error is normalized by RMS variability of the simulation in the same region (0.19 m). Thick line with closed circles corresponds to the unperturbed forecast. Long dashed line with crosses corresponds to the non-assimilated simulation run. Short dashed line with squares corresponds to the persistence of an initial state. (b) As in Fig.2.2a except for anomaly correlation.

(a)



(b)

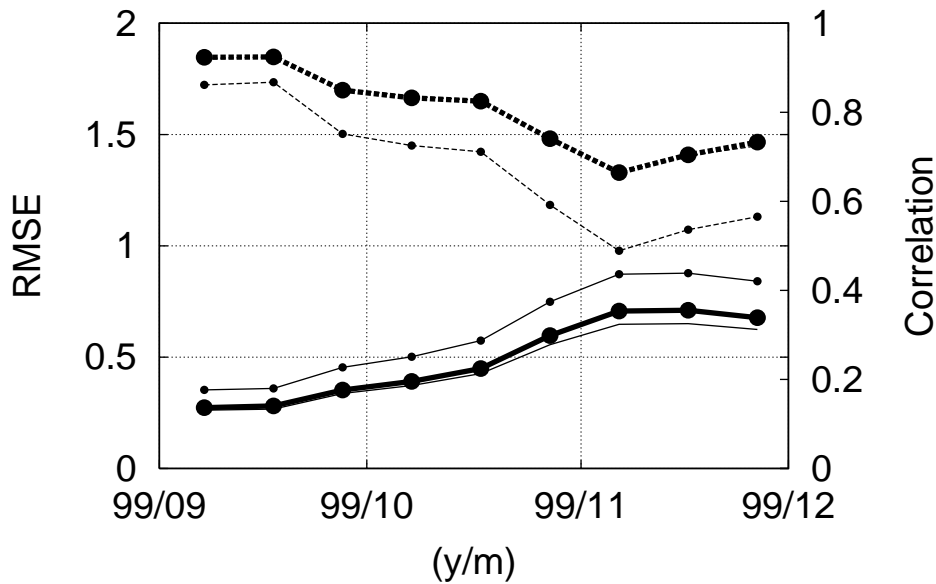


Figure 2.3 (a) Evolution of RMS errors of sea surface height anomaly normalized by RMS variability of the simulation (0.19 m) for the reference run over the Kuroshio region, 28° - 35° N, 130° - 140° E (solid lines with closed circles) and anomaly correlations (dashed lines with closed circles). Thick lines with closed circles denote the ensemble mean and thin lines with closed circles denote the unperturbed forecast. Thin solid and dashed lines denote theoretical skill, and, respectively ($M=10$). (b) As in Fig.2.3a except for a perfect model experiment. Thick lines denote averaged ensemble mean and thin

lines denote averaged skill of individual forecast. Theoretical curve for the anomaly correlation (dashed line) coincides with the curve of the ensemble mean (thick line with closed circles).

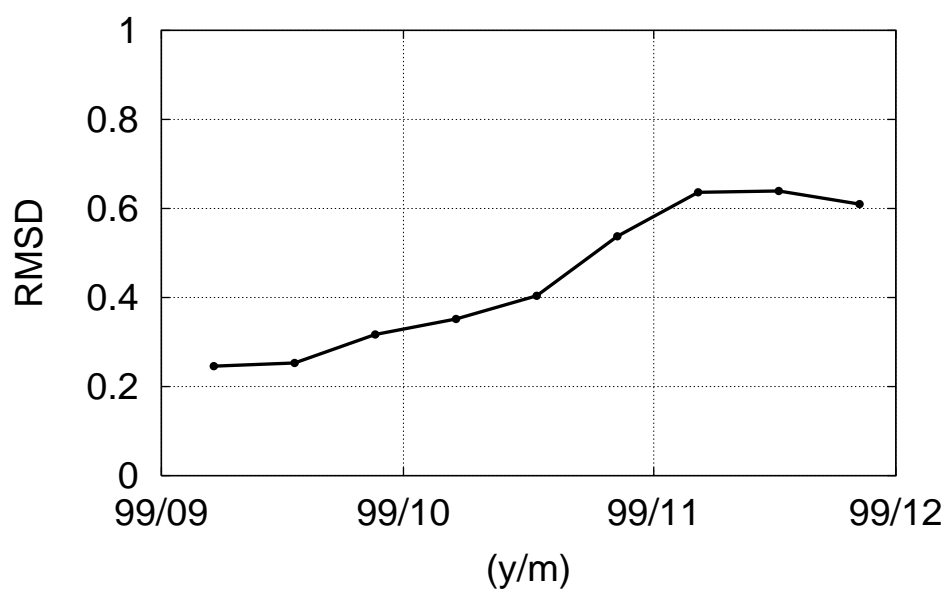


Figure 2.4 Evolution of ensemble spread, S_M , measured by RMS difference normalized by RMS variability of the simulation (0.19 m) for the reference run over the Kuroshio region, 28°-35°N, 130°-140°E.

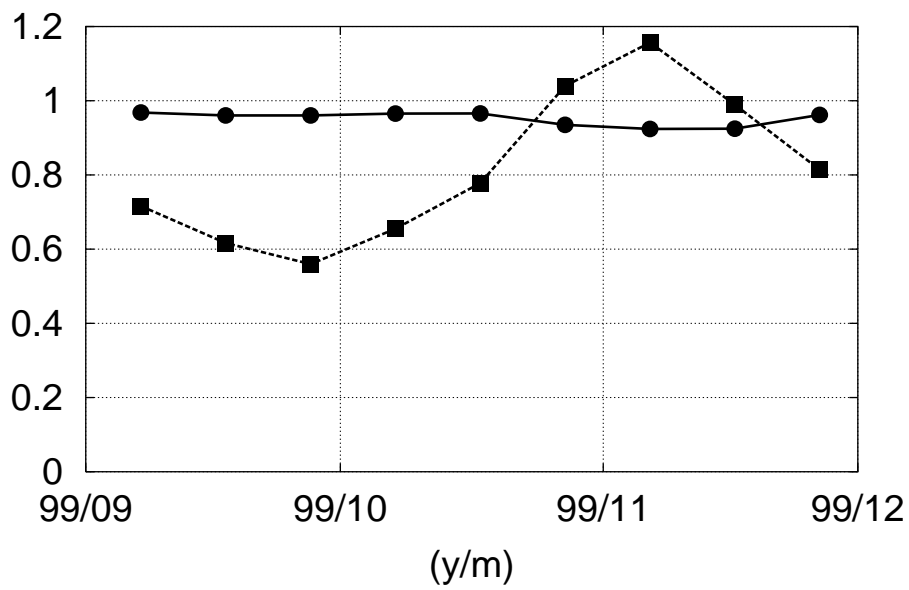


Figure 2.5 Evolution of $(S_M\sqrt{M+1})/(e_M\sqrt{M-1})$ ($M = 10$) in the Kuroshio region, 28° - 35° N, 130° - 140° E. Solid line with closed circles denotes a perfect model experiment. Dashed line with closed squares denotes an ensemble forecast reference to the reference run.

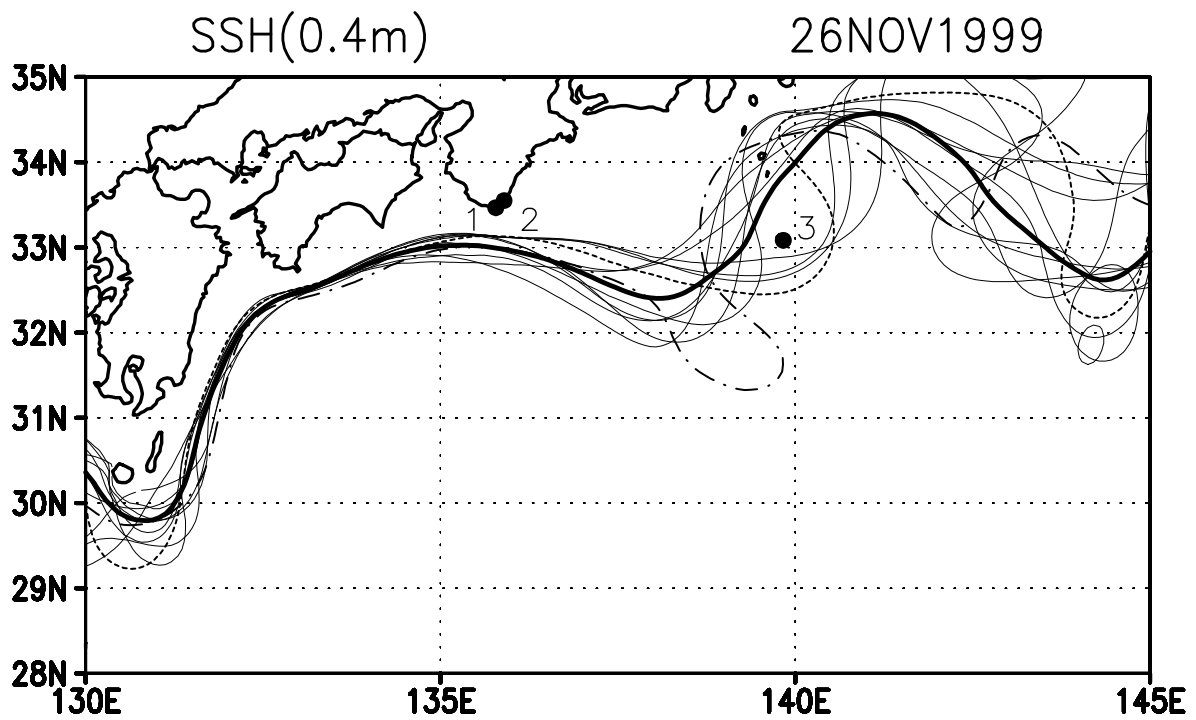


Figure 2.6 'Spaghetti' diagram of the Kuroshio path on 26 November 1999. The Kuroshio path is defined as a curve on which the value of sea surface height equals 0.4m. Thick curve denotes ensemble mean. Thin curves correspond to individual ensemble members. Dashed curve denotes the unperturbed forecast. Dot dashed line denotes the reference run. The numbers denote the tide stations; 1: Kushimoto, 2: Uragami, 3: Hachiojima.

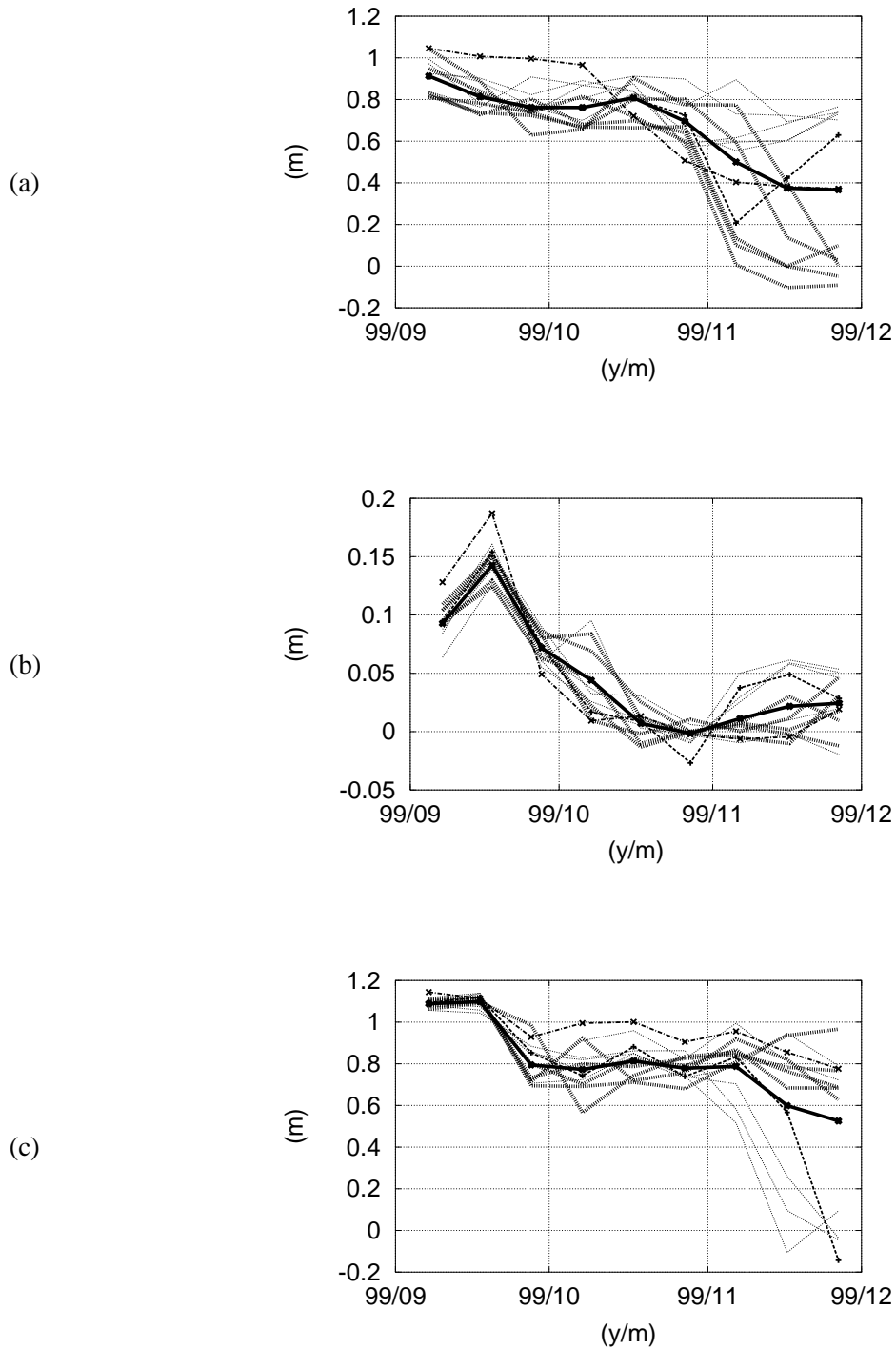


Figure 2.7 (a) Evolution of sea level at 32.5°N, 138°E. Thick and thin short dashed lines correspond to ensemble members of strong and weak meander, respectively. Thick line with crosses denote ensemble mean. Long dashed line with crosses denotes the unperturbed forecast. Dot dashed line with crosses denotes the reference run. (b) As in Fig.2.7a except for sea level difference between Kushimoto and Uragami. (c) As in Fig.2.7a except for sea level of Hachijojima.

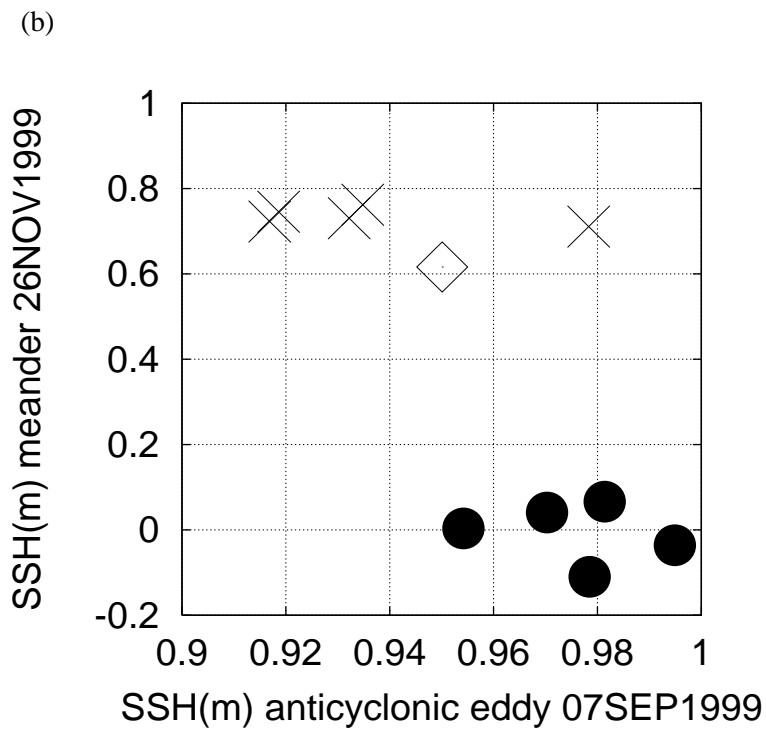
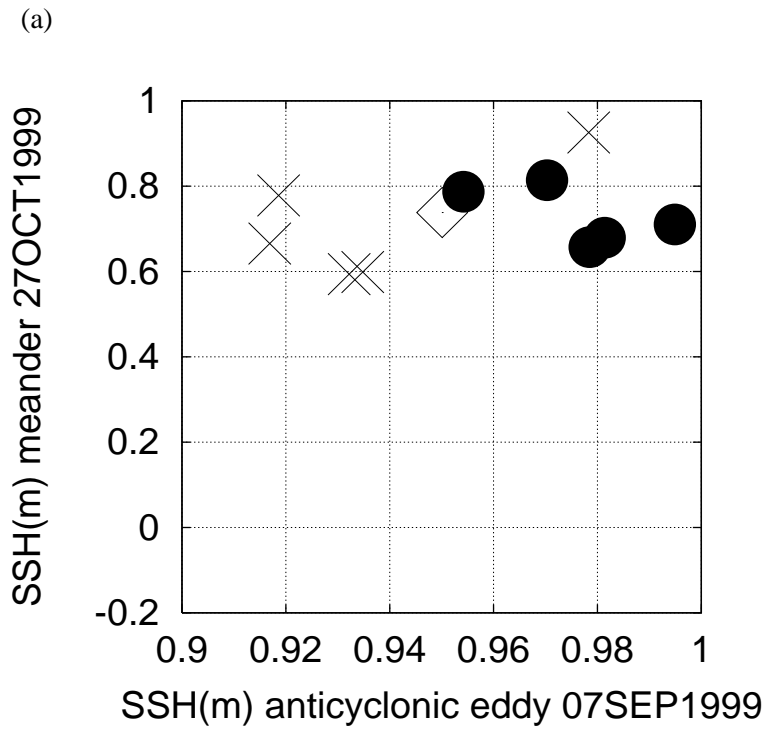


Figure 2.8 (a) Relations between intensity of the trigger anticyclonic eddy (mean over a region in which sea surface height exceeds 0.9m within the Kuroshio region, 28°-32°N, 130°-136°E) and the Kuroshio meander amplitude (sea surface height at 32.5°N, 138°E) on 27 October 1999. Closed circles correspond to ensemble members of the large-meander. Crosses correspond to ensemble members of the non-large-meander. A diamond corresponds to the unperturbed forecast. (b) As in Fig.2.8a on 26 November 1999.

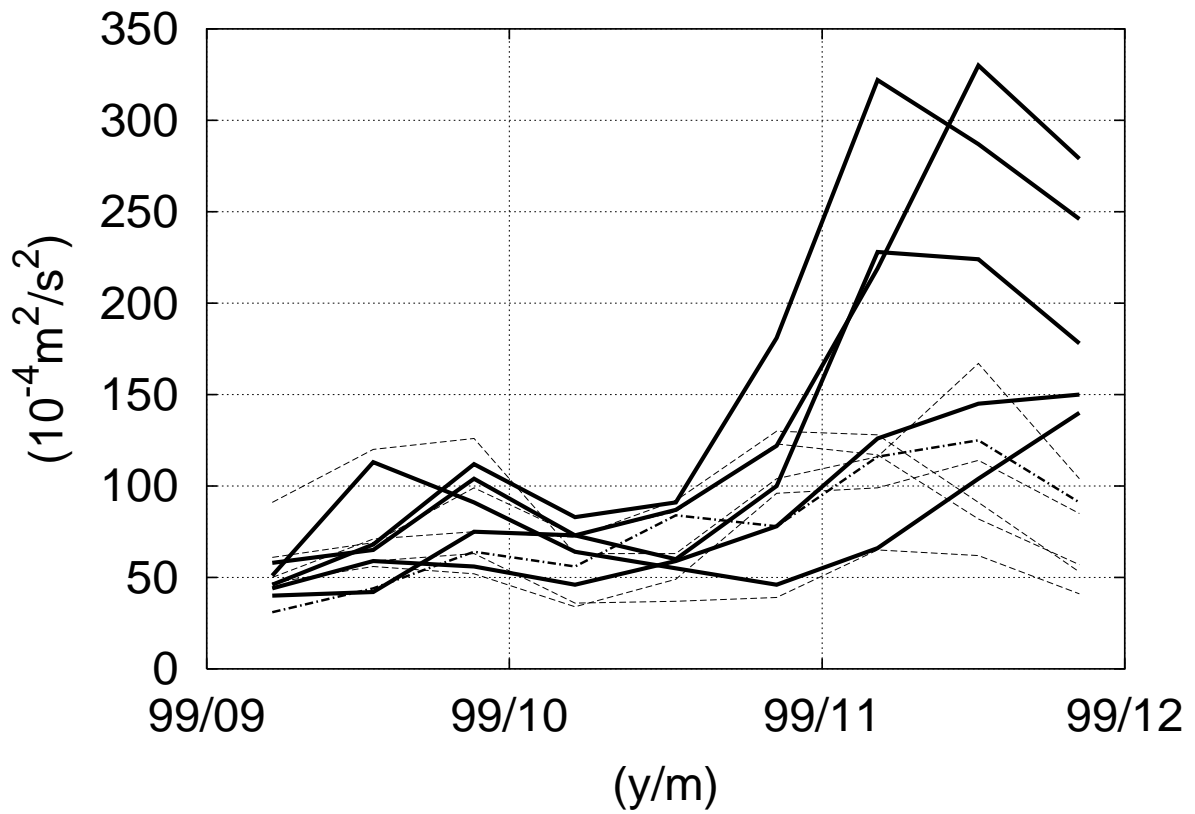


Figure 2.9 Evolution of kinetic energy (in m^2/s^2) at the depth of 4000m averaged over 31° - 33° N, 135° - 138° E. Solid lines correspond to ensemble members of the large-meander. Dashed lines correspond to individual ensemble members of the non-large-meander. Dot dashed line denotes the unperturbed forecast.

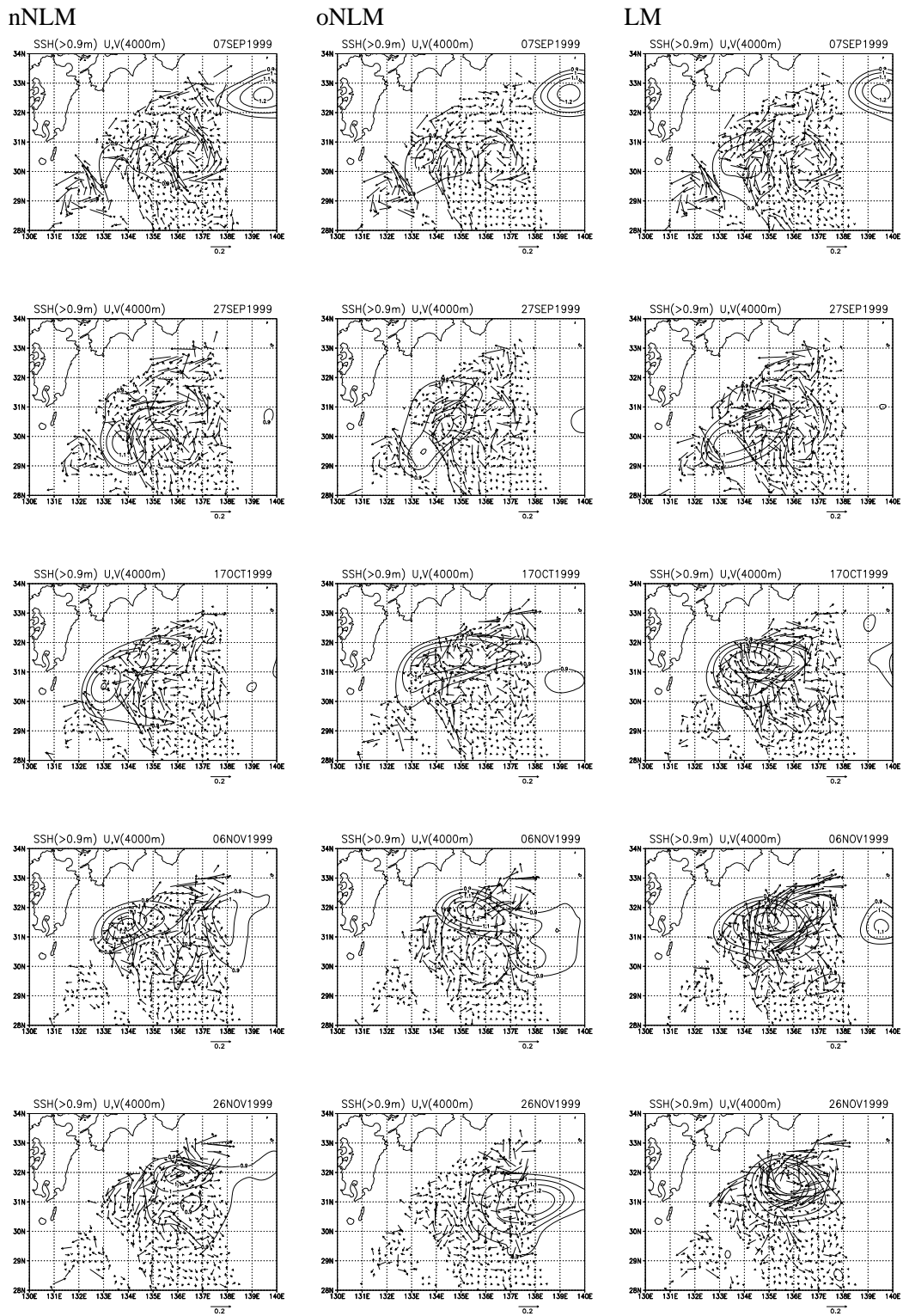


Figure 2.10 Snapshots of sea surface height upper 0.9m (contour interval is 0.1m) and horizontal velocity at 4000m depth. Left panels: an ensemble member corresponding to the nearshore non-large-meander. Middle panels: the unperturbed forecast, which realizes the offshore non-large-meander. Right panels: an ensemble member corresponding to the large-meander.

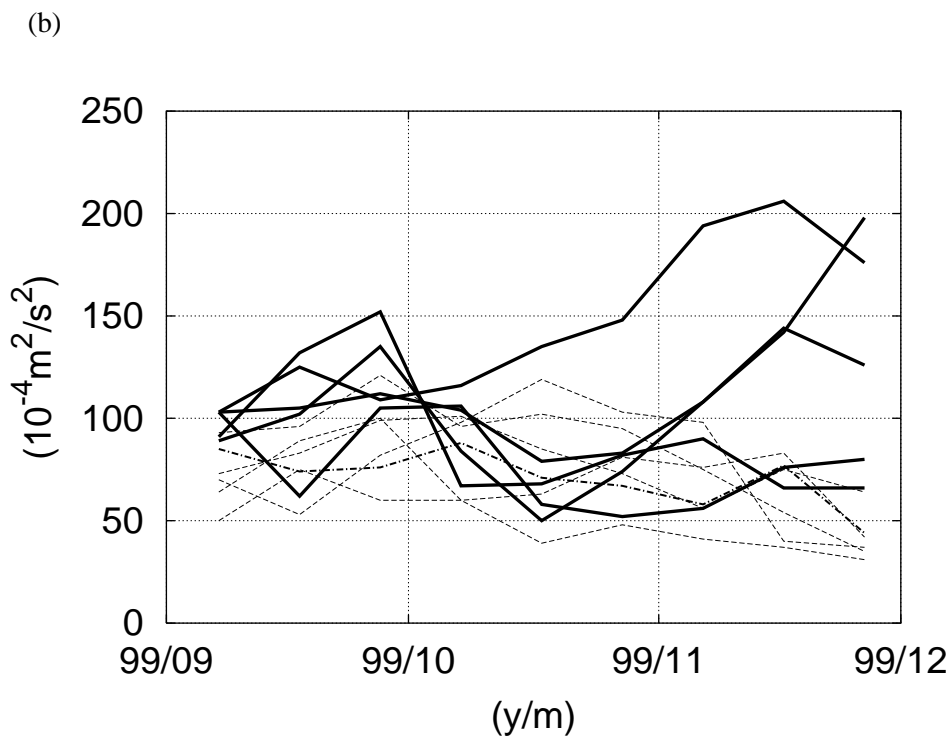
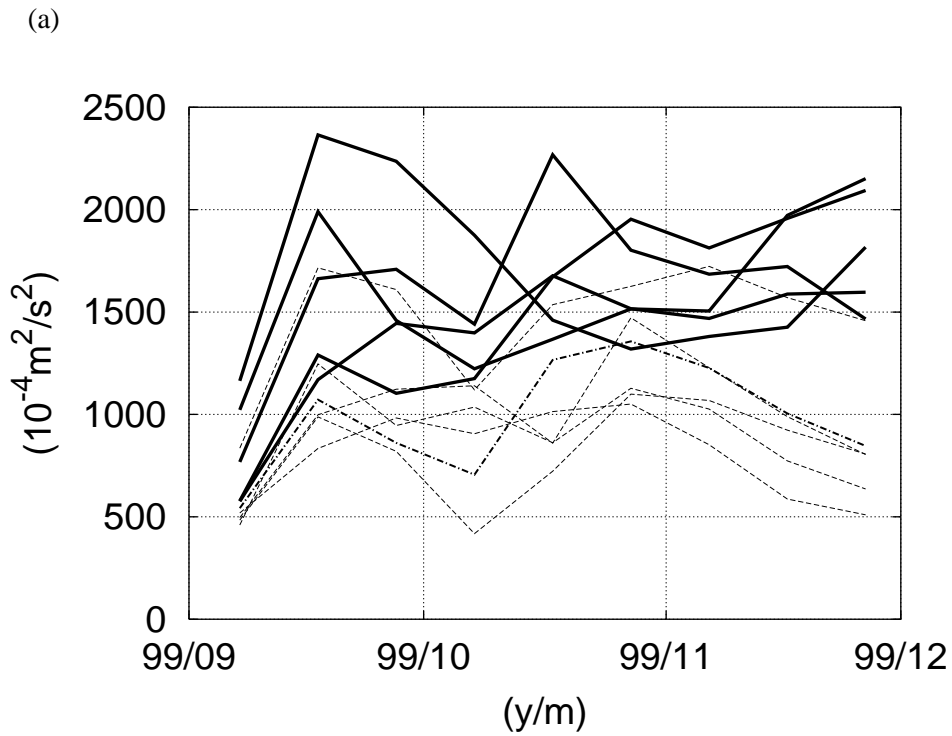


Figure 2.11 (a) As in Fig.2.9 except for kinetic energy (in m^2/s^2) of the trigger anticyclonic eddies (a region in which sea surface height exceeds 0.9m, averaged over 28° - 32° N, 130° - 136° E in September 1999 and over 29° - 32.5° N, 133° - 140° E in October and November 1999) at the depth of 200m. (b) As in Fig.2.12a except for the depth of 4000m.

General Conclusion

In this thesis, using the basin-scale eddy-resolving ocean general circulation model (OGCM), we investigated the Kuroshio path variations south of Japan due to meso-scale eddies and their predictability.

To simulate the Kuroshio path variations and meso-scale eddy activity as realistically as possible, we have developed a nested high-resolution nested grid model for the North Pacific. The horizontal grid spacing of the model, $1/12^\circ$, is much smaller than the first baroclinic Rossby radius in the Northwest Pacific.

In part I, we investigated possible connections between the Kuroshio path variations and meso-scale eddy activity using the OGCM. The model with atmospheric forcing from 1992-1998 well simulated meso-scale activity south of Japan. In addition, the model reproduced the offshore non-large-meander path, the nearshore non-large-meander path and the large-meander like path. We showed that the anticyclonic vorticity supply through intrusion of eddies destabilizes the Kuroshio, thus generating the large-meander like path. The present model simulates the eddy-Kuroshio interaction in a more realistic way than previous studies. However, its ability to reproduce the large-meander state needs improvement because the duration is too short compared to observations. Thus we must distinguish the simulated large meander like path from the real large-meander. Nevertheless, the existence of the brief large-meander like path states in the model may suggest a working hypothesis for the real large-meander formation because the present model appears to capture almost all key elements in the large-meander formation.

A synthesis of these results leads to the following scenario for the formation of the Kuroshio large-meander. At the beginning, anticyclonic eddies are activated near Taiwan or the Philippine coast and advected by the Kuroshio into the Shikoku Basin. The transport across the PN line increases by the successive arrival of those anticyclonic eddies and the anticyclonic Kuroshio recirculation south of Shikoku is intensified by the merger of those eddies. Then, the Kuroshio large-meander is generated by baroclinic instability that is

triggered by the interaction with the anticyclonic/cyclonic eddies. During the meandering period, the meandering cyclonic jet matures by absorbing a cyclonic ring propagating from the Kuroshio Extension and eventually sheds the cyclonic ring. Thus, the large-meander state ends. The above scenario suggests the importance of eddy activities to the Kuroshio meandering and provides a key to predict the ever-mysterious phenomenon of the Kuroshio meander; the eddy activities introduce a favorable condition for the Kuroshio large-meander formation through intensification of the Kuroshio recirculation.

However, since the simulated large-meander like path is unstable, the above scenario provides no favorable conditions for the long-lived meander. Those conditions might be related to basin scale climate variations. Observational evidence suggests bi-decadal frequency variation of the large-meander occurrence (Kawabe 2001). The period of the present OGCM simulation from 1992 to 1998 corresponds to the non-large-meander period. Further observational and modeling studies are needed to clarify the maintenance mechanism of the large-meander.

In part II, we discussed the event in 1999 using the OGCM initialized by assimilating the TOPEX/POSEIDON altimetry data. The results of Part I suggested that the Kuroshio path variations are strongly affected by the eddy-Kuroshio interactions. Therefore, data assimilation is necessary to simulate the Kuroshio path variations in a right place at a right time. We conducted a hindcast experiment of the Kuroshio path from September 1999 to November 1999. It was found that the model has forecasting skill within 80 days after last initialization.

In order to systematically evaluate the impact of difference of initial state, we adopted ensemble forecasts in the hindcast experiment. This part is a first comprehensive study of the Kuroshio meandering using the ensemble forecast. The ensemble forecast experiment exhibited interesting case-by-case variation in the ensemble. The meanders appeared in the ensemble members for the 80 days forecast are classified into two categories: the

large-meander and the non-large-meander. The bifurcation occurs more than 50 days after the initialization. The ensemble forecast experiment for the 1999 event suggests that the real Kuroshio state falls in the multiple equilibrium state in 1999.

The intensity of an initial anticyclonic eddy plays a key role in subsequent development into the two categories; a strong anticyclone induces the large-meander. The strong anticyclonic eddy triggers the distinctive joint evolution of the upper and lower layer circulations associated with the growth of the large-meander. The detected process supports a part of the scenario for the formation of the large-meander suggested in Part I. The time scale of the anticyclonic eddy is determined by the slow lower-layer velocity field rather than direct advection by the Kuroshio. It is consistent with the limit of the predictability in the present study, i.e., 50-80 days.

Despite the ability to simulate some aspect of the Kuroshio path variation, the model has biases. The simulated eddy activity from the subtropical front east of the Nansei Islands is weaker than in the observations (Fig.1.5). Since meso-scale eddies in this region are important to generate the variation of the Kuroshio volume transport (Ichikawa 2001), improvement of the model performance in this region may lead to more realistic simulation of the Kuroshio path variation.

The model climatology indicates a strong trough of the Kuroshio Extension at 142°E (Fig.1.3). This feature, which is inconsistent with the observation (Mizuno and White 1983), may affect the model Kuroshio path variation south of Japan (Fig.1.13d, Fig.1.14a). Also, the overestimation of the transport of the Kuroshio recirculation (Section 1.3.1) has to be improved for better modeling of the Kuroshio path variation.

The present study suggests the importance of the eddy dynamics in the Kuroshio recirculation region to the Kuroshio path variation south of Japan. However, detailed mechanism is still unclear. Further intensive studies may be needed on interactions with the Kuroshio and both the local topography and meso-scale eddy. To clarify connections

between the Kuroshio path variations and the basin-wide climate change, it is also necessary to investigate mechanism of the Kuroshio volume transport variations in detail. In the present OGCM simulation, the meso-scale eddy activities near Taiwan or the Philippine coast affect the Kuroshio volume transport in the East China Sea. Questions how the basin-scale wind variation is related to the meso-scale eddy activities in the subtropical front region or the upstream Kuroshio volume transport still remain to be understood.

This study suggests necessary conditions for modeling and forecasting of the Kuroshio path variation south of Japan. First, the whole subtropical gyre system over the North Pacific should be modeled because the Kuroshio volume transport is basically determined by the basin-scale wind variation. Second, the model requires to cover both the Kuroshio-Kuroshio Extension and the subtropical front regions with horizontal resolution of smaller than 1/10 degree. The present study suggests that the Kuroshio path variation is affected by the eddy activities in the above regions. Third, the modeler should carefully treat both bottom topography and stratification. The Kuroshio path is strongly controlled by bottom slope along the south coast of Japan. The Izu-Ogasawara Ridge, moreover, plays an important role in eastward shift of the Kuroshio meander, which leads to decline of the meander amplitude. Skill of the sigma coordinate model is sensitive to smoothness of the bottom topography. Stratification may be well simulated by well-designed vertical grid of more than 20 levels. Fourth, realistic forcing is important. The satellite scatterometer wind is one of suitable choices. Fifth, proper initialization is necessary for forecasting of the real Kuroshio path variation. Both the intensity and shape of the trigger eddies related with the Kuroshio path variation significantly affects the evolution of the Kuroshio path. Multi use of satellite altimeters in data assimilation allows better spatial resolution for capturing the eddies.

Based on these suggestions, an operational nowcast/forecast system in the Japan coastal

ocean has been developed (Miyazawa and Yamagata 2003; Miyazawa et al. 2005a). In future studies, data products created by more advanced nowcast/forecast systems will be utilized to describe oceanic variations realistically and investigate ocean dynamics in detail. The present study is a first step toward this direction.

Acknowledgements

I am most grateful to my supervisor, Prof. Toshio Yamagata, who has encouraged me with great patience, throughout the long process of completion of this work. The members of my dissertation committee: Prof. Ichiro Yasuda, Prof. Toshiyuki Hibiya, Prof. Masaki Kawabe, Prof. Hiroshi Niino provided many useful comments and suggestions. I appreciate Prof. Humio Mitsudera, Dr. Takashi Kagimoto, Dr. Xinyu Guo, Dr. Shozo Yamane, and Dr. Hirofumi Sakuma for their suggestions and encouragement. Acknowledgement is also given to Ms. Michiko Oishi for great encouragement during the long course of completion of this work. Dr. H. Xue kindly provided me with the code for the linear stability analysis. This work is part of the Japan Coastal Ocean Predictability Experiment (JCOPE) started in October 1997 under the initiative of the Frontier Research System for Global Change (FRSGC), which was supported jointly by National Space Development Agency of Japan (NASDA) and Japan Marine Science and Technology Center (JAMSTEC). The scientific interaction with the IOC/UNESCO NEAR-GOOS project supported by Ministry of Education, Culture, Sports, Science and Technology (MEXT) was helpful in completing this work. Observed sea level data were provided by the Japan Oceanographic Data Center. Barometric pressure data for correction of the observed sea level data were provided by the Japan Meteorological Agency.

References

- Akitomo, K., and M. Kurogi, 2001: Path transition of the Kuroshio due to mesoscale eddies: A two-layer, wind-driven experiment, *J. Oceanogr.*, **57**, 735-741.
- Boyer, T. P., and S. Levitus, 1997: Objective analyses of temperature and salinity for the world ocean on a 1/4 degree grid, *NOAA Atlas NESDIS*, **11**, U. S. Dep. Of Comm., Washington, D.C.
- Cushman-Roisin, B., 1986: Frontal geostrophic dynamics, *J. Phys. Oceanogr.*, **16**, 132-143.
- Cushman-Roisin, B., Sutyryn, G. G., and B. Tang, 1992: Two-layer geostrophic dynamics. Part I: governing equations, *J. Phys. Oceanogr.*, **22**, 117-126.
- Da Silva, A., C. Young and S. Levitus, 1994: Atlas of Surface Marine Data, Volume1: Algorithms and Procedures, *NOAA Atlas NESDIS*, **6**, U. S. Dep. of Comm., Washington D.C.
- De Szoeki, R., A., 1975: Some effects of bottom topography on baroclinic instability. *J. Mar. Res.*, **33**, 93-122.
- Ebuchi, N., and K. Hanawa, 2000: Mesoscale eddies observed by TOLEX-ADCP and TOPEX/POSEIDON altimeter in the Kuroshio recirculation region south of Japan, *J. Oceanogr.*, **56**, 43-57.
- , and -----, 2003: Influence of mesoscale eddies on variations of the Kuroshio path south of Japan, *J. Oceanogr.*, **59**, 25-36.
- Emery, W. J., W. G. Lee, and L. Magaard, 1984: Geographical and seasonal distributions of Brunt-Vaisala frequency and Rossby radii in the north Pacific and North Atlantic, *J. Phys. Oceanogr.*, **14**, 294-317.
- Endoh, T., and T. Hibiya, 2001: Numerical simulation of the transient response of the Kuroshio leading to the large meander formation south of Japan, *J. Geophys. Res.*, **106**, 26833-26850.
- Evensen, G., 1994: Sequential data assimilation with a nonlinear quasigeostrophic model

- using Monte Carlo methods to forecast error statistics, *J. Geophys. Res.*, **97**, 10,143-10162.
- Ezer, T., and G. L. Mellor, 1994: Diagnostic and prognostic calculations of the North Atlantic circulation and sea level using a sigma coordinate ocean model, *J. Geophys. Res.*, **99**, 14159-14171.
- Guo, X., H. Hukuda, Y. Miyazawa, and T. Yamagata, 2003: A triply nested ocean model simulating the Kuroshio –Roles of horizontal resolution on JEBAR-, *J. Phys. Oceanogr.*, **33**, 146-169.
- Haney, R., 1971: Surface thermal boundary condition for ocean circulation models, *J. Phys. Oceanogr.*, **1**, 241-248.
- Hasunuma, K., and K. Yoshida, 1978: Splitting of the subtropical gyre in the Western North Pacific, *J. Oceanogr. Soc. Jpn.*, **34**, 160-172.
- Hurlburt, H. E., A. J. Wallcraft, W. J. Scmitz Jr. P. J. Hogan, and E. J. Metzger, 1996: Dynamics of the Kuroshio/Oyashio current system using eddy-resolving models of the North Pacific Ocean, *J. Geophys. Res.*, **101**, 941-976..
- Ichikawa, K., and S. Imawaki, 1994: Life history of a cyclonic ring detached from the Kuroshio Extension as seen by the Geosat altimeter., *J. Geophys. Res.*, **99**, 15953-15966.
- , 2001: Variation of the Kuroshio in the Tokara Strait induced by meso-scale eddies. *J. Oceanogr.*, **57**, 55-68.
- Imawaki, S., U. Hiroshi, H. Ichikawa, M. Fukazawa, S. Umatani, and ASUKA Group, 2001: Satellite altimeter monitoring the Kuroshio transport south of Japan, *Geophys. Res. Lett.*, **28**, 17-20.
- Kagimoto, T., and T. Yamagata, 1997: Seasonal transport variations of the Kuroshio: An OGCM simulation, *J. Phys. Oceanogr.*, **27**, 403-418.
- , 1999: Numerical study on transport variations of the Kuroshio, Doctor thesis, The

- University of Tokyo. Pp75.
- Kalnay, E., and Coauthors, 1996: The NCEP/NCAR 40-Year Reanalysis Project. *Bull. Amer. Meteor. Soc.*, **77**, 437-471.
- Kamachi, M., T. Kuragano, S. Sugimoto, K. Yoshida, T. Sakurai, T. Nakano, N. Usui, and F. Uboldi, 2004: Short-range prediction experiments with operational data assimilation system for the Kuroshio south of Japan. *J. Oceanogr.*, **60**, 269-282.
- Kawabe, M., 1985: Sea level variations at the Izu islands and typical stable paths of the Kuroshio, *J. Oceanogr. Soc. Jpn.*, **41**, 307-326.
- , 1987: Spectral properties of sea level and time scales of Kuroshio path variations, *J. Oceanogr. Soc. Jpn.*, **43**, 111-123.
- , 1995: Variations of current path, velocity, and volume transport of the Kuroshio in relation with the large meander, *J. Phys. Oceanogr.*, **25**, 3103-3117.
- , 2001: Interannual variations of sea level at the Nansei Islands and volume transport of the Kuroshio due to wind change, *J. Oceanogr.*, **57**, 189-205.
- Komori, N., T. Awaji, Y. Ishikawa, and T. Kuragano, 2003: Short-range forecast experiments of the Kuroshio path variabilities south of Japan using TOPEX/Poseidon altimetric data. *J. Geophys. Res.*, **108**, NO. C1, 3010, doi:10.1029/2001JC001282.
- Kuragano, T. and M. Kamachi, 1999: Global statistical space-time scales of oceanic variability estimated from the TOPEX/POSEIDON altimetry data, *J. Geophys. Res.*, **105**, 955-974.
- Levitus, S., and, T. P. Boyer, 1994: *World Ocean Atlas*, vol. 4, *Temperature*, NOAA Atlas NESDIS, **4**, U. S. Dep. Of Comm., Washington, D.C.
- , R. Burgett, and, T. P. Boyer, 1994: *World Ocean Atlas*, vol. 3, *Salinity*, NOAA Atlas NESDIS, **3**, U. S. Dep. Of Comm., Washington, D.C.
- Lillibridge, J., L. Robert, and F. Vossepoel, 1997: Real-Time Altimetry from ERS-2,

- paper presented at 3rd ERS Symposium, Florence, Italy.
- Masina, S., S. G. H. Philander, and, A. B. G. Bush, 1999: An analysis of tropical instability waves in a numerical model of the Pacific Ocean 2. Generation and energetics of the waves, *J. Geophys. Res.*, **104**, 29637-29661.
- Masuda, A., 1982: An interpretation of the bimodal character of the stable Kuroshio path, *Deep-Sea Res.*, **29**, 471-484.
- Mellor, G. L., and T. Yamada, 1982: Development of a turbulence closure model for geophysical fluid problems, *Rev. Geophys. Space Phys.*, **20**, 851-875.
- Mellor, G. L., and T. Ezer, 1991: A Gulf Stream model and an altimetry assimilation scheme, *J. Geophys. Res.*, **96**, 8779-8795.
- , T. Ezer, and L.-Y. Oey, 1994: The pressure gradient conundrum of sigma coordinate ocean models, *J. Atmos. Oceanic Tech.*, **11**, 1126-1134.
- , 1996: Users guide for a three-dimensional, primitive equation, numerical ocean model. Available from the following website:
<http://www.aos.princeton.edu/WWWPUBLIC/htdocs.pom/>.
- Miller, R. N., and L. L. Ehret, 2002: Ensemble generation for models of multimodal systems, *Mon. Wea. Rev.*, **30**, 2313-2333.
- Mitsudera, H. and R. Grimshaw, 1994: Capture and resonant forcing of solitary waves by the interaction of a baroclinic current with topography, *J. Phys. Oceanogr.*, **24**, 2217-2244.
- Mitsudera, H., T. Waseda, Y. Yoshikawa, and B. Taguchi, 2001: Anticyclonic eddies and Kuroshio meander formation, *Geophys. Res. Lett.*, **28**, 2025-2028.
- Miyazawa, Y., and T. Yamagata, 2003: The JCOPE ocean forecast system (in Japanese), *Monthly Kaiyo*, **12**, 881-886.
- Miyazawa, Y., X. Guo, and T. Yamagata, 2004: Roles of meso-scale eddies in the Kuroshio paths, *J. Phys. Oceanogr.*, **34**, 2203-2222.

- Miyazawa, Y., T. Kagimoto, H. Kawajiri, R. Zhang, H. Sakuma, X. Guo, and T. Yamagata, 2005a: Current and future perspective of the JCOPE ocean forecast system (in Japanese), *Monthly Kaiyo*, in printing.
- Miyazawa, Y., S. Yamane, X. Guo, and T. Yamagata, 2005b: Ensemble forecast of the Kuroshio meandering, submitted to *J. Geophys. Res.*
- Mizuno, K., and W. B. White, 1983: Annual and interannual variability in the Kuroshio Current System, *J. Phys. Oceanogr.*, **13**, 1847-1867.
- Murphy, J. M., 1988: The impact of ensemble forecasts on predictability, *Q. J. R. Meteorol. Soc.*, **114**, 463-493.
- Pedlosky, J., 1987: *Geophysical Fluid Dynamics, second edition*. Springer-Verlag, pp.710.
- Qiu, B., and W. Miao, 2000: Kuroshio path variations south of Japan: Bimodality as a self-sustained internal oscillation, *J. Phys. Oceanogr.*, **30**, 2124-2137.
- Reynolds, R. W., and T. M. Smith, 1994: Improved global sea surface temperature analysis, *J. Climate*, **7**, 929-948.
- Robinson, A. R., and B. Taft, 1972: A numerical experiment for the path of the Kuroshio, *J. Mar. Res.*, **30**, 65-101.
- Rosati, A. and K. Miyakoda, 1988: A general circulation model for upper ocean simulation, *J. Phys. Oceanogr.*, **18**, 1601-1626.
- Saiki, M., 1982: Relation between the geostrophic flux of the Kuroshio in the eastern China Sea and its large meanders in south of Japan, *Oceanogr. Mag.*, **32**, 11-18.
- Takano, S., 2002: Application technique of ensemble prediction (in Japanese), in *Meteorological Research Note*, edited by S. Takano, **201**, 73-103.
- Toth, Z. and E. Kalnay, 1993: Ensemble forecasting at NMC: The generation of perturbations, *Bull. Amer. Meteor. Soc.*, **74**, 2317-2330.
- Smagorinsky, J., S. Manabe, and J. L. Holloway, 1965: Numerical results from a

- nine-level general circulation model of the atmosphere, *Mon. Weather Rev.*, **93**, 727-768.
- Stammer, D., 1997: Global characteristics of ocean variability estimated from regional TOPEX/POSEIDON altimeter measurements, *J. Phys. Oceanogr.*, **27**, 1743-1769.
- Solomon, H., 1978: Occurrence of small “trigger” meanders in the Kuroshio off southern Kyushu, *J. Oceanogr. Soc. Jpn.*, **34**, 81-84.
- Wells, N., C., V., O., Ivchenko, and S., E., Best, 2000: Instabilities in the Agulhas retroflection current system: a comparative model study. *J. Geophys. Res.*, **105**, 3233-3241.
- White, W. B., and J. P. McCreary, 1976: On the formation of the Kuroshio meander and its relationship to the large-scale ocean circulation, *Deep-Sea Res.*, **23**, 33-47.
- Williams, G., P. and T. Yamagata, 1984: Geostrophic regimes, intermediate solitary vortices and Jovian eddies, *J. Atmos. Sci.*, **41**, 453-478.
- Xue, H., and G. Mellor, 1993: Instability of the Gulf Stream meanders in South Atlantic Bight. *J. Phys. Oceanogr.*, **23**, 2326-2350.
- Yamagata, T., Y. Shibao and S. Umatani, 1985: Interannual variability of the Kuroshio Extension and its relation to the Southern Oscillation/El Nino. *J. Oceanogr. Soc. Jpn.*, **41**, 274-281.
- Yamagata, T., and S. Umatani, 1987: The capture of current meander by coastal geometry with possible application to the Kuroshio current, *Tellus*, **39A**, 161-169.
- , and -----, 1989: Geometry-forced coherent structures as a model of the Kuroshio large meander, *J. Phys. Oceanogr.*, **19**, 130-138.
- Yamane, S. and S. Yoden, 2001: Finite-time evolution of small perturbations superposed on a chaotic solution: experiment with an idealized barotropic model, *J. Atmos. Sci.*, **58**, 1066-1078.
- Zhu X.-H., A. Kaneko, T. Saito, and N. Gohda, 2001: Kuroshio stream path variation and

its associated velocity structures south of Shikoku, Japan. *Geophys. Res. Let.*, **28**, 4615-4618.

Zhu X.-H., I.-S. Han, J.-H. Park, H. Ichikawa, K. Murakami, A. Kaneko, and A. Ostrovskii, 2003: The Northeastward current southeast of Okinawa Island observed during November 2000 to August 2001. *Geophys. Res. Let.*, **30**, 10.1029/2002GL015867.